

30 MAY 2000

**EFFECT PROCESSING ON THE EVOLUTION OF
INTERFACES
METAL MATRIX COMPOSITES**

FINAL REPORT

May 2000

AIR FORCE OFFICE OF SCIENTIFIC RESEARCH

Grant No. F49620-96-0256

Professor Namas Chandra
Department of Mechanical Engineering
FAMU-FSU College of Engineering
Florida State University
2525 Pottsdamer Street, Room 229
Tallahassee, FL 32310

APPROVED FOR PUBLIC RELEASE
DISTRIBUTION UNLIMITED

THIS VIEWS, OPINIONS, AND/OR FINDINGS CONTAINED IN THIS REPORT ARE
THOSE OF THE AUTHOR(S) AND SHOULD NOT BE CONSTRUED AS AN OFFI-
CIAL DEPARTMENT OF THE ARMY POSITION, POLICY, OR DECISION, UNLESS
SO DESIGNED BY OTHER DOCUMENTATION.

20010905 128

AFRL-SR-BL-TR-01-

REPORT DOCUMENTATION PAGE

0460

Public reporting burden for this collection of information is estimated to average 1 hour per response, including the gathering and maintaining the data needed, and completing and reviewing the collection of information. Send comments regarding this burden estimate or any other aspect of this collection of information, including suggestions for reducing this burden, to Washington Headquarters Services, Directorate for Information Operations and Reports, 1215 Jefferson Davis Highway, Suite 1204, Arlington, VA 22202-4302, and to the Office of Management and Budget, Paperwork Reduction Project (0704-0188), Washington, DC 20503.

1. AGENCY USE ONLY (Leave blank)		2. REPORT DATE May 15, 2000		3. REPORT TYPE AND DATES COVERED Final Report 1 June 96- 31 May 98	
4. TITLE AND SUBTITLE Effect of Processing on the Evolution of Interfaces in Metal Matrix Composites				5. FUNDING NUMBERS Grant No. F49620-96-1-0256	
6. AUTHOR(S) Dr. Namas Chandra (P. I.)					
7. PERFORMING ORGANIZATION NAME(S) AND ADDRESS(ES) Florida State University Contracts and Grants Office 407 Westcott Building Tallahassee Florida 32306				8. PERFORMING ORGANIZATION REPORT NUMBER	
9. SPONSORING / MONITORING AGENCY NAME(S) AND ADDRESS(ES) AFOSR/NA 110 Duncan Avenue B115 Bolling AFB DC 20332-8050				10. SPONSORING / MONITORING AGENCY REPORT NUMBER	
11. SUPPLEMENTARY NOTES The views, opinions and/or findings contained in this report are those of the author(s) and should not be construed as an official Department of the Army position, policy or decision, unless so designated by other documentation.					
12a. DISTRIBUTION / AVAILABILITY STATEMENT Approved for public release; distribution unlimited.				12 b. DISTRIBUTION CODE	
13. ABSTRACT (Maximum 200 words) The issues in this research focused on the understanding the chemical evolution (diffusional) process at the interface, developing a mechanistic model of an interface based on stress or energy failure criterion, and studying the effect of interface properties on the performance of the composites. The approach involved both experimental and computational components. a link between the evolution of chemistry and geometry of the reaction zone and the interfacial properties. Microstructural studies reveal that reaction growth is due to transformation of both coating and the matrix. Push-out tests conducted on heat treated specimens reveal that the effect of thermal exposure on interfacial properties is predominantly due to exposure temperature. Time of exposure is found to have only a secondary effect. The push out data was used indirectly to evaluate both strength and toughness properties of the interfaces. The local shear strength of Ti-6Al-4V/SCS-6 interfaces was found to be of the order of 450 Mpa, in comparison with much lower (120 Mpa) average shear strength reported elsewhere. Also a fracture toughness of 50 Mpa m ^{1/2} was found in this research. Also the fracture toughness values remain more or less constant for normal use temperatures in the range of 450 to 700° C.					
14. SUBJECT TERMS				15. NUMBER OF PAGES	
				16. PRICE CODE	
17. SECURITY CLASSIFICATION OR REPORT UNCLASSIFIED	18. SECURITY CLASSIFICATION OF THIS PAGE UNCLASSIFIED	19. SECURITY CLASSIFICATION OF ABSTRACT UNCLASSIFIED	20. LIMITATION OF ABSTRACT UL		

EXECUTIVE SUMMARY

In this work, the effect of processing on the origin and the evolution of interfaces in metallic/intermetallic matrix composites were studied. Novel computational methods using nonlinear finite element method combined with experimental work (both processing and push-out testing) were used in this investigation. Typical Titanium based MMCs and IMCs such as SiC/Ti-6Al-4V, SiC/Ti-15V-3Sn-3Al and SiC/Ti-24Al-11Nb systems were used as model material in this study. MMCs and IMCs are significantly influenced by the presence of large levels of residual stresses arising from processing as well as use temperature and time. This is quite different from that of other composite systems such as polymeric and ceramic matrix composite systems. Thus great caution needs to be exercised when results are extended from these systems to MMCs. A comprehensive study of the origin and role of residual stresses on the interface behavior was carried out in this work.

Interfaces in composites play a very vital role in determining the strength, stiffness and failure characteristics of composite systems. Hence in this work, the thermomechanical behavior of interfaces was carefully analyzed. The strength and toughness behaviour of composites were modeled using energy based criterion. The shear strength and fracture toughness of interfaces were evaluated from push-out test results in conjunction with nonlinear finite element analysis incorporating equivalent domain integral methods. This report contains details of the results in the areas of elevated temperature effects, evolution of interface chemistry, effect of residual stress on fracture behavior, the effect of debonding and fiber fracture on the evolution of damage in composites and the prediction of composite behavior given the interfacial properties.

ACKNOWLEDGMENTS

The authors wish to acknowledge Air Force Office of Scientific Research and project monitors, Drs. Walter Jones and Ozden Ochoa for providing financial assistance in support of the project.

PUBLICATIONS DURING THE PROJECT PERIOD 1996 - 1999

Journal Papers

1. S. R. Voleti, C. R. Ananth and N. Chandra, Effect of Fiber Fracture and Matrix Yielding on Load Sharing in Continuous Fiber Metal Matrix Composites, *Journal of Composites Technology and Research*, 20, 4, 203-209, (1998).
2. C.R. Ananth, S. R. Voleti and N. Chandra, Effect of Fiber Fracture and Interfacial Debonding on the Evolution of Damage in Metal Matrix Composites, *Composites Part A*, 29A, 1203-1211, (1998)
3. S. Mukherjee, C. R. Ananth and N. Chandra, Effect of Interface Chemistry on the Fracture Properties of Titanium Matrix Composites, *Composites Part A*, 29A, 1213-1219, (1998)
4. S. R. Voleti, C. R. Ananth and N. Chandra, Effect of Interfacial Properties on the Fiber Fragmentation Process in Polymer Matrix Composites, *Journal of Composites Technology and Research*, 20, 1, 16-26, (1998).
5. S. Mukherjee, C. R. Ananth and N. Chandra, Evaluation of Fracture Toughness of MMC Interfaces Using Thin-slice Push-out Tests, *Scripta Materialia*, 36, 1333-1338 (1997).
6. C. R. Ananth, S. Mukherjee, and N. Chandra, Effect of Time Dependent Matrix Behavior on the Evolution of Processing-Induced Residual Stresses in Metal Matrix Composites, *Journal of Composites Technology and Research* 19, 3, 134-141, (1997).
8. S. Mukherjee, C. R. Ananth and N. Chandra, Effect of Residual Stresses on the Interfacial Fracture Behavior of Metal Matrix Composites, *Composite Science and Technology*, 57, 1501-112, (1997).
9. C. R. Ananth and N. Chandra, Elevated temperature interfacial behavior of MMC: a computational study, *Composites: Part A*, 27A, 805-811 (1996).
10. Voleti, S.R., N. Chandra and J R. Miller, Global-Local Analysis of Large-scale Composite Structures Using Finite Element Methods, *Composites & Structures*, 58, 3, 453-464, (1996).

Proceedings (conference, symposium, congress)

11. N. Chandra, Effect of Processing on the Evolution of Interfaces in Metal Matrix Composites, *Proceedings of AFOSR Mechanics of Composites Materials*, Dayton, Ohio, October 14-16, pages 159-165, (1998).
12. Chandra, N. and H. Ghonem, Evaluation of Crack Behavior in Bimaterial Interfaces Using Experimental and Computational Methods, 8th U.S.-Japan Conference on Composite Materials, ed. G. Newaz and R. Gibson, Technomic Publications, (in print), (1998).

13. Chandra, N. and J Watts, Effect of Elevated Temperature Exposure on the Interfacial Properties of SCS-6/Timetal 21S Composites, 8th U.S.-Japan Conference on Composite Materials, ed. G. Newaz and R. Gibson, Technomic Publications, (in print), (1998).
14. S.R. Voleti, C.R. Ananth and N. Chandra, Evolution of Micro-Damage in a Metal Matrix Composite, ICES 97', Costa Rica, pages 1214-1219, (1997).
15. Mukherjee, S., C.R. Ananth and N. Chandra, Evaluation of Fracture Toughness of MMCs Using a Computational Approach, Proceedings of the American Society for Composites -11th Technical Conference, ed. W.S. Johnson, 330-333, (1996).
16. Voleti, S.R., C.R. Ananth, N. Chandra and B.S. Majumdar, Effect of Matrix and Interfacial Behavior on Load Sharing in Metal Matrix Composites, Proceedings of the American Society for Composites -11th Technical Conference, ed. W.S. Johnson, 340-348, (1996).
17. Mukherjee, S., C.R. Ananth and N. Chandra, Effect of Matrix Viscoplasticity on Residual Stresses in MMCs: Computational and Experimental Analysis, Constitutive Laws, Experimental and Numerical Implementation, ed A.M. Rajendran and R.C. Batra, CIMNE Publishers, 203-214, (1995).
18. Mukherjee, S., C.R. Ananth and N. Chandra, Effect of Viscoplastic Constitutive Behavior on Residual Stresses in Metal Matrix Composites, 6 Pages, Computational Mechanics '95 , ed. S.N. Atluri, G. Yagawa and T.A. Cruse, Springer Verlag Publishers, 1803-1808, (1995).

Conference Papers

1. N Chandra, Residual Stresses-Origin and Effects in MMCs, Wright Patterson Air Force Base, Dayton, OH, August 10, 1995.
2. C. R. Ananth, S. Mukherjee, and N. Chandra, Computational Analysis of Interfacial Fracture Process in a Push-out Test, Third U. S. National Congress on Computational Mechanics, Dallas, June 12-14, 1995.
3. S. Mukherjee, C. R. Ananth, and N. Chandra, Numerical Modeling of Inelastic Effects in the Evolution of Residual Stresses in Metal Matrix Composites', Third U. S. National Congress on Computational Mechanics, Dallas, June 12-14, 1995.
4. S. R. Voleti, and N. Chandra, Analysis of Large Scale Structures Using Global-Local Finite Element Method', Third U. S. National Congress on Computational Mechanics, Dallas, June 12-14, 1995.

GRADUATE STUDENTS AND POST-DOCTORAL ASSOCIATES

DR. C.R. ANANTH (POST-DOC)

DR. S. MUKHERJEE (Ph. D.)

DR. S.R. VOLETI (Ph. D.)

JOHN WATTS(M.S.)

Contents

1 Overview of the Research Effort	1
1.1 Introduction	1
1.2 Elevated Temperature Interfacial Behavior of MMCs	2
1.3 Effect of Interface Chemistry on the Fracture Properties	2
1.4 Effect of residual stress on interfacial fracture behavior	3
1.5 Evaluation of fracture toughness using thin-slice push-out Tests	4
1.6 Effect of Fiber Fracture and Matrix Yielding on Load Sharing	4
1.7 Effect of Fiber Fracture and Matrix Yielding on Load Sharing	5
1.8 Effect of Interfacial Properties on the Fiber Fragmentation Process	5
1.9 Summary and Conclusion	6
2 Elevated Temperature Interfacial Behavior of MMCs: A Computational Study	7
2.1 Introduction	7
2.2 Modeling the single fiber push-out test	8
2.3 Numerical Implementation	9
2.4 Results and Discussion	10
2.4.1 Interface failure at room temperature	10
2.4.2 Elevated temperature push-out behavior	11
2.4.3 Evaluation of interfacial properties	11

2.4.4	Support distance and its effect on push-out test results at different temperatures	12
2.5	Conclusions	12
3	Effect of Interface Chemistry on the Fracture Properties of Titanium Matrix Composites	24
3.1	Introduction	24
3.2	Evaluation of Interfacial Fracture Toughness of MMCs	25
3.3	Results and Discussion	26
3.3.1	Change in Reaction Zone Size and Composition	26
3.3.2	Evaluation of Interfacial Fracture Toughness from Thin-slice Push-out Tests	28
3.3.3	Observation of the Fracture Surface of Push-out Specimens	29
3.4	Summary and Conclusions	29
4	Effect of Residual Stresses on the Interfacial Fracture Behavior of MMCs	43
4.1	Introduction	43
4.2	Evaluation of Energy Release Rates	44
4.3	Numerical Modeling of the Interface Using Finite Element Methods	47
4.3.1	Simulation of the Single Fiber Push-out test	48
4.4	Results and Discussion:	49
4.4.1	G_i after Specimen Slicing	49
4.4.2	Debond Initiation	51
4.4.3	Application of the EDI Method to Interfacial Crack Propagation	52
4.5	Summary and Conclusions	53
5	Evaluation of Fracture Toughness of MMC Interfaces Using Thin-slice Push-out Tests	70
5.1	Introduction	70

5.2	Numerical Simulation of the Push-out Test Using Finite Element Method . .	71
5.3	Results and Discussion	71
5.4	Summary and Conclusions	74
5.5	Bibliography	74
6	Effect of Fiber Fracture and Interfacial Debonding on the Evolution of Damage in Metal Matrix Composites	80
6.1	Introduction	80
6.2	Damage Mechanics	81
6.3	Monte Carlo simulation	82
6.3.1	Statistical Model for Fiber Strength and its Distribution	82
6.3.2	Fiber-matrix interface	83
6.4	Computational Models	84
6.4.1	Numerical Implementation of the Weibull Model	84
6.4.2	Numerical Implementation of the Monte Carlo Method for modeling fiber breakage	84
6.4.3	Numerical Modeling of interfacial debonding	85
6.4.4	Finite Element Models and Boundary Conditions	85
6.5	Results and Discussion	86
6.5.1	Longitudinal Behavior	86
6.5.2	Transverse Behavior	88
6.5.3	Shear Behavior	88
6.5.4	Evaluation of the damage tensor	89
6.6	Summary and Conclusions	89
7	Effect of Fiber Fracture and Matrix Yielding on Load Sharing in Continuous Fiber Metal Matrix Composites	104
7.1	Introduction	104

7.2	Computational Model	105
7.3	Results and Discussion	105
7.3.1	Effect of Fiber Fracture: Elastic Analysis	106
7.3.2	Effect of Matrix Plasticity	107
7.3.3	Effect of Interfacial Debonding	108
7.3.4	Experimental Comparisons	108
7.3.5	Summary and Conclusions	108
8	Effect of Interfacial Properties on the Fiber Fragmentation Process in Polymer Matrix Composites	124
8.1	Introduction	124
8.2	Interface Model	125
8.3	Statistical Model for Fiber Strength Distribution	127
8.4	Implementation of the model	127
8.5	Results and Discussion	128
8.5.1	Stress Distributions	128
8.5.2	Mean Fragment Length and Saturation	128
8.5.3	Effect of variation in interfacial properties	129
8.5.4	Comparison with Experimental Data	130
8.6	Summary and Conclusions	130
9	Summary and Conclusion	145
9.1	Introduction	145
9.2	Overall goal of the research work	145
9.3	Basic Research Issues	146
9.4	Technical Approach	147
9.5	Significant Results	147

9.6	Relevance to Air Force and Future Direction	148
-----	---	-----

List of Tables

3.1	Interfacial fracture toughness	33
4.1	Material properties for ceramic matrices	57
4.2	Material properties for ceramic matrices	57
4.3	Material properties for ceramic matrices	58
6.1	Material properties of the fiber and matrix	93
6.2	Elastic modulli calculated from FEM and theoretical solutions	93
6.3	Material behavior changes due to damage and plasticity	94
7.1	Material properties of fiber and matrix	112

List of Figures

2.1	Typical push-out test curve with the schematic of the experimental set-up . . .	15
2.2	Push-out experimental results for SiC/Ti-15-3 and SiC/Ti-24-11 composites . . .	15
2.3	Boundary conditions used in the finite element analysis	16
2.4	Residual stresses after step 1; Material: SiC/Ti-15-3	17
2.5	Residual shear stress distribution along the interface at room temperature . . .	18
2.6	Propagation of interface failure in thin-slice push-out test	19
2.7	Variation of residual shear stress along the interface with temperature	20
2.8	Predicted push-out behavior at $T = 23^{\circ}\text{C}$ and $T = 400^{\circ}\text{C}$; $\tau^* = 400.0\text{MPa}$. . .	21
2.9	Variation of failure initiation load with temperature; $\tau^* = 400.0\text{MPa}$	21
2.10	Variation of residual radial stresses along the interface with temperature . . .	22
2.11	Calibration curve to obtain interfacial shear strength from experimental data; $T = 700^{\circ}\text{C}$	23
3.1	Architecture of the SCS-6 SiC Fiber [102]	34
3.2	Interfacial region in a SCS-6/Timetal 21s composite	34
3.3	Finite element model and details of the interface	35
3.4	Variation in reaction zone size with exposure time for SCS-6/Timetal 21s composite heat treated at 927°C	36
3.5	Titanium x-ray scan of an as-processed SCS-6/Timetal 21s specimen (a) line scan (b) dot map	37
3.6	Titanium x-ray scan of a SCS-6/Timetal 21s specimen exposed to 927°C for 120 hours (a) line scan (b) dot map	37

3.7	Silicon x-ray scan of an as-processed SCS-6/Timetal 21s specimen (a) line scan (b) dot map	38
3.8	Silicon x-ray scan of a SCS-6/Timetal 21s specimen exposed to 927° C for 120 hours (a) line scan (b) dot map	38
3.9	Typical load displacement curve for a push-out test conducted on an as-processed specimen	39
3.10	Typical load displacement curve for a push-out test conducted on a specimen subjected to 927° C for 25 hours	39
3.11	Composite of the push-out test results	40
3.12	Bottom fracture surface for a 700° C heat treated push-out specimen	41
3.13	Bottom fracture surface for a 927° C heat treated push-out specimen	42
4.1	Contours used in the Equivalent Domain Integral Method	59
4.2	Typical path used in the energy release rate computations	60
4.3	Finite element model and details of the interface	61
4.4	Variation of material properties with temperature	62
4.5	Boundary conditions used in the Finite Element Analysis	63
4.6	Shear stress distributions along the interface for specimen thickness of 0.5 mm	64
4.7	Percentage error in energy release rates calculated using the axial fiber residual stress plotted as a function of the ratio of the matrix modulus to the fiber modulus	65
4.8	Variation of the energy release rates from the end of the processing stage till debond initiation as a result of indenter load application	65
4.9	Variation of axial and radial components of residual stress in the fiber with equivalent plastic strain induced in the matrix as a result of straining	66
4.10	Variation of energy release rates till debond initiation upon application of load by the indenter after straining to 0.9 % total strain	66
4.11	Variation of energy release rates till debond initiation upon application of load by the indenter after straining to 1.3 % total strain	67
4.12	Variation of energy release rates till debond initiation upon application of load by the indenter after straining to 1.5 % total strain	67

4.13	Variation of energy release rates till debond initiation upon application of load by the indenter for ceramic matrix composites	68
4.14	Crack tip locations for the loading and support ends from the end of processing stage till the fiber gets pushed out	68
4.15	Variation of energy release rates from the end of processing stage till the fiber gets pushed out	69
5.1	finite element model	76
5.2	profilometry-as received specimen	77
5.3	profilometry-as received specimen	78
5.4	shear stress for residual stress case	78
5.5	profilometry-as received specimen	79
5.6	shear stress for no residual stress case	79
6.1	Flow-chart of the Monte Carlo simulation	95
6.2	Spring-layer model for fiber-matrix interface	96
6.3	Schematic of the 0^0 lamina and boundary conditions	97
6.4	Schematic of the 3-fiber model and boundary conditions	97
6.5	Schematic and boundary conditions of the finite element model to study transverse behavior	98
6.6	Schematic diagram of the loading and boundary conditions of the 45^0 ply model	98
6.7	(a) Stress-strain curves for 0^0 degree laminae, (b) fracture pattern for a 35 % volume fraction lamina	99
6.8	Fracture pattern for a 16 % fiber volume fraction lamina	100
6.9	Experimental results	100
6.10	Load-displacement curves for pre-determined damage patterns	101
6.11	Propagation of plastic front in the case of broken fiber with debonding	101
6.12	Variation of axial stress in the intact fiber upon debonding of the broken fiber	102
6.13	Stress-strain curve for a weakly-bonded, transversely-loaded composite . . .	102

6.14	Stress vs. longitudinal strain for 45°-lamina	103
7.1	Finite element model with boundary conditions	113
7.2	axial elastic broken	114
7.3	axial elastic y	114
7.4	axial elastic x	115
7.5	x disp bending	115
7.6	nonuniform stress bending	116
7.7	propagation vf 35	117
7.8	P-delta vf 35	117
7.9	variation pl str fiber length vf 35	118
7.10	variation stress fiber length vf 35	119
7.11	variation stress fiber length vf 16	119
7.12	propagation vf 16	120
7.13	variation pl str fiber length vf 16	121
7.14	plasticity with debonding	121
7.15	stress debonding vf 35	122
7.16	slip bands	123
8.1	Stress distribution with no debonding. (a) axial stress in the fiber; (b)interfacial shear stress	133
8.2	Stress distribution with partial debonding. (a) axial stress in the fiber; (b) interfacial shear stress	133
8.3	Flow chart for the simulation of the fiber fragmentation test	134
8.4	Axial stress in fiber with strong bond (a) at intermediate applied strain, (b) high strain	135
8.5	Axial stress profile with debonding (a) at initial loading and intermediate stages, (b) at saturation	136
8.6	Number of breaks vs. applied strain (perfect bonding)	137

8.7	(a):Variation of average fragment length with applied strain for a strong bond.	
	(b):Variation of average fragment length with applied strain for a weak bond.	138
8.8	Number of breaks vs. applied strain (bond strength = 60 MPa, frictional stress = 20 MPa).	139
8.9	Variation of debonding with applied strain	139
8.10	Variation of mean fragment length with bond strength.	140
8.11	Fragment length distribution with increasing bond strength (1 link = 4 microns)	141
8.12	Variation of mean fragment length with frictional stress	142
8.13	Comparison of the numerical values with experimental results	142
8.14	debond-length friction	143
8.15	exp comp lm	144

Chapter 1

Overview of the Research Effort

This research was focused on the effect of processing on the evolution of interfaces in metal matrix composites (MMCs). The effort was carried out in two different hierarchical levels (micromechanical and macroscopic) using both experimental and computational methods. Significant work was carried out in understanding the origin of interfacial mechanical properties and hence was performed at the micromechanics level. The report consists of about ten chapters spanning different aspects of the problem. While the first eight attempts to characterize the interface in terms of its thermomechanical properties, the last two use the concept developed in the earlier chapters to design composites for practical applications.

1.1 Introduction

Metallic and Intermetallic Matrix Composites (MMCs and IMCs) are being considered for crucial applications in the aerospace industry because of their high specific stiffness and strength even at elevated temperatures ($> 600^{\circ}\text{C}$). A critical issue in the successful application of these composites is the behavior of fiber-matrix interfaces. Push-out test is emerging as an important experimental tool for characterizing the interfacial behavior of this class of composites, mainly after its widespread use in Ceramic Matrix Composites (CMCs).

When MMCs and IMCs are cooled after processing from a stress free temperature, residual stresses arise due to the difference in the coefficients of thermal expansion (CTE) of fiber and matrix materials. These stresses reach considerable levels because, in typical titanium based MMCs and IMCs such as SiC/Ti-6Al-4V, SiC/Ti-15V-3Sn-3Al, SiC/Ti-24Al-11Nb the mismatch in the CTE is quite significant ($\alpha_{\text{matrix}} \geq 2\alpha_{\text{fiber}}$) and also the temperature differential involved in the cooling process is high (about 800°C). These stresses cause matrix cracking near the interface on processing and also affect the interfacial response of these composites under service conditions.

1.2 Elevated Temperature Interfacial Behavior of MMCs

The thermomechanical behavior of fiber-matrix interfaces play an important role in the successful application of this class of composites. Push-out test is emerging as an important experimental tool for characterizing the interfacial behavior of MMCs and IMCs. In this study, single fiber push-out test is modeled using the finite element method, with the objective of studying the interface failure process, and extracting interfacial properties from the experimental test results. Earlier studies by the author's group emphasize the significance of processing induced residual stresses in titanium based composites and their effects on push-out test results. In the present work, the developed methodology is used to study the interfacial behavior during push-out tests at elevated temperatures. An attempt is made in Chapter 2 to predict interfacial shear strengths at elevated temperatures, by correlating the numerical simulations and the experimental results.

In this chapter, it is shown that residual shear stresses affect the peak push-out load as well as the failure initiation load at elevated temperatures. The average shear strength ($\tau_{exp}^p = P_{max}/\pi dL$) evaluated from the peak push-out load does not reflect the actual shear strength of the interface, since it is influenced by the presence of processing induced residual stresses and other geometric and testing variables. Numerical predictions show that for SiC/Ti-15-3 the intrinsic interfacial shear strength (which is a material property) is about four times τ_{exp}^p at room temperature and drops to 2.0 at 700°C. The support distance in the experimental set-up has to be controlled properly at elevated temperatures to minimize the specimen bending effects.

1.3 Effect of Interface Chemistry on the Fracture Properties

In Chapter 3, the effect of fiber-matrix interfacial reactions on the fracture properties of the interface is studied using experimental characterization and computational modeling techniques. The objective of this study is to establish a link between the evolution of the interfacial chemistry and the resulting mechanical properties. SCS-6/Timetal21s composite is chosen as the candidate material system. The composite specimens are exposed to temperatures as high as 927°C for extended hours. The diffusion of elements across the interface is investigated through metallurgical techniques. Fiber push-out is used to characterize the mechanical properties of the interface. A novel computational method is used to simulate the propagation of interfacial cracks during the tests. The fracture toughness of the interface is evaluated from the experimental data using this model.

The evolution of interface in SCS-6/Timetal 21s composite system is shown in Chapter 3 by means of heat treatment experiments, with the objective of establishing a link between the evolution of chemistry and geometry of the reaction zone and the interfacial properties.

- Microstructural studies reveal that reaction growth is due to transformation of both coating and the matrix. The growth of the reaction zone into the matrix is much more than the growth towards the fiber, as carbon is able to diffuse much farther into the matrix than the diffusion of Titanium into the fiber.
- Reaction zone sizes increase rapidly with time at 927° C. At lower temperatures such as 700° C and 450° C no significant increase in reaction zone size is observed for this system.
- Push-out tests conducted on heat treated specimens reveal that the effect of thermal exposure on interfacial properties is predominantly due to exposure temperature. Time of exposure is found to have only a secondary effect.
- Fracture toughness values remain more or less constant for normal use temperatures in the range of 450° to 700° C. The values however, increase when the exposure temperature is raised to 927° C.
- Fracture surfaces of the specimens exposed at 927° C show that debonding took place in the reaction zone whereas in as-processed specimens and those heat treated at the lower temperature ranges debonding initiated in the coating. This is because the weak region in the coating is replaced by the stronger interfacial region.

1.4 Effect of residual stress on interfacial fracture behavior

A fracture mechanics approach is used in Chapter 4 to examine the interfacial debonding process in MMCs and CMCs during a fiber push-out test. The Equivalent Domain Integral (EDI) method is implemented in a finite element code and is used to compute the strain energy release rates for the interface crack. The cooling process from the composite consolidation temperature, specimen preparation for the push-out test and the actual testing are included in the finite element simulation. A strain energy based debonding criterion is used to predict the interfacial behavior. The experimentally observed phenomenon of bottom debonding in MMCs is explained from the energy release rate variation for the loading and support end cracks. It is shown that processing induced residual stresses significantly affect the initiation and propagation of interface cracks. The advantage of the EDI method over conventional methods for modeling interface crack propagation, by eliminating the need for singular elements and thus remeshing with crack advance is demonstrated through the simulation of the push-out test.

Strain energy release rates for the fiber-matrix interface due to processing induced residual stresses are determined by the above method. These rates serve as a lower bound for the Mode II fracture toughness of the composite systems examined. The phenomenon of bottom (support end) debonding observed in MMC systems during the push-out test is explained by the study of the variation of energy release rates for the loading and support end

cracks upto debond initiation. The effect of residual stresses on crack initiation is studied by altering the residual stress state by plastic straining. It is found that crack initiation switches from the support to the loading end with reduction in residual stresses with increase in plastic strain. For the specimen geometry and material system studied, this switching occurs when the G_{ir} values drop to values of the order of $4J/m^2$ from the as-received value of around $40J/m^2$. It is shown that the EDI method can be used to simulate interface crack propagation without the need for remeshing with crack advance. Evaluation of strain energy release rates through the use of J-integral for cracks along bimaterial interfaces in the presence of friction is still a "mathematical problem" and care needs to be exercised in the interpretation of the numerical predictions.

1.5 Evaluation of fracture toughness using thin-slice push-out Tests

Push-out test has emerged as an important experimental tool for characterizing the interface behavior of MMCs mainly after its widespread use in the study of interfaces in ceramic matrix composites (CMC). The presence of high levels of residual stresses in MMCs alters the mechanics of the failure process, making the interpretation of test results and evaluation of interfacial properties very difficult. Moreover the relatively high bond strength of MMCs and residual clamping stresses at the interface limit the specimen thickness for push-out experiments. In the thin slice push-out tests it is observed that interface failure initiates from the bottom of the specimen and not from the loading end as in the case of CMCs. In Chapter 5, fracture toughness (G_{ic}) is considered as a more appropriate quantitative measure of the bond at the interface. The interfacial fracture energies of metal matrix composites are not currently available in the literature because of the difficulty in evaluating these from the experimental results.

In this chapter, a numerical method based on the equivalent domain integral technique developed previously is used to simulate the fracture process during a thin slice push-out test and determine the critical interfacial fracture toughness G_{ic} . Experimental correlations are made with push-out test results of ceramic matrix composites to validate the G_{ic} predictions using the EDI method. This approach is then used to evaluate the G_{ic} of some as processed SCS-6/Titanium matrix composites from the experimental data.

1.6 Effect of Fiber Fracture and Matrix Yielding on Load Sharing

Chapter 6 addresses the issue of stress re-distribution in the presence of a fiber fracture in a composite lamina. Stress elevation in the fiber adjacent to the broken fiber is the focus of this study. The stress concentration effects in the vicinity of the fiber break and its influence

on the neighboring intact fiber is analyzed using finite element method as a function of fiber volume fraction. The role of the inelastic behavior of the matrix in causing the stress elevation is studied. It is found that the state of stress in the intact fiber is significantly affected by the propagation of plastic front due to matrix yielding. The local stress field is affected also if the fiber break is followed by interfacial debonding. Titanium matrix reinforced with continuous fibers of silicon carbide is chosen as the metal matrix composite system for this study. Experimental comparisons are made with tensile tests conducted using a single ply lamina.

1.7 Effect of Fiber Fracture and Matrix Yielding on Load Sharing

A new approach for modeling the behavior laminated composite structures using computational methods is presented in Chapter 7 considering the damage evolution at the micromechanical level. Micromechanical models are developed to predict the stress-strain response of a composite lamina explicitly accounting for the local damage mechanisms such as fiber fracture and interfacial bonding. The model is applied to metal matrix composites and hence the inelastic constitutive behavior of the matrix phase is included. The stochastic variation of the fiber properties is incorporated in this simulation using the two-parameter weibull model. The effect of fiber volume fraction and the properties of the fiber, matrix and interface on the damage evolution is studied using this approach. A constitutive damage tensor for the composite lamina is developed from the micromechanical models which can be input into laminate structural analysis codes.

1.8 Effect of Interfacial Properties on the Fiber Fragmentation Process

Fiber Fragmentation Test or Single Fiber Composite Test (SFC) has been widely used to characterize the interfacial behavior in composites. Though it is accepted that SFC gives useful information about the interfacial bond quality and the fiber strength, there is no clear consensus on how to interpret the data and quantify the interfacial properties. In this paper, the fiber fragmentation test is modeled with the objective of studying the effect of interfacial bond strength and post-debonding frictional effects on the progress of the fragmentation process. The load transfer at the fiber-matrix interface is modeled using the shear-lag principles and the statistical variation of fiber strength is incorporated using Weibull theory. A parametric study of the variation of interfacial shear properties on the mean fragment length and debond progression with applied strain is conducted. It is found that in the case of weak interfaces saturation of fiber fragments occurs at much lower applied strain values and is usually associated with extensive debonding. The numerical simulation shows that the fragmentation results are very much sensitive to the frictional effects as it

controls the debonded length. The results from the model are correlated with experimental data to validate the model and for extracting the interfacial properties from the test data.

1.9 Summary and Conclusion

The final chapter summarizes the goal of the research, technical approach taken, and some of the significant findings. Future research direction to pursue this work is also suggested.

Chapter 2

Elevated Temperature Interfacial Behavior of MMCs: A Computational Study

2.1 Introduction

Metallic and Intermetallic Matrix Composites (MMCs and IMCs) are being considered for crucial applications in the aerospace industry because of their high specific stiffness and strength even at elevated temperatures ($> 600^{\circ}\text{C}$). A critical issue in the successful application of these composites is the behavior of fiber-matrix interfaces. Push-out test is emerging as an important experimental tool for characterizing the interfacial behavior of this class of composites, mainly after its widespread use in Ceramic Matrix Composites (CMCs).

When MMCs and IMCs are cooled after processing from a stress free temperature, residual stresses arise due to the difference in the coefficients of thermal expansion (CTE) of fiber and matrix materials. These stresses reach considerable levels because, in typical titanium based MMCs and IMCs such as SiC/Ti-6Al-4V, SiC/Ti-15V-3Sn-3Al, SiC/Ti-24Al-11Nb the mismatch in the CTE is quite significant ($\alpha_{matrix} \geq 2\alpha_{fiber}$) and also the temperature differential involved in the cooling process is high (about 800°C) [3]. These stresses cause matrix cracking near the interface on processing and also affect the interfacial response of these composites under service conditions.

Push-out tests involve application of compressive load through a flat indenter to push a fiber out of a composite specimen. A schematic of the experimental set-up and a typical push-out curve are shown in Fig. 2.1. The cross head displacement is plotted along the x-axis. Applied load, P or average interfacial shear stress, τ is plotted along the y-axis. τ is

evaluated from P using the relationship

$$\tau = \frac{P}{\pi d L} \quad (2.1)$$

where d is the diameter of the fiber, and L is the length of the specimen. Eldridge et al. [9] conducted *thin-slice* push-out tests of SiC/Ti-15-3 and SiC/Ti-24-11 composites (Fig. 2.2) at various temperatures. In this figure, the average shear stress evaluated from equation (1) is plotted against the cross head displacement. F_{max} (or τ^p) and P_{fr} (or τ^{fr}) are the two parameters reported from the push-out tests.

The higher bond strength of MMCs and IMCs compared to CMCs limit the specimen thickness for push-out tests in MMCs to a value less than 1.0 mm (with thickness less than 0.5 mm being the most common), due to experimental problems such as fiber damage during loading or failure of the indenter [5]. Previous work by Ananth and Chandra [3] indicates that processing induced residual stresses considerably influence the debonding sequence during push-out tests at these thicknesses and makes the interpretation of the test results difficult. Nonlinear finite element method was used in that work to model the propagation of interface failure during push-out tests. They showed that the intrinsic shear strength of the interface can be very much different than τ^p from the experiment; and, developed a methodology to evaluate the interfacial properties by correlating the numerical predictions with the experimental data. In this work, the comprehensive analysis procedure developed by the authors [3, 7] is used to study the interfacial behavior during push-out tests at elevated temperatures.

2.2 Modeling the single fiber push-out test

The single fiber push-out test is analyzed using axisymmetric cylindrical models. A two phase unit cell consisting of a fiber and matrix is used with periodic boundary conditions at the outer radius ($u_r = \text{constant}$) to represent the composite. The interface is modeled as a region of negligible thickness [7, 8, 9, 26] possessing the required stiffness and strength. A stress based criterion for debonding, and frictional resistance based criterion for interfacial sliding are used to capture debonding and sliding which are presumed to occur in a chronological sequence with increasing load. Debonding is postulated to occur under the combined action of normal tensile stress which could cause mode I failure and shear stress which could cause mode II failure at the interface. A quadratic stress based failure theory

$$F(\sigma) \equiv \left(\frac{\sigma_r}{\sigma_r^f} \right)^2 + \left(\frac{\tau}{\tau^f} \right)^2 \geq 1 \quad (2.2)$$

is applied [25, 26] where σ_r^f is the interfacial strength in the normal direction resisting crack opening, and τ^f is the effective shear strength of the interface. In the above equation the effect of σ_r is included only when it is positive. Subsequent to the debonding process, interfacial frictional sliding occurs in the mating debonded surfaces according to Coulomb's law.

Any contact pressure at the interface will result in an increase in the value of τ^f , which is then evaluated as

$$\begin{aligned} \tau^f &= \tau^* + \mu p \quad \text{with } p = -\sigma_r \text{ if } \sigma_r < 0 \\ p &= 0 \quad \text{if } \sigma_r \geq 0 \end{aligned} \quad (2.3)$$

where τ^* is the shear strength of the interface (the shear stress required to break the bond), p is the contact pressure at the interface, and μ is the coefficient of friction. σ_r^f is taken to be equal to be of the same order as τ^* [26] in the absence of any experimental data.

2.3 Numerical Implementation

The problem is analyzed by assuming axial symmetry. The interface is modeled using a contact-friction formulation [7] and the fiber-matrix bonding is simulated by connecting the nodes at the interface by means of high stiffness springs. MARC finite element software is used to perform the analysis along with external subroutines. The stresses at the interface are monitored in these subroutines and the stiffness of the springs is dropped to a negligible value once the failure criterion is satisfied, indicating the onset of frictional sliding. Coulomb's law is used to model the frictional behavior. The coefficient of friction μ is approximately calculated from the relation $\mu = \frac{\tau^{fr}}{p_{res}}$, where τ^{fr} is the average frictional stress from the push-out experiment, and p_{res} is the average residual contact pressure (at the interface) from the numerical results.

Elastic constitutive behavior is assumed for the fiber phase. Matrix is assumed to be a rate independent elastic-plastic material. The temperature dependency of the elastic and inelastic properties of the constituent phases are included in the analysis in a piece-wise linear manner, for different titanium based matrices and silicon carbide (SCS-6) fiber [3, 21, 13].

To simulate the thin-slice push-out test, the analysis is done in three steps. The boundary conditions for these steps are shown in Fig. 4.5.

1. In the first step (Fig. 4.5a) the cooling process after composite consolidation at high temperature is modeled. A reference temperature T_{ref} is assumed above which the composite is stress free.
2. The second step (Fig. 4.5b) models the specimen preparation process. This is simulated by removing the existing tying constraints and boundary conditions from the top and bottom faces and allowing the stresses in the specimen to reach equilibrium, symmetrical about a plane passing through the center of specimen thickness. This process results in shear stresses at the interface due to differential axial residual strains between the fiber and matrix.

3. The push-out load is applied by prescribing displacements to a rigid punch, till the fiber is pushed through. The boundary conditions used in this step are shown in Fig. 4.5(c). The clearance between the supporting hole and the fiber diameter is made as small as possible to minimize bending.

The interface failure criterion is checked during steps 2 and 3 to detect the possibility of debonding. Hence, if the residual shear stresses are high and the bonding at the interface is weak, then debonding can occur, even before the application of punch load.

2.4 Results and Discussion

The push-out test is numerically modeled with SiC/Ti-15-3 MMC as the model material system. The silicon carbide fiber used in this study is the SCS-6 type (continuous fibers) with $140\mu\text{m}$ fiber diameter. The reference temperature at which the composite is stress free is taken to be 815°C [13]. Fiber volume fraction of 35%, specimen thickness of 0.45 mm and an indenter of $125\mu\text{m}$ diameter are used so that the numerical predictions can be compared with the experimental results of Eldridge et al. [9].

2.4.1 Interface failure at room temperature

The 3-step numerical procedure outlined in the previous section is used to simulate the interfacial failure process during push-out test. Residual stress state in the bulk composite after the cooling process is shown in Fig. 2.4 (step 1). It can be seen that axial compressive stresses (σ_z) of the order of 750 MPa is produced in the fiber and a corresponding tensile stress is produced in the matrix due to the thermal mismatch between the fiber and the matrix. The radial stress (σ_r) is compressive at the interface and acts as a clamping force on the fiber. Step 2 which models the specimen preparation process results in considerable amount of shear stresses at the ends (Fig. 2.5) due to the removal of boundary constraints. The effect of this shear stress is to push the fiber (which is under axial compression) out of the matrix at both the ends. Adequate modeling of the end effects through mesh refinement reveals that the end points of the specimen debond due to the combined effect of the high levels of shear stresses and radial normal stresses (resulting from the local bending of the matrix). When an axial load is applied to the fiber under these conditions, debonding starts from the far end (or support end) and progresses towards the punch end (Fig. 7.15). Fig. 7.15a shows the residual shear stress state and (b), (c), (d) and (e) are the stress states at increasing punch displacements. It can also be seen from Fig. 7.15 that the fiber protrudes outside in the axial direction at the support end, as the residual axial compressive stresses are relieved in the debonded region. This is contrary to the normally observed debonding behavior in CMCs where the interface failure always initiates at the loading end. A detailed study of this phenomena can be found in reference [8, 3].

2.4.2 Elevated temperature push-out behavior

Residual stresses decrease with increase in temperature. This results in a decrease in the axial strain mismatch between the fiber and matrix phases thus reducing the residual shear stress at the interface as shown in Fig. 2.7. The push-out test is numerically simulated at 23°C and 400°C assuming a constant value of interfacial shear strength ($\tau^* = 400.0$ MPa) in this temperature range, and the results are shown in Fig. 2.8. We can see from this figure and from Fig. 2.9 that the peak load P_{max} increases with temperature. This is because the reduction in shear stresses at elevated temperatures requires a larger load for failure initiation from the support end. Fig. 2.9 also shows the plot of debond initiation load P_i with temperature. The debonding sequence indicates that the failure under these conditions of temperature and thickness, still initiates from the support end. It can be seen from Fig. 2.9 that the difference between P_{max} and P_i decreases with increase in temperature. This can be attributed to the reduction in residual shear stresses at the loading end at elevated temperatures which causes the resistance to further debonding to decrease as the crack propagates towards the loading end.

Apart from the shear stresses, radial clamping stresses at the interface also decrease with increase in temperature as shown in Fig. 2.10. The effect of this drop can be seen from the significant reduction in τ_{fr} from 23°C to 400°C in Fig. 2.8. The coefficient of friction μ is taken as 0.25 in these calculations.

2.4.3 Evaluation of interfacial properties

The experimental data of τ_{exp}^p at different temperatures for SiC/Ti-15-3 composite is available from Fig. 2.2 [9]. But τ_{exp}^p is only an average value and is not a measure of the actual shear strength of the interface [7]. The intrinsic shear strength of the interface which is a material property, could be higher than the τ_{exp}^p which is computed from the peak load from push-out test, using equation (1). Thus one of our main objective is to establish a quantitative relationship between the experimental value τ_{exp}^p and the intrinsic shear strength τ^* , for MMCs and IMCs. In the present study, the average interfacial shear stress corresponding to the peak load τ_{comp}^p , is evaluated from finite element simulation for different values of τ^* (Fig. 2.11). This serves as a calibration curve from which the material shear strength τ^* can be evaluated. We can now define an Interface Strength Factor, K_s as

$$K_s = \frac{\tau^*}{\tau_{exp}^p} \quad (2.4)$$

where τ^* is the intrinsic shear strength of the interface and τ_{exp}^p is the average interfacial shear stress corresponding to peak push-out load P_{max} from the experiment. K_s is found to be in the range of 4.0 from room temperature to 400°C and drops to about 2.0 at about 700°C.

2.4.4 Support distance and its effect on push-out test results at different temperatures

Kallas et al. [5] found that in niobium/sapphire MMC system specimen bending under push-out load is a problem, especially at very low aspect ratios L/h , where L is the thickness and h is the distance between the bottom supports in Fig. 2.1. This results in tensile normal stresses at the bottom surface which causes interface failure to initiate from the bottom even in the absence of residual shear stress. To determine the effect of support distance in the material system under consideration, the numerical simulation is repeated at different L/h ratios ranging from 2.2 to 3.3. The results indicate that the peak push-out load reduces with reduction in L/h ratio; but the effect is significant only at higher temperatures. The variation of the peak push-out load is found to be about 3% at temperatures less than 400°C; but, increases to 15% at 700°C. This is due to the reduction in the mechanical properties of the material at elevated temperatures.

2.5 Conclusions

Residual shear stresses affect the peak push-out load as well as the failure initiation load at elevated temperatures. The average shear strength ($\tau_{exp}^p = P_{max}/\pi dL$) evaluated from the peak push-out load does not reflect the actual shear strength of the interface, since it is influenced by the presence of processing induced residual stresses and other geometric and testing variables. Numerical predictions show that for SiC/Ti-15-3 the intrinsic interfacial shear strength (which is a material property) is about four times τ_{exp}^p at room temperature and drops to 2.0 at 700°C. The support distance in the experimental set-up has to be controlled properly at elevated temperatures to minimize the specimen bending effects.

Bibliography

- [1] N. Chandra, C. R. Ananth, and H. Garmestani. Micromechanical Modeling of Process Induced Residual Stresses in Ti-24Al-11Nb/SCS-6 Composite. *Journal of Composites Technology and Research*, 16(1):37–46, 1994.
- [2] C. R. Ananth and N. Chandra. Numerical Modeling of Fiber Push-out Test in Metallic and Intermetallic Matrix Composites - Mechanics of the Failure Process. *Journal of Composite Materials*, 29(11):1488–1514, 1995.
- [3] S. M. Arnold, V. K. Arya, and M. E. Melis. Elastic/Plastic Analyses of Advanced Composites Investigating the Use of the Compliant Layer Concept in Reducing Residual Stresses Resulting from Processing. Technical Report NASA TM 103204, NASA, 1990.
- [4] J. I. Eldridge. Fiber Push-out Testing of Intermetallic Matrix Composites at Elevated Temperatures. In D. B. Miracle, D. L. Anton, and J. A. Graves, editors, *Intermetallic Matrix Composites II*, MRS Symposium Proceedings, volume 273, pages 325–330. Materials Research Society, 1992.
- [5] M. N. Kallas, D. A. Koss, H. T. Hahn, and J. R. Hellman. Interfacial Stress State Present in a Thin-slice Fibre Push-out test. *Journal of Materials Science*, 27:3821–3826, 1992.
- [6] N. Chandra and C. R. Ananth. Analysis of Interfacial Behavior in MMCs and IMCs using Thin-slice Push-out Tests. *Composites Science and Technology*, 54(1):87–100, 1995.
- [7] J. Aboudi. Damage in Composites - Modeling of Imperfect Bonding. *Composites Science and Technology*, 28:103–128, 1987.
- [8] A. Needleman. A Continuum Model for Void Nucleation by Inclusion Debonding. *Journal of Applied Mechanics*, 54:525–531, 1987.
- [9] H. Zhu and J. D. Achenbach. Radial Matrix Cracking and Interphase Failure in Transversely Loaded Fiber Composites. *Mechanics of Materials*, 11:347–356, 1991.
- [10] M. R. Wisnom. Micromechanical Modeling of the Transverse Tensile Ductility of Unidirectional Silicon Carbide/6061 Aluminum. *Journal of Composites Technology and Research*, 14(1):61–69, 1992.

- [11] Z. Hashin. Failure Criteria for Unidirectional Fibre Composites. *Journal of Applied Mechanics*, 47:329-334, 1980.
- [12] R. P. Nimmer, R. J. Bankert, E. S. Russel, G. A. Smith, and P. K. Wright. Micromechanical Modeling of Fiber-Matrix Interface Effects in Transversely Loaded SiC/Ti-6-4 Metal Matrix Composites. *Journal of Composites Technology and Research*, 13(1):3-13, Spring 1991.
- [13] B. S. Majumdar and G. M. Newaz. Isothermal Fatigue Mechanisms in Ti-Based Metal Matrix Composites. Technical Report NASA CR 191181, NASA, 1993.

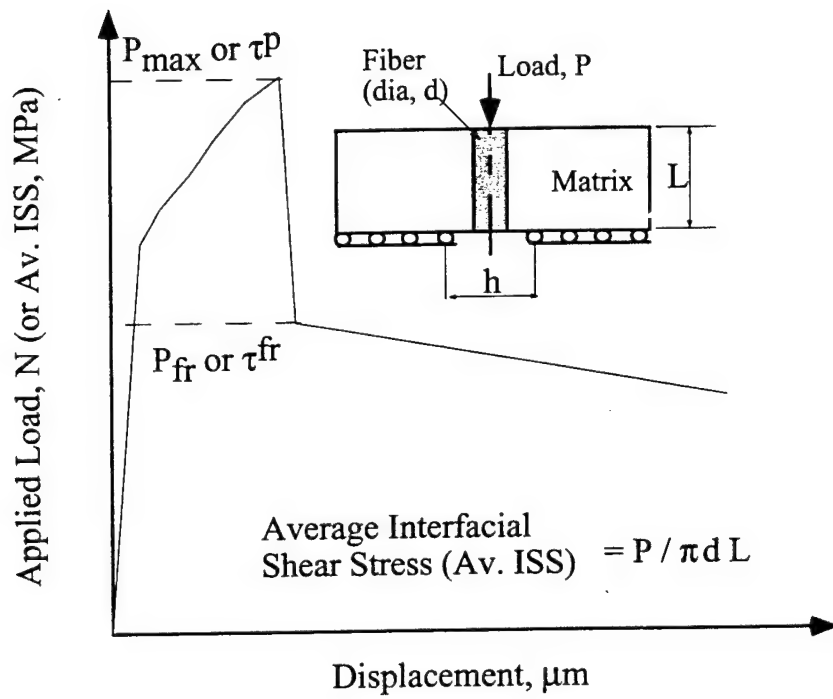


Figure 2.1: Typical push-out test curve with the schematic of the experimental set-up

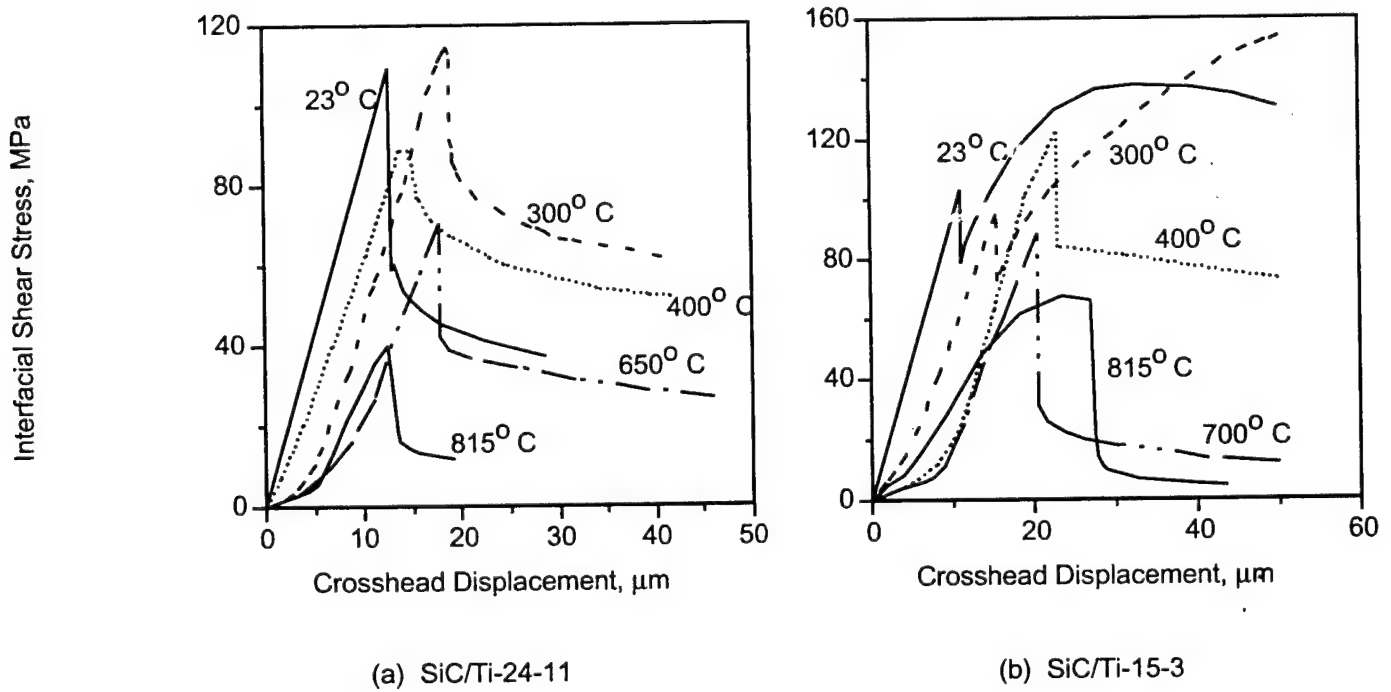


Figure 2.2: Push-out experimental results for SiC/Ti-15-3 and SiC/Ti-24-11 composites

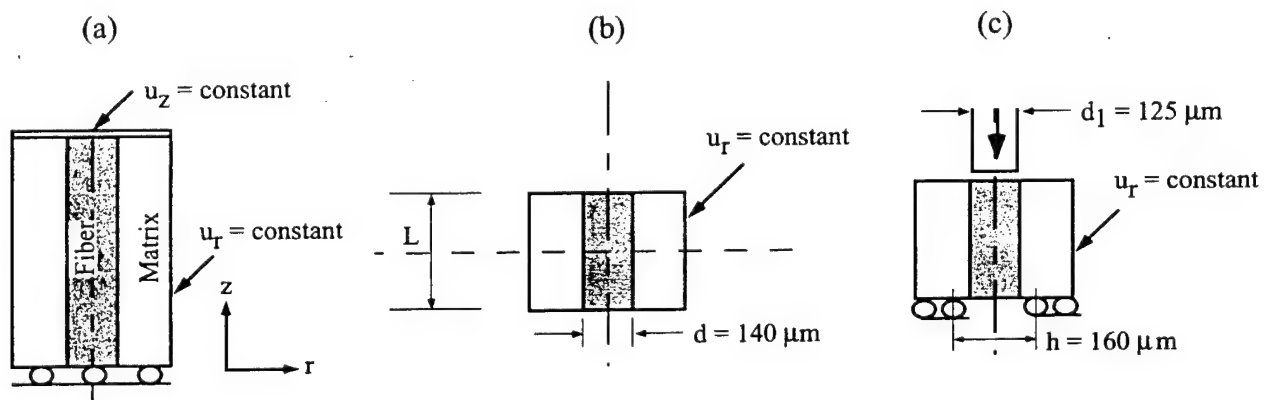


Figure 2.3: Boundary conditions used in the finite element analysis

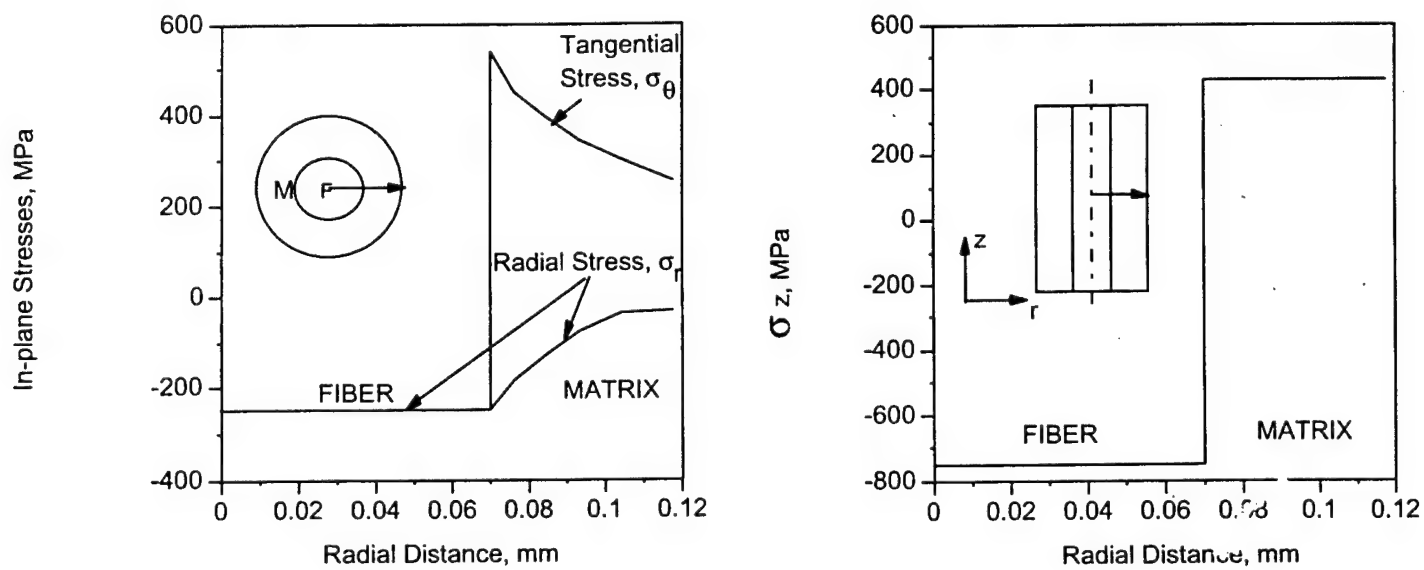


Figure 2.4: Residual stresses after step 1; Material: SiC/Ti-15-3

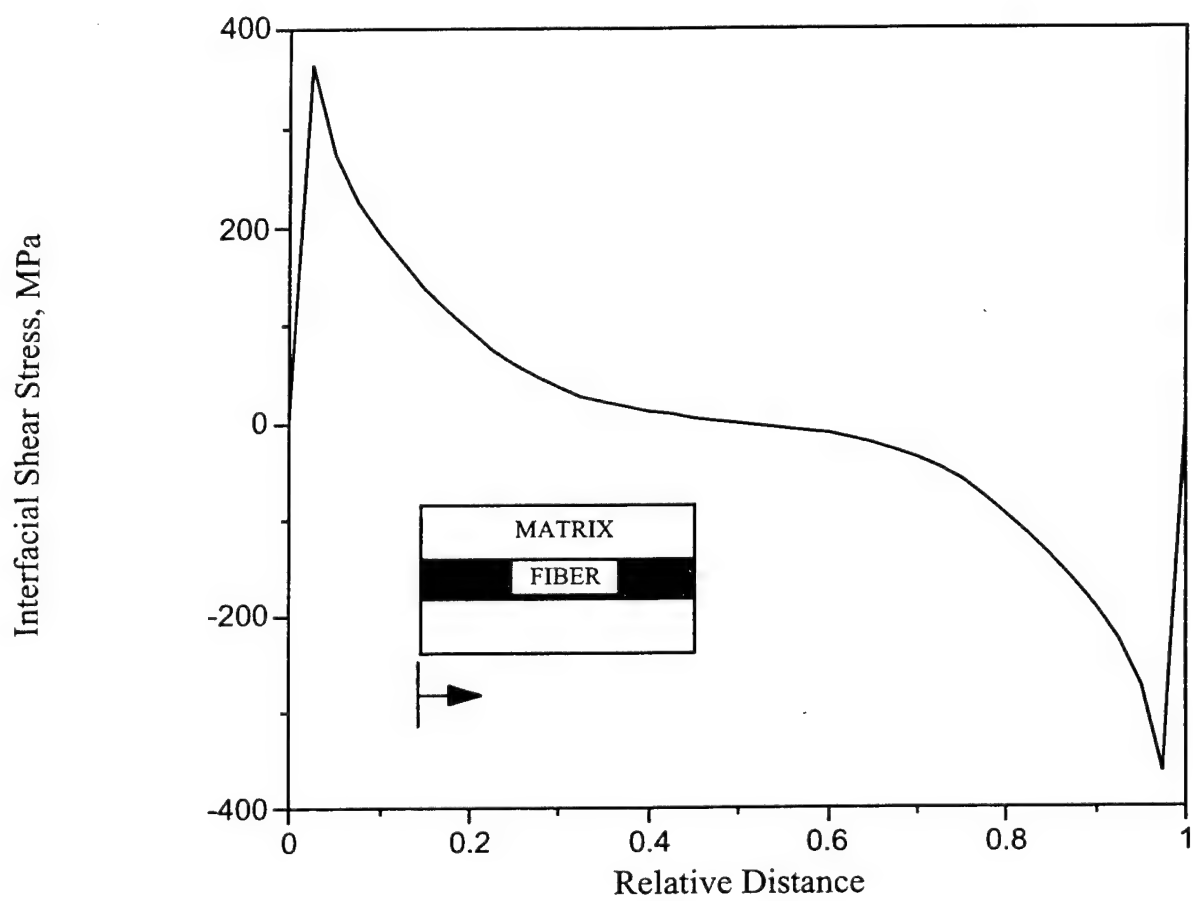


Figure 2.5: Residual shear stress distribution along the interface at room temperature

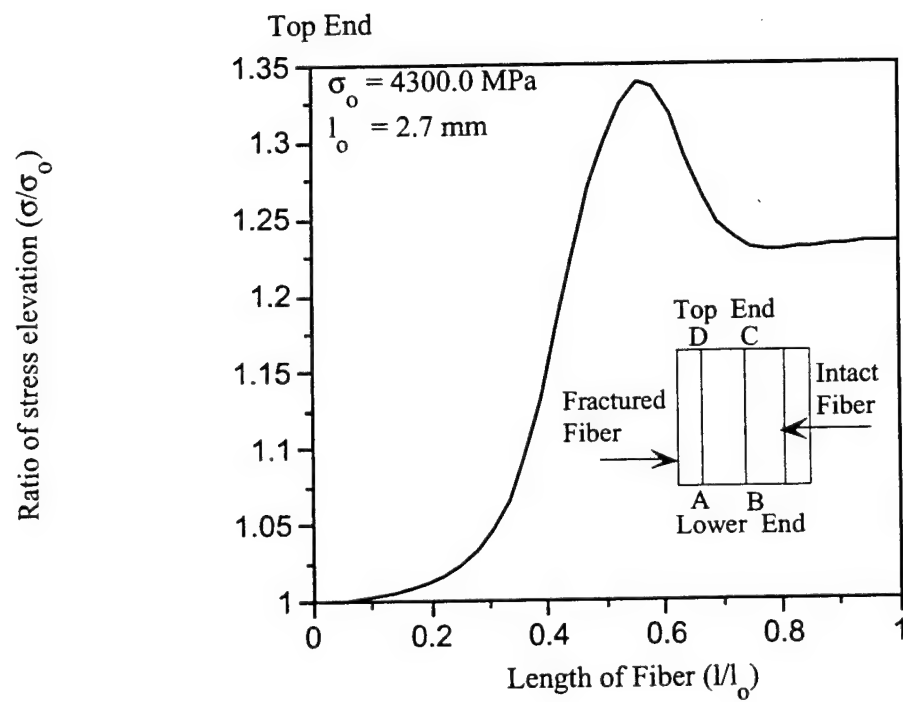


Figure 2.6: Propagation of interface failure in thin-slice push-out test

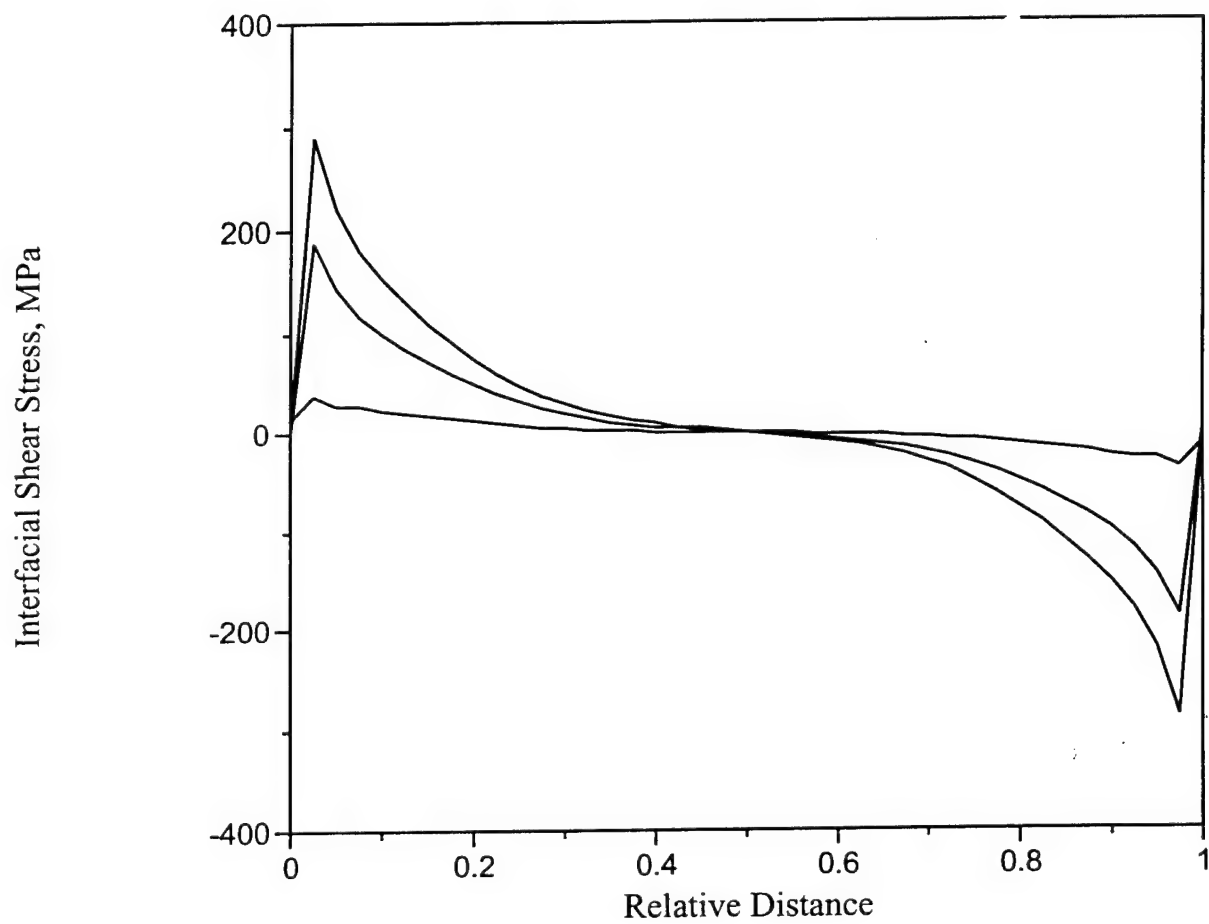


Figure 2.7: Variation of residual shear stress along the interface with temperature

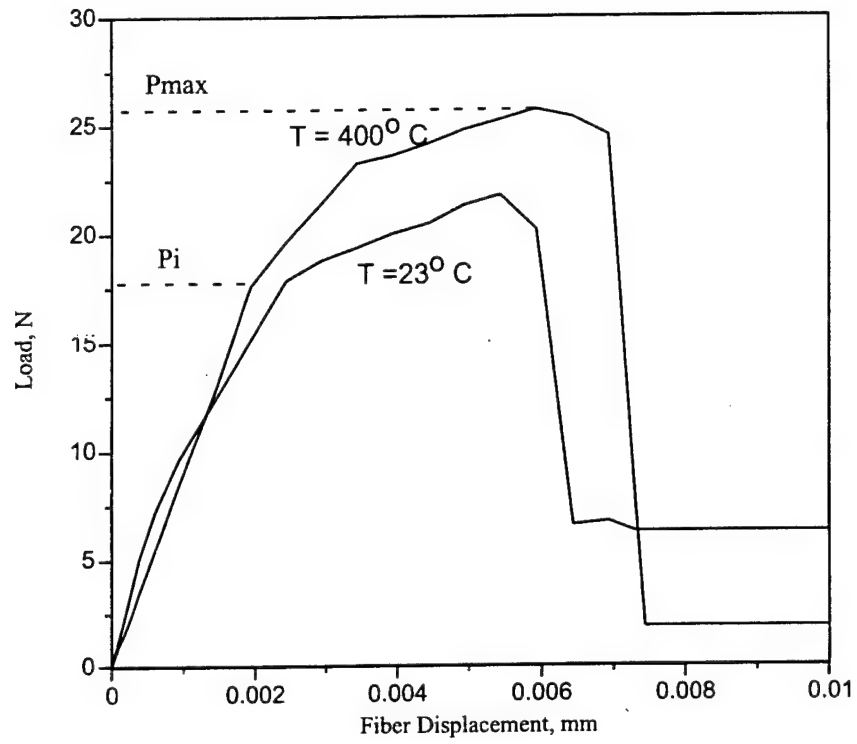


Figure 2.8: Predicted push-out behavior at $T = 23^{\circ}\text{C}$ and $T = 400^{\circ}\text{C}$; $\tau^* = 400.0\text{MPa}$

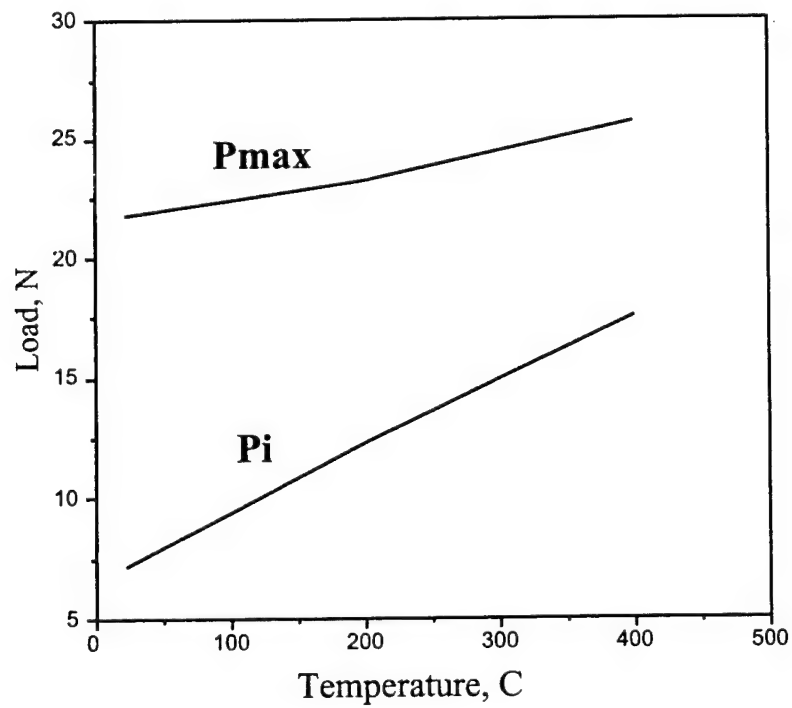


Figure 2.9: Variation of failure initiation load with temperature; $\tau^* = 400.0\text{MPa}$

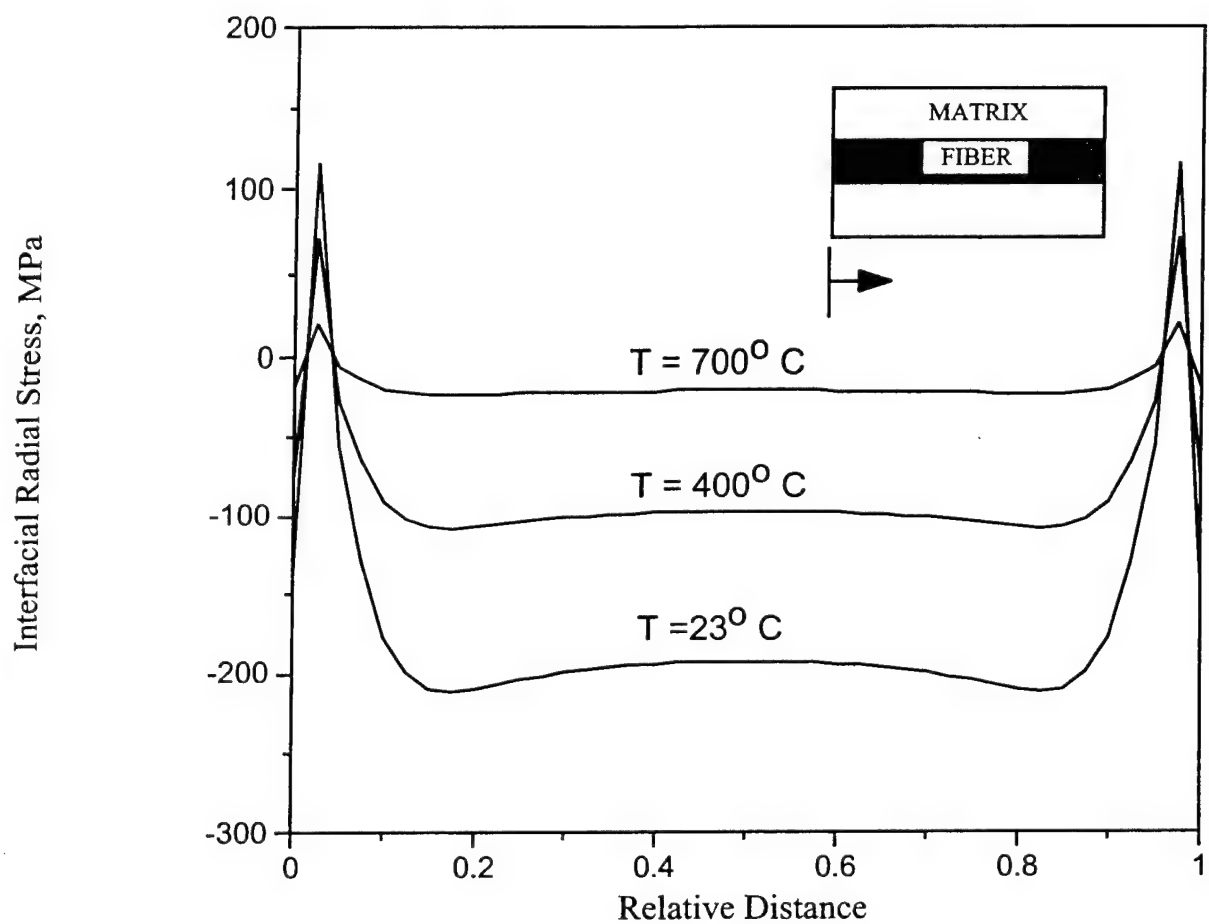


Figure 2.10: Variation of residual radial stresses along the interface with temperature

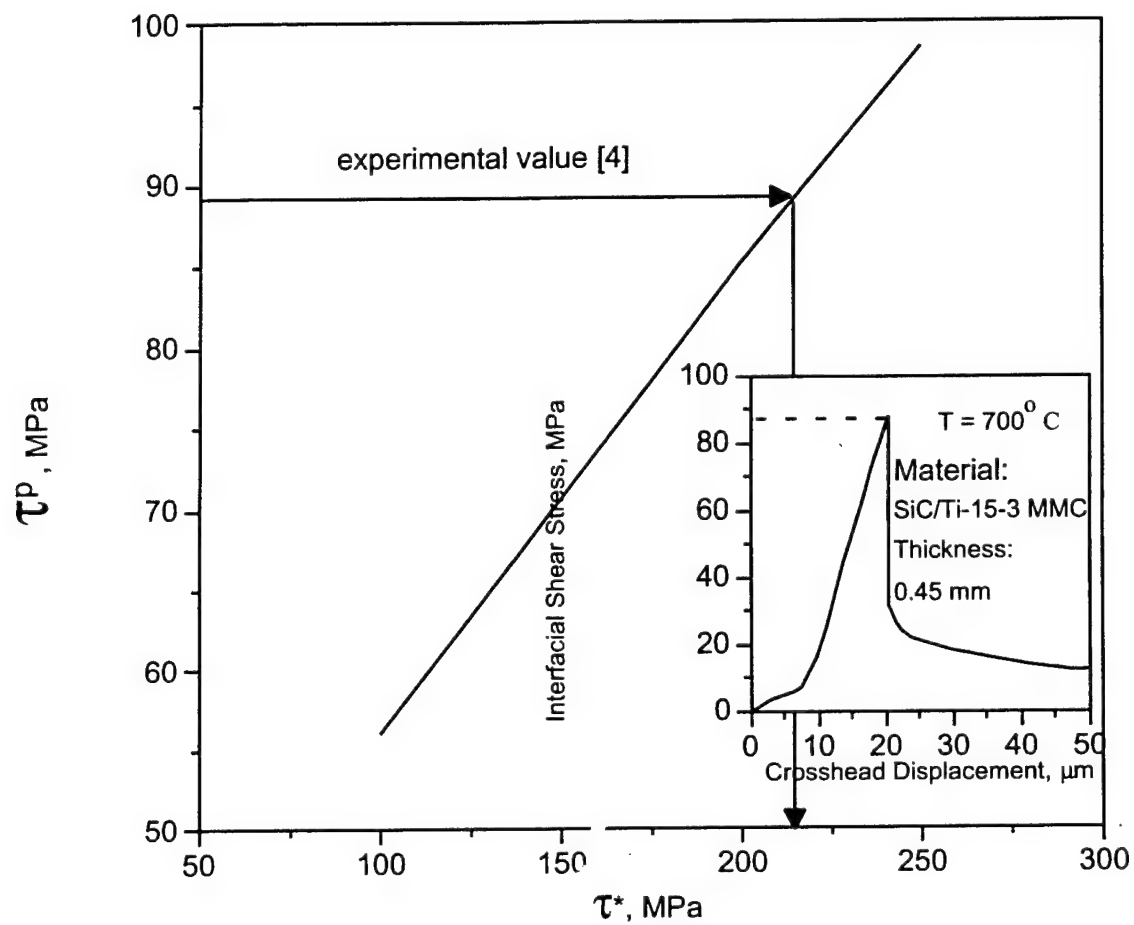


Figure 2.11: Calibration curve to obtain interfacial shear strength from experimental data;
 $T = 700^{\circ}\text{C}$

Chapter 3

Effect of Interface Chemistry on the Fracture Properties of Titanium Matrix Composites

3.1 Introduction

Metal matrix composites (MMC) are being considered as the material systems of choice for the jet engines of next generation aircraft, owing to their high specific stiffness and strength. In MMCs titanium matrices reinforced by silicon carbide fibers have shown considerable potential for high temperature aerospace applications. A critical issue to be addressed in the use of Titanium matrix composites is the high reactivity between the fiber and the matrix phases, which leads to the formation of a reaction zone at the fiber/matrix interface. The chemistry and geometry of this zone can influence fiber-matrix interfacial properties, and hence the overall thermomechanical response of these Titanium based MMCs.

SiC fibers are of considerable interest as reinforcements for metal and ceramic matrix composites because of their high strength and stiffness even at elevated temperatures. In MMCs a reaction layer often forms between the outermost regions of the fiber and the adjacent matrix. This reaction layer constitutes the interfacial region. The microstructure of the outer region of the fiber and the fiber/matrix interphase play a vital role in determining the properties of the composite. The microstructure of the SCS-6 fiber (developed by Textron Specialty Materials Inc.) has been reported in the literature [1]. The SCS-6 fiber consists of several layers deposited using CVD technique, as schematically shown in Figure 3.1. The fiber comprises of three broad regions namely a carbon core, many silicon carbide layers and an outer coating rich in carbon. The outer coating which is the region of interest, is a carbonaceous layer comprising carbon matrix with SiC particles embedded in it. This outer (carbon) coating itself is composed of three distinct layers (layers 1, 2 and 3) with varying size and density of SiC particles. Layer 2 is very thin compared to the other two and also has the lowest density of silicon carbide particles in it [1]. Push-out experiments on SCS-6/RBSN

CMCs [1] have shown that the failure initiation occurs predominantly in this region. Similar experiments by Roman and Jero [2] on as-processed SCS-6/Ti-6Al-4V MMC also revealed that the interface failure has occurred in the outer carbon coating and not in the reaction zone.

Titanium is highly reactive at elevated temperatures reacts with the carbon and silicon in the coating to form the reaction zone (Figure 3.2). These constituents (carbon, silicon and titanium) inevitable in the Titanium Matrix Composite systems ; hence, a clear understanding of the reaction between these elements at elevated temperatures and the effect of the reaction products on the mechanical properties is essential. Studies of reaction zone formation in TMCs have been carried out by several researchers [3, 4, 5]. None of these studies focus on establishing a relationship between the mechanical properties and the chemical composition of the interfacial region as the interface evolves. This is the objective of the current study. This type of study is critical in not only understanding the evolution of the interfacial reaction zone, but also in providing means to optimize the interface chemistry for performance.

Fiber Push-out Test has recently emerged as a popular test for characterizing the mechanical properties of the interface due mainly to simpler specimen preparation and equipment. This test has been used to measure the interfacial properties of MMCs at room [6, 1, 8] and elevated temperatures [9, 10]. Chandra and coworkers [3, 7, 5] analyzed the thin-slice push-out test and simulated the initiation of interface failure and its propagation using non-linear finite element methods. This work was able to explain many of the experimental observations [9] of push-out behavior at room and elevated temperatures. They also proposed a method for evaluating the interfacial shear strength [14] and fracture toughness [7] from the push-out data.

The present work involves elevated temperature exposure experiments on MMCs to study the effect of exposure temperature and time on the reaction zone, and the effect of evolution on mechanical properties. SCS-6/Timetal 21s (Ti-15Mo-3Al-2.7Nb-0.25Si) composite system is selected as the model material system and the relationship between reaction zone evolution and interface mechanical properties is investigated. Push-out tests in combination with the computational fracture mechanics approach developed by the authors [5, 7] are used to evaluate the fracture properties.

3.2 Evaluation of Interfacial Fracture Toughness of MMCs

In this paper, a numerical method based on the equivalent domain integral technique developed by the authors [5, 7] is used to simulate the fracture process during a thin slice push-out test and extract the interfacial fracture toughness G_{ic} of SCS-6/Timetal21s composites from the experimental data.

The thin-slice push out test involves pushing a fiber out of a composite specimen by the application of compressive load through a flat indenter. Modeling such a test involves three major stages. Step 1 involves modeling the composite consolidation at high temperatures and then cooling down to room temperature which induces residual stresses in the composite. Step 2 is the specimen preparation stage consisting of slicing a thin push-out specimen from the bulk composite which results in stress redistribution at the two ends of a fiber. Step 3 is modeling the loading stage where compressive load is applied to the fiber until it is pushed out of the specimen. A detailed description of the above sequence of steps is provided elsewhere [3]. The test is analyzed using an axisymmetric cylindrical model. A three phase model consisting of fiber, matrix and a composite phase with effective properties has been used. The interface is modeled as a contact surface and the bonding at the interface is simulated using high stiffness springs. The interface failure process is modeled using a strain energy based failure criteria given by:

$$G_i \geq G_{ic}$$

where G_i is the strain energy release rate for the interface crack and G_{ic} is the critical value of the strain energy release rate. The interface crack propagates further when its strain energy release rate exceeds the critical value. The strain energy release rate of the propagating interface crack is computed using the Equivalent Domain Integral (EDI) [8, 9, 4] method. The EDI method was implemented in the commercial finite element analysis software MARC [6] through user subroutines. A typical mesh used is shown in Figure 5.1. A small interface crack of the order of $0.5r_f$ (where r_f is the fiber radius) is introduced at both the ends of the specimen during step 2 of the simulation for the purpose of computation of energy release rates.

3.3 Results and Discussion

The effect of elevated temperature exposure on the interfacial fracture behavior of MMCs is studied by subjecting SCS-6/Timetal 21s specimens to selected temperatures (450° C, 700° C and 927° C) in vacuum for varying periods of time. The time periods used are 25, 70 and 120 hours. Most of the specimens for the exposure study were cut from a composite panel consolidated by Textron Specialty Materials, Inc. Some of the specimens were fabricated in-house using foil-fiber-foil technique. Scanning Electron Microscope (SEM) is used to measure the thickness of the interface. Interfacial chemistry is monitored using Energy Dispersive X-ray Spectroscopy (EDX). Push-out tests are conducted on the heat treated specimens and the results are compared with those of as-processed ones. Numerical simulations are used to extract interfacial fracture toughness values from the experimental data.

3.3.1 Change in Reaction Zone Size and Composition

The change in reaction zone thickness is measured as a function of time for two temperatures 927° C and 700° C and compared with the reaction zone size for as processed conditions.

The presence of a reaction zone is identified by the change in the morphology in the SEM micrographs (Figure 3.2). The coating size of unconsolidated fibers is measured and taken as the reference. The variation in the reaction zone and the coating thicknesses for specimens exposed to 927° C for 25, 70 and 120 hours were measured and plotted in Figure 3.4 along with the as-processed sample. It is seen from this figure that the initial growth of the reaction zone for the 25 hours case is by partial consumption of the coating and partial transformation of the matrix region. With extended exposure upto 120 hours the reaction zone growth occurs *more through transformation of the matrix than through consumption of the coating*. The exposure studies conducted at 700° C showed that the reaction zone growth with time and also the change in the thickness of the outer carbon coating are significantly reduced. An important observation from the exposure studies is that the coating is not fully consumed even after being subjected to high temperatures for extended periods of time.

Elemental composition and diffusion are studied with the help of EDX. Line scans are performed across the reaction zone, showing the variation in the chemical composition. The diffusion of alloying elements across the reaction zone is studied as a function of time for 927° C and 700° C. The results for the exposure study at 927° C for 120 hours only are discussed in detail in this study since the maximum change is observed in this case. Comparisons are made with the as-processed samples. Since EDX system used in this study is not capable of detecting lighter elements such as Carbon, the Carbon percentage is deduced from the relative counts as the rest of the chemical composition. The concentration of Titanium was found to be the maximum in the reaction zone, followed by silicon. The concentration of the other alloying elements such as Molybdenum, Aluminum and Niobium are observed to be minimal.

The variation of Titanium for the as-received specimen is shown in Figure 3.5. It is seen from this figure that Titanium content for half of the reaction zone is of the same order as that in the matrix. The Titanium content reduces sharply in the reaction zone near the coating. Figure 3.6 shows the line scan of Titanium from a sample which was exposed to 927° C for 120 hours. It can be seen that the diffusion of Titanium towards the carbon coating is more profound after the thermal exposure when compared to the as-processed composite specimen. Figure 3.7 shows the variation of silicon across the reaction zone. From this figure, it can be seen that the highest concentration of silicon occurs at the coating reaction zone interface. This silicon concentration decreases across the reaction zone thickness towards the matrix. The behavior of silicon after the thermal exposure is observed to be similar to that of the as-processed case as can be seen from Figure 3.8.

It can be inferred from the chemical composition studies that the carbon from the fiber coating probably diffuses the maximum into the matrix indicating Titanium Carbide to be the compound which is present in most of the interfacial region. This has also been confirmed by other researchers [3]. The results also suggest that Titanium Silicides (Ti_5Si_3) may be present mainly near the coating reaction zone interface. It has to be noted that TiC in the reaction zone is formed in two possible ways: by the diffusion and subsequent reaction of the free carbon (from the outer carbon coating) with the Titanium, and due to the direct reaction of Ti with SiC from the coating.

3.3.2 Evaluation of Interfacial Fracture Toughness from Thin-slice Push-out Tests

Fiber Push-out test was carried out on as-processed and heat treated specimens. The tests were carried out at NASA Lewis Research center. The average thickness of the as-processed specimens is about 0.53 mm. A typical load displacement curve for a push out test on as-processed specimen is shown in Figure 3.9. From this figure it is seen that after attaining the peak load there is a sharp load drop which corresponds to the fiber being completely debonded and the onset of frictional sliding. Full debonding is also characterized by a sharp acoustic signal also shown in the figure. The average peak load obtained for the as-processed specimens is of the order of 10 N which corresponds to an average peak debond shear stress of about 38 MPa. Figure 3.10 shows the push-out behavior after extended exposure at 927° C. It can be seen that the peak load in this has significantly increased. It is also observed from this figure that there is no distinct sharp load drop associated with complete debonding as is seen for the as-processed case. There is also no sharp acoustic signal which marks the event of complete debonding as observed in the earlier case. The push-out test results at 700° C and at 450° C are observed to be similar to that the as-processed case characterized by abrupt load drops after complete debonding accompanied by sharp acoustic signals.

A composite of the test results for the as-processed specimens and those subjected to 450°, 700° and 927° C for different exposure time periods is shown in Figure 3.11. Each point is the average of 12 push-out test results. The scatter in the data is also shown in the figure. As mentioned earlier the average peak debond shear stresses are significantly higher for the specimens subjected to 927° C heat treatments than those for the as-processed specimens and the specimens heat treated at 450° and 700° C. The results for the 927° C heat treated specimens also show a large degree of scatter. It can also be seen from this figure that the exposure time did not have a significant effect on the test results, especially at lower temperatures. The results for the tests conducted for the as received specimen and those subjected to the lower temperature ranges ($< 700^{\circ}$ C) suggest that there is not much change in interfacial properties at these temperatures. Thus the most significant change in interfacial behavior is observed for the specimens subjected to 927° C heat treatments.

The fracture mechanics based approach developed previously [5, 7] is used here to extract interfacial fracture toughness values from the push-out test results. Numerical simulations of push-out tests representing conditions of specimens, exposed to 927°, 700° C and 450° C for 120 hours and as-processed specimens are carried out. The fracture toughness values obtained from the numerical simulations are shown in Table 1. It is observed that the fracture toughness values for specimens heat treated at 700° C and 450° C are not very different from that of the as-processed specimen and are in the range of 55 to 60 J/m^2 . However when the specimens were exposed at 927° C, the mode II fracture toughness is observed to actually increase significantly to about 70 J/m^2 .

3.3.3 Observation of the Fracture Surface of Push-out Specimens

In order to obtain a better idea about the mechanics of the failure process the fracture surfaces of the failed push-out specimens were examined with the help of an SEM. It is observed that in all the cases, debonding initiated from the bottom of the push-out specimen, i.e., the side opposite to that of the point of application of the compressive load. This is consistent with theoretical predictions [3] and experiments carried out in other as-processed Titanium Matrix Composite systems where residual stresses are present [6, 8]. The bottom surface was examined for fracture characteristics as crack initiation takes place there. Typical fracture surfaces for 700° and 927° C are shown in Figures 3.12 and 3.13 respectively.

The fracture surfaces for the 700° C specimens reveal that cracks initiate in different regions of the coating, occurring more frequently in the middle and in the region near the coating reaction zone interface. The nature of the fracture surfaces at 700° C indicate a sharp abrupt fracture process thus consistent with the abrupt load drops seen in the load displacement curves and the sharp acoustic emission results. The element diffusion results and the negligible reaction growth at 700° C suggests that the middle region of the coating is the weak link in these specimens. The fracture surfaces for the as-processed specimens and those subjected to 450° C heat treatments are observed to be similar to that of the 700° C case.

The fracture surfaces of the 927° C heat treated specimens are significantly different from that of the 700° heat treated specimens. It is observed from scanning electron micrographs that debonding initiates more in the interface region than in the coating. The fracture surfaces are rough with the presence of large amount of debris. Cracks are seen to form in the middle of the reaction zone or near the reaction zone matrix interface. Comparison of the fracture surfaces of the push-out specimens exposed to different time periods did not reveal significant differences in the fracture behavior. The large reaction zone growth and the extensive diffusion of titanium into the coating indicates the possible formation of titanium carbides and silicides near the coating. Also since there is a considerable consumption of the coating, the weaker region (layer 2) in the coating is replaced by the strongly bonded high concentration titanium region. The fracture process in the 927° C specimens thus is characterized by a slow fragmentation of the reaction zone and high peak debond and sliding frictional stresses.

3.4 Summary and Conclusions

The evolution of interface in SCS-6/Timetal 21s composite system is studied by means of heat treatment experiments, with the objective of establishing a link between the evolution of chemistry and geometry of the reaction zone and the interfacial properties.

- Microstructural studies reveal that reaction growth is due to transformation of both coating and the matrix. The growth of the reaction zone into the matrix is much more

than the growth towards the fiber, as carbon is able to diffuse much farther into the matrix than the diffusion of Titanium into the fiber.

- Reaction zone sizes increase rapidly with time at 927° C. At lower temperatures such as 700° C and 450° C no significant increase in reaction zone size is observed for this system.
- Push-out tests conducted on heat treated specimens reveal that the effect of thermal exposure on interfacial properties is predominantly due to exposure temperature. Time of exposure is found to have only a secondary effect.
- Fracture toughness values remain more or less constant for normal use temperatures in the range of 450° to 700° C. The values however, increase when the exposure temperature is raised to 927° C.
- Fracture surfaces of the specimens exposed at 927° C show that debonding took place in the reaction zone whereas in as-processed specimens and those heat treated at the lower temperature ranges debonding initiated in the coating. This is because the weak region in the coating is replaced by the stronger interfacial region.

Bibliography

- [1] X.J. Ning and P. Pirouz. The Microstructure of SCS-6 SiC Fiber. *Journal of Materials Research*, 6(10):2234-2248, 1991.
- [2] I. Roman and P. D. Jero. Interfacial Shear Behavior of Two Titanium-Based SCS-6 Model Composites. In D. B. Miracle, D. L. Anton, and J. A. Graves, editors, *Intermetallic Matrix Composites II, MRS Symposium Proceedings*, volume 273, pages 337-342. Materials Research Society, 1992.
- [3] E. L. Hall and A. M. Ritter. Structure and Behavior of Metal/Ceramic Interfaces in Ti alloy/SiC Metal Matrix Composites. *Journal of Materials Research*, 8(5):1158-1168, 1993.
- [4] J-M. Yang and S. M. Jeng. Interfacial Reactions in Titanium Matrix Composites. *Journal of Metals*, 41(11):56-59, 1989.
- [5] W. O. Soboyejo. Investigation of the Effects of Matrix Microstructure and Interfacial Properties on the Fatigue and Fracture Behavior of a Ti-15V-3Cr-3Al-3Sn/SCS9 Composite. *Materials Science and Engineering*, A183:49-58, 1994.
- [6] L. J. Ghossein, J. I. Eldridge, and P. Kantzos. Analytical Modeling of the Interfacial Stress State During Pushout Testing of SCS-6/Ti-Based Composites. *Acta Metallurgica et Materialia*, 42(11):3895-3908, 1994.
- [7] B. S. Majumdar and G. M. Newaz. Inelastic Deformation of Metal Matrix Composites: Plasticity and Damage Mechanisms. *Philosophical Magazine A*, 66(2):187-212, 1992.
- [8] B. S. Majumdar and D. B. Miracle. Interface Measurements and Applications in Fiber Reinforced MMCs. *Journal of Key Engineering Materials - Special issue on Interfaces in Composites and Laminated Structures*, 116-117:153-172, 1996.
- [9] J. I. Eldridge. Fiber Push-out Testing of Intermetallic Matrix Composites at Elevated Temperatures. In D. B. Miracle, D. L. Anton, and J. A. Graves, editors, *Intermetallic Matrix Composites II, MRS Symposium Proceedings*, volume 273, pages 325-330. Materials Research Society, 1992.
- [10] J. I. Eldridge and B. T. Ebihara. Fiber Push-out testing Apparatus for Elevated Temperatures. *Journal of Materials Research*, 9(4):1035-1042, 1994.

- [11] C. R. Ananth and N. Chandra. Numerical Modeling of Fiber Push-out Test in Metallic and Intermetallic Matrix Composites - Mechanics of the Failure Process. *Journal of Composite Materials*, 29(11):1488-1514, 1995.
- [12] N. Chandra and C. R. Ananth. Analysis of Interfacial Behavior in MMCs and IMCs using Thin-slice Push-out Tests. *Composites Science and Technology*, 54(1):87-100, 1995.
- [13] S. Mukherjee, C. R. Ananth, and N. Chandra. Effect of Residual Stresses on the Interfacial Fracture Behavior of MMCs. *Composites Science and Technology*, (in print) 1997.
- [14] C. R. Ananth and N. Chandra. Evaluation of Interfacial Shear Properties of Metal Matrix Composites from Fiber Push-out Tests. *Mechanics of Composite Materials and Structures*, 2:309-328, 1995.
- [15] S. Mukherjee, C. R. Ananth, and N. Chandra. Evaluation of Fracture Toughness of MMC Interfaces Using Thin-slice Push-out Tests. *Scripta Materialia*, 36(11), 1997.
- [16] G. P. Nikishkov and S. N. Atluri. An Equivalent Domain Integral Method for Computing Crack Tip Integral Parameters in Non-Elastic, Thermomechanical Fracture. *Engineering Fracture Mechanics*, 26:851-867, 1987.
- [17] G. P. Nikishkov and S. N. Atluri. Calculation of Fracture Mechanics Parameters for an Arbitrary Three-Dimensional Crack, by the Equivalent Domain Integral Method. *International Journal for Numerical Methods in Engineering*, 24:1801-1821, 1987.
- [18] I. S. Raju and K. N. Shivakumar. An Equivalent Domain Integral Method in the Two-Dimensional Analysis of Mixed Mode Crack Problems. *Engineering Fracture Mechanics*, 37(4):707-725, 1990.
- [19] MARC Analysis Corporation. *MARC Version: K6, User Manuals*, 1995.

Material System: SCS-6/Timetal 21s fiber volume fraction= 0.35 average specimen thickness=0.53 mm	Peak Load (Experimental) (N)	G_{ic} (Simulation) (J/m²)
As-processed	10.12	53.5
Heat treated at 450°C for 25 hours	12.01	55.0
Heat treated at 700°C for 120 hours	16.37	58.0
Heat treated at 927°C for 120 hours	29.28	70.0

Table 3.1: Interfacial fracture toughness

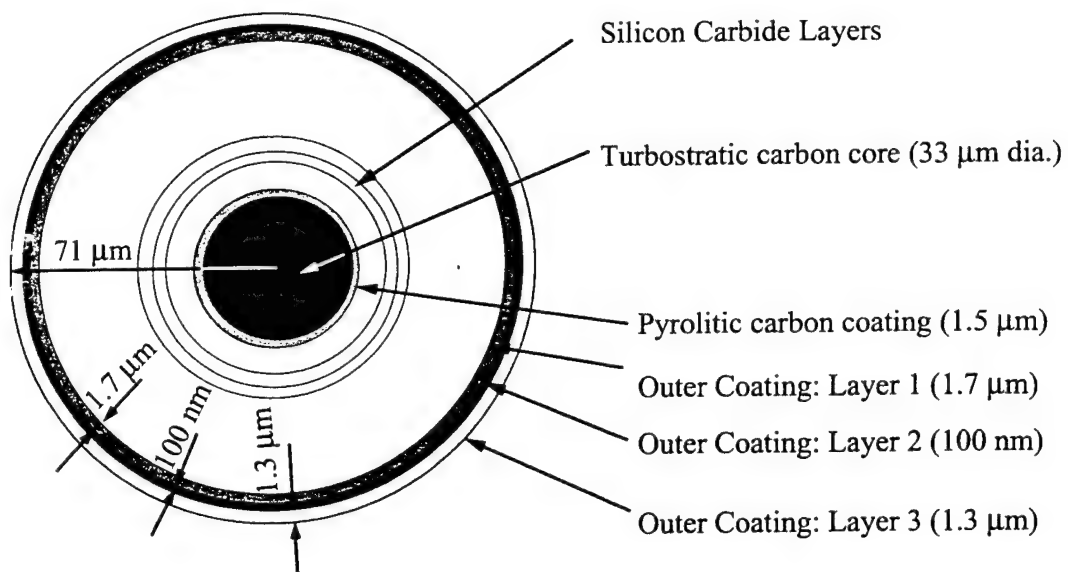


Figure 3.1: Architecture of the SCS-6 SiC Fiber [102]

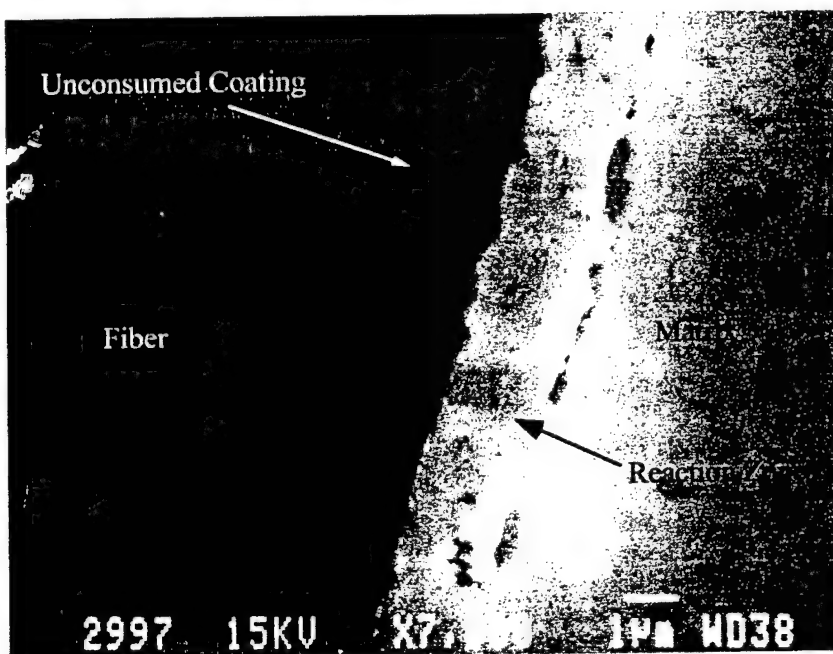


Figure 3.2: Interfacial region in a SCS-6/Timetal 21s composite

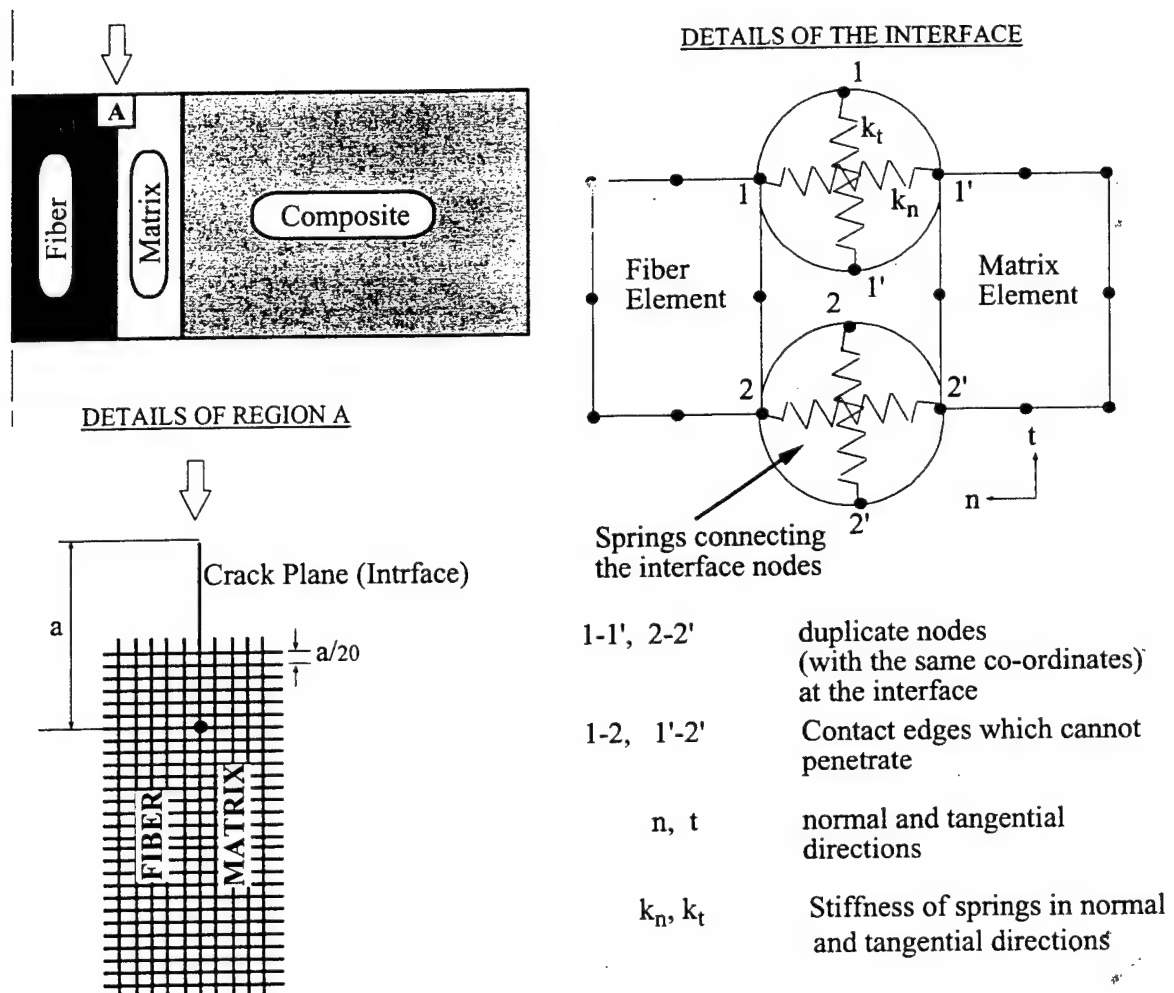


Figure 3.3: Finite element model and details of the interface

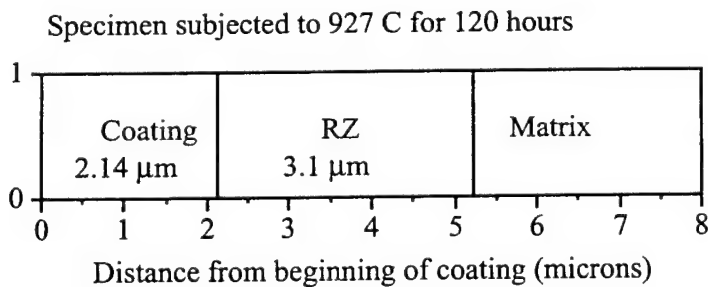
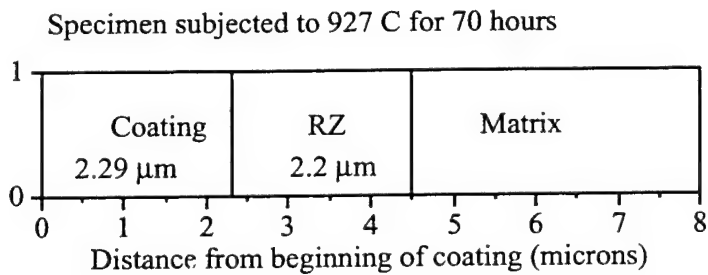
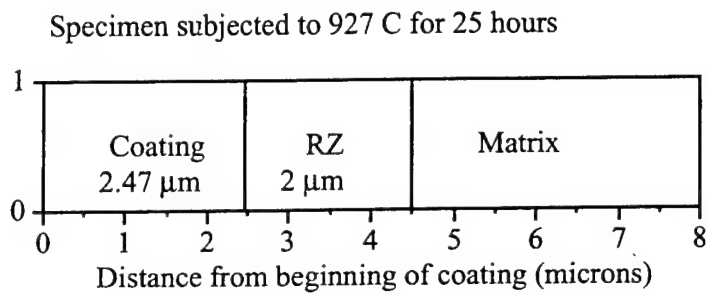
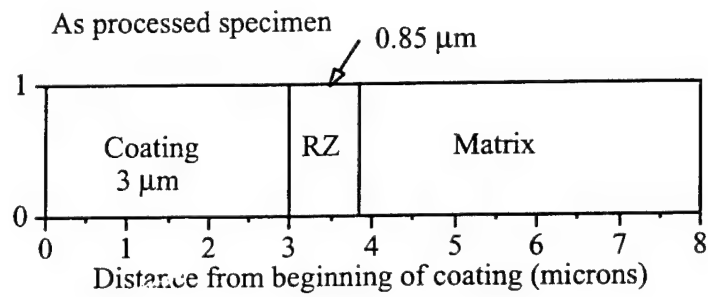


Figure 3.4: Variation in reaction zone size with exposure time for SCS-6/Timetal 21s composite heat treated at 927° C

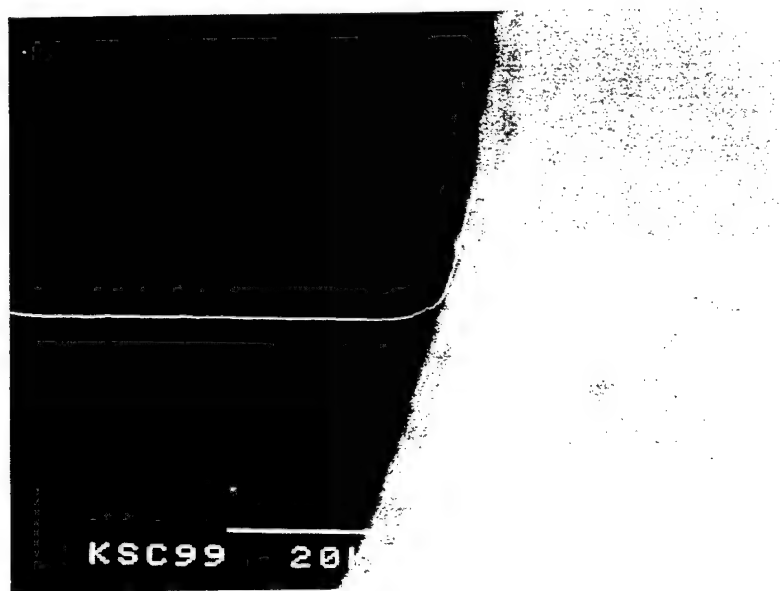


Figure 3.5: Titanium x-ray scan of an as-processed SCS-6/Timetal 21s specimen (a) line scan (b) dot map



Figure 3.6: Titanium x-ray scan of a SCS-6/Timetal 21s specimen exposed to 927° C for 120 hours (a) line scan (b) dot map

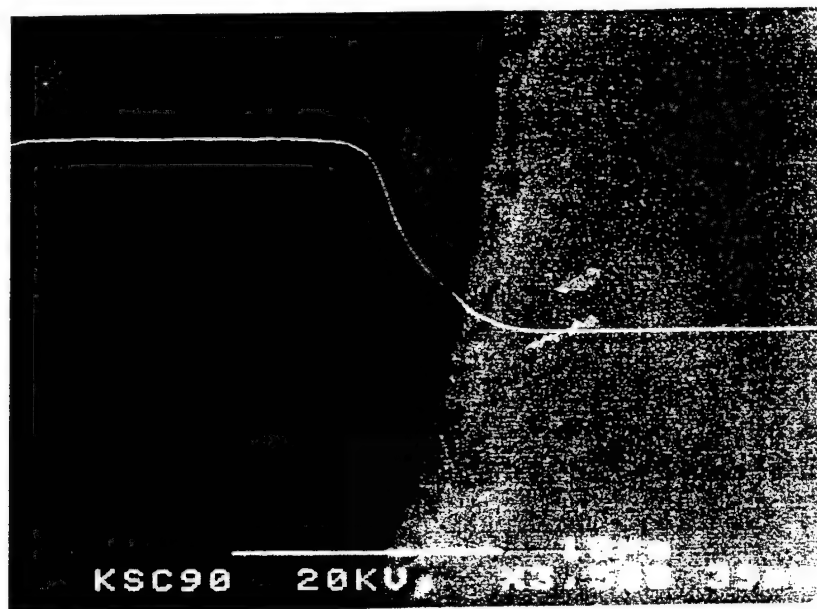


Figure 3.7: Silicon x-ray scan of an as-processed SCS-6/Timetal 21s specimen (a) line scan (b) dot map.

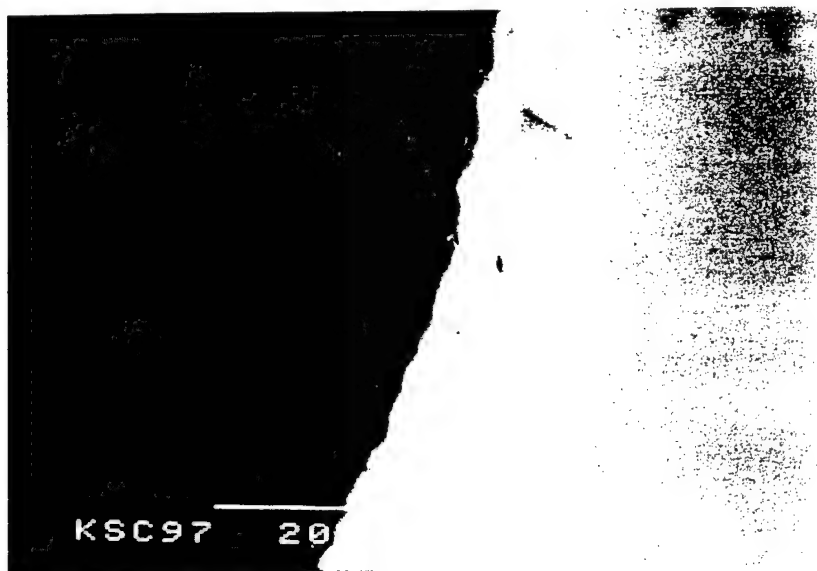


Figure 3.8: Silicon x-ray scan of a SCS-6/Timetal 21s specimen exposed to 927° C for 120 hours (a) line scan (b) dot map

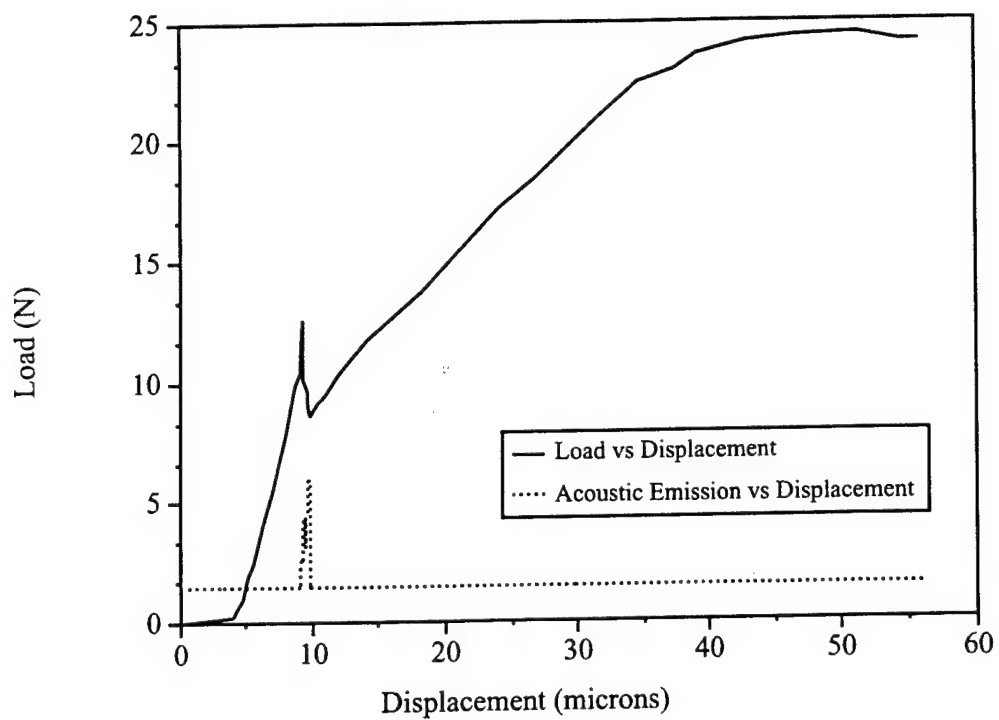


Figure 3.9: Typical load displacement curve for a push-out test conducted on an as-processed specimen

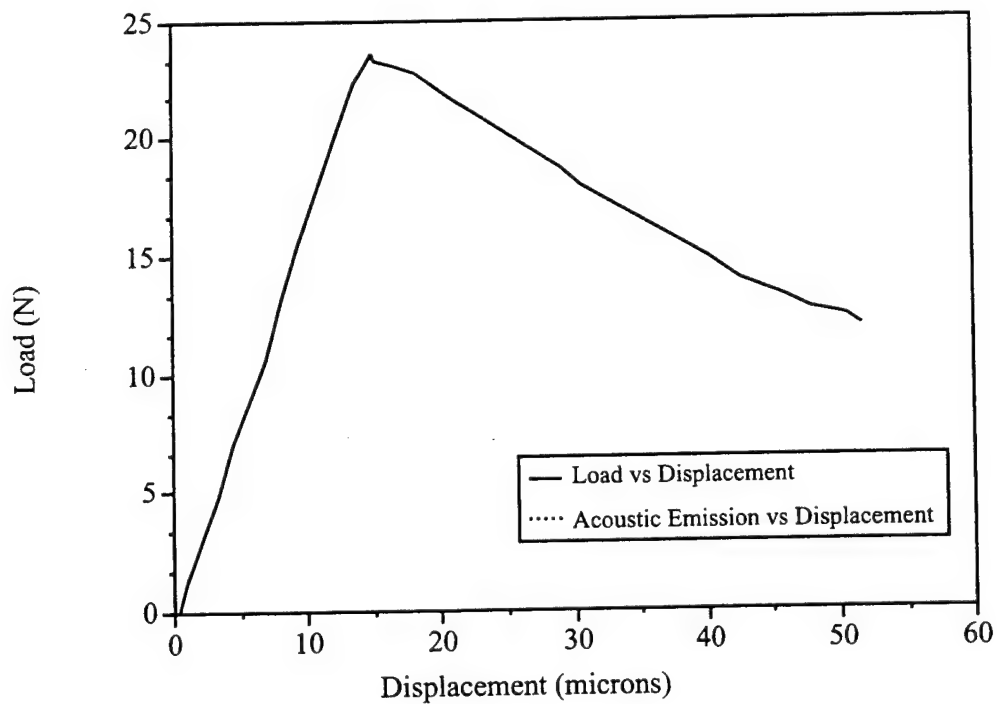


Figure 3.10: Typical load displacement curve for a push-out test conducted on a specimen subjected to 927^o C for 25 hours

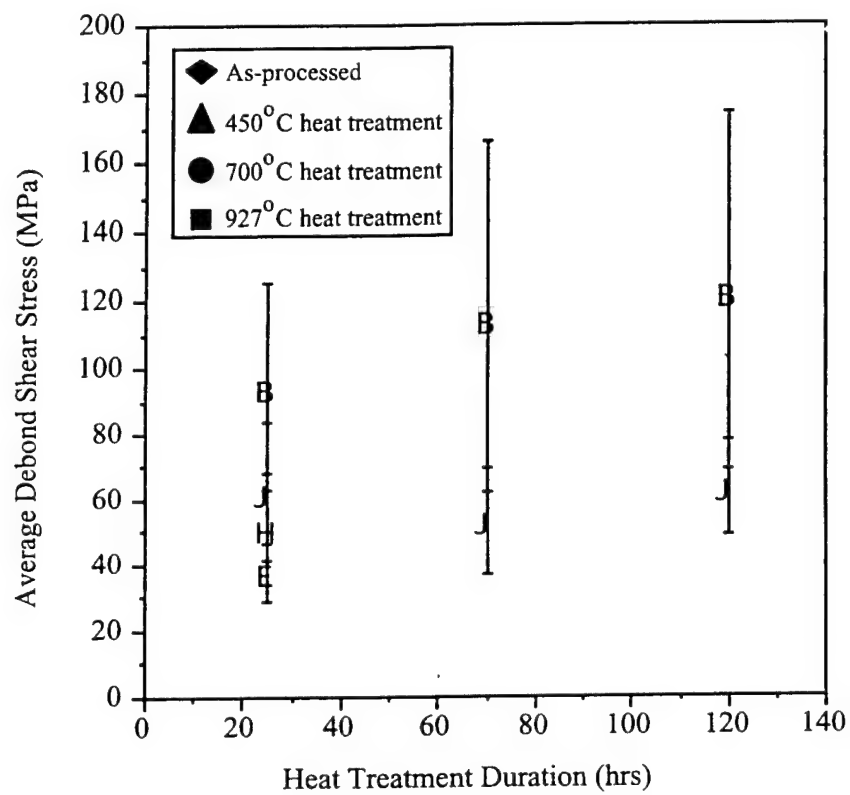


Figure 3.11: Composite of the push-out test results

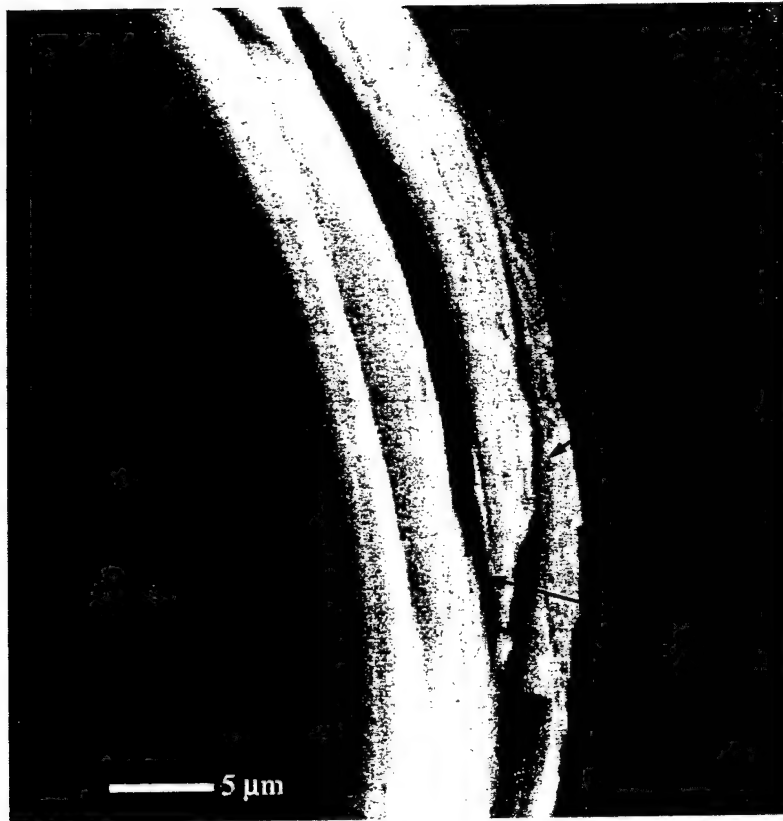


Figure 3.12: Bottom fracture surface for a 700° C heat treated push-out specimen

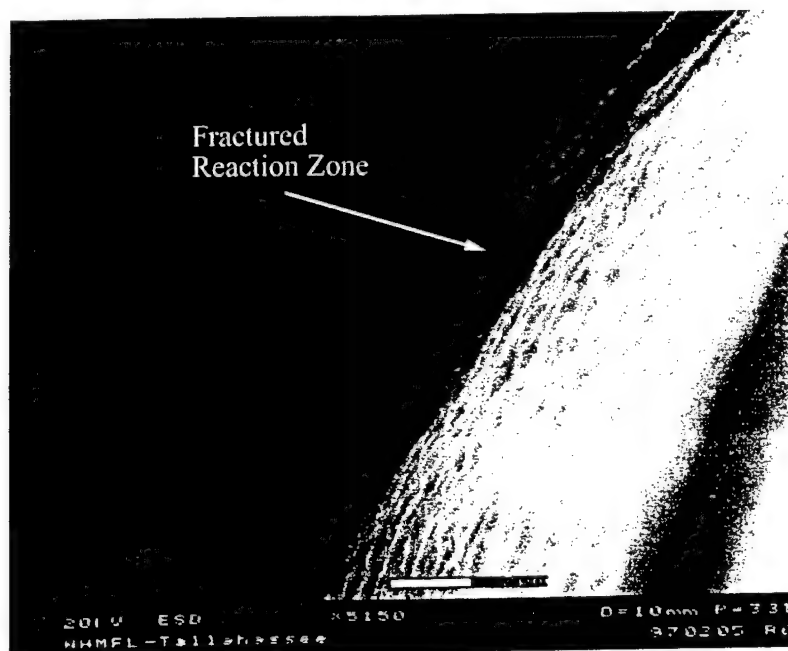


Figure 3.13: Bottom fracture surface for a 927° C heat treated push-out specimen

Chapter 4

Effect of Residual Stresses on the Interfacial Fracture Behavior of MMCs

4.1 Introduction

Metal matrix composites (MMC) are being considered as potential material systems of choice for the advanced propulsion systems of twenty-first century aircraft, owing to their high specific stiffness and strength. One of the critical issues in the successful application of these composites is the behavior of the fibre-matrix interface. The role of interface is critical to the performance of the composites. The strength, stiffness and fracture behavior of the composites depend on the interfacial conditions. In MMCs experimental investigations¹⁻³ give clear evidence of premature interfacial debonding, emphasizing the need to study the interfacial behavior of this class of composites. The push-out test is emerging as an important experimental tool for characterizing the interface behavior of MMCs mainly after its widespread use in the study of interfaces in ceramic matrix composites (CMC). The presence of high levels of residual stresses in MMCs alters the mechanics of the interfacial failure process, making the interpretation of test results difficult. Moreover the relatively high bond strength of MMCs and residual clamping stresses at the interface limit the specimen thickness for push-out tests. The experiments under these conditions indicate⁴ that interface failure initiates from the bottom of the specimen and not from the loading end as in the case of CMCs. The cause of bottom initiation during thin slice push-out tests of MMCs has been dealt in detail^{5,6} and is found to be predominantly due to residual stresses. This is different from two way debonding reported in the analyses of fiber pull-out tests^{7,8} on polymer and ceramic matrix composites, where fiber volume fraction and Young's modulus ratio are the dominant factors.

In recent years there have been several efforts to model the push-out test analytically with the objective of understanding the interfacial behavior⁹⁻¹⁵. The most comprehensive study

thus far which is applicable for MMCs is by Liang and Hutchinson¹⁶; but this work still does not address the case of failure initiation from the bottom surface. Chandra et al^{5,6,17} analyzed the thin-slice push-out test where the initiation of interface failure and its propagation were simulated using non-linear finite element methods. This work was able to explain many of the experimental observations¹⁸ of push-out behavior at room and elevated temperatures. The failure criteria used in their approach is based on local stresses and hence is affected by stress concentration effects which are a function of mesh density in the finite element analysis. This error was minimized to a certain extent by adopting proper averaging schemes near the crack tip. A more consistent quantity for monitoring the fracture process is the strain energy release rate (G_i) of the interface crack. G_{ic} , the critical value of G_i is a measure of the fracture toughness of the interface.

In this paper, a numerical method based on the equivalent domain integral technique has been developed to compute the strain energy release rates G_i of the interfaces in composites. This method has been applied to evaluate the G_i of as-processed titanium based MMCs and compared with some CMC systems. The interface failure process in a thin slice push-out test is simulated using the developed methodology. It is shown that processing induced residual stresses significantly affect the initiation and propagation of interface cracks in MMCs.

4.2 Evaluation of Energy Release Rates

Several methods are available to calculate the energy release rate G for an existing crack such as virtual crack closure technique (VCCT), contour integral and the equivalent domain integral method (EDI). The contour integral method is relatively independent of mesh density, however it requires a focussed mesh i.e., a ring of singular elements around the crack tip. This hampers crack propagation studies. The EDI method does not require the use of singular elements for computing energy release rates and is ideally suited for studying the propagation of cracks. J-integral is a closed contour integral of the strain energy density and the work done by tractions around the crack tip. It is a path-independent parameter and is equivalent to the rate of change of total potential energy with reference to the crack length. For the purposes of numerical implementation the J-integrals are converted to equivalent area or domain integrals¹⁹⁻²¹, hence the name equivalent domain integral (EDI). The conversion of line integrals to domain integrals is very advantageous because all the quantities necessary for computation of the domain integrals are readily available in a finite element analysis. The EDI method has been shown²¹ to give accurate results for the J-integral for mode I, mode II and mixed mode problems. For an arbitrary closed contour Γ around the crack tip (Figure 4.1), the J-integral is defined in the absence of any body forces as:

$$J_{x_k} = \int_{\Gamma} \left[W n_k - \sigma_{ij} \frac{\partial u_i}{\partial x_k} n_j \right] d\Gamma \quad (4.1)$$

where $k=1,2$ and W is the total strain energy density defined as:

$$W = \int_0^{\epsilon_{ij}} \sigma_{ij} d\epsilon_{ij} \quad (4.2)$$

The integrals J_{x_1} and J_{x_2} are two path-independent integrals that compute the total amount of the energy flux leaving the contour Γ in the two directions x_1 and x_2 respectively. J_{x_1} is known as the J-integral. J_{x_2} is called the product integral. A closed contour integral along DEFCBAD (Figure 4.1) can be defined by adding and subtracting the line integrals on the crack faces FC and AD and can be written as:

$$J_{x_k} = - \int_{DEFCBAD} Q S d\Gamma + \int_{FC} Q S d\Gamma + \int_{AD} Q S d\Gamma + \int_{CO} Q d\Gamma + \int_{OA} Q d\Gamma \quad (4.3)$$

or

$$J_{x_k} = - \int_{DEFCBAD} Q S d\Gamma + (J_{x_k})_{line} \quad (4.4)$$

where

$$Q = \left[W n_k - \sigma_{ij} \frac{\partial u_i}{\partial x_k} n_j \right] \quad (4.5)$$

For implementation in a finite element code the above contour integral on DEFCBAD for J can be converted into a domain or area integral as:

$$(J_{x_k})_{domain} = - \int_A \left[W \frac{\partial S}{\partial x_k} - \sigma_{ij} \frac{\partial u_i}{\partial x_k} \frac{\partial S}{\partial x_j} \right] dA - \int_A \left[\frac{\partial W}{\partial x_k} - \sigma_{ij} \frac{\partial \epsilon_{ij}}{\partial x_k} \right] S dA \quad (4.6)$$

Hence the total integral J_{x_k} can be written as

$$J_{x_k} = (J_{x_k})_{domain} + (J_{x_k})_{line} \quad (4.7)$$

$S = S(x_1, x_2)$ is an arbitrary but continuous function and has a value of 0 on the outer contour and a value of 1 on the inner contour. In order to be able to separate the individual modes (J_I and J_{II}) from the domain integral, a procedure called the decomposition method²¹⁻²³ was adopted in which the stress and displacement fields are separated into symmetric and anti-symmetric parts. Consider two points $P(x_1, x_2)$ and $P'(x_1, -x_2)$ that are in the immediate neighbourhood of the crack tip and are symmetric about the crack line. Then the symmetric and anti-symmetric parts of the displacements can be expressed in terms of the displacements at points P and P' as

$$\begin{Bmatrix} u_1 \\ u_2 \end{Bmatrix}_S = \frac{1}{2} \begin{Bmatrix} u_{1P} + u_{1P'} \\ u_{2P} - u_{2P'} \end{Bmatrix} \quad (4.8)$$

$$\begin{Bmatrix} u_1 \\ u_2 \end{Bmatrix}_{AS} = \frac{1}{2} \begin{Bmatrix} u_{1P} - u_{1P'} \\ u_{2P} + u_{2P'} \end{Bmatrix} \quad (4.9)$$

Similarly, the symmetric and anti-symmetric components of the stresses can be expressed in terms of the stresses at points P and P' as

$$\begin{pmatrix} \sigma_{11} \\ \sigma_{22} \\ \sigma_{33} \\ \sigma_{12} \end{pmatrix}_S = \frac{1}{2} \begin{pmatrix} \sigma_{11P} + \sigma_{11P'} \\ \sigma_{22P} + \sigma_{22P'} \\ \sigma_{33P} + \sigma_{33P'} \\ \sigma_{12P} - \sigma_{12P'} \end{pmatrix} \quad (4.10)$$

$$\begin{pmatrix} \sigma_{11} \\ \sigma_{22} \\ \sigma_{33} \\ \sigma_{12} \end{pmatrix}_{AS} = \frac{1}{2} \begin{pmatrix} \sigma_{11P} - \sigma_{11P'} \\ \sigma_{22P} - \sigma_{22P'} \\ \sigma_{33P} - \sigma_{33P'} \\ \sigma_{12P} + \sigma_{12P'} \end{pmatrix} \quad (4.11)$$

These symmetric and anti-symmetric displacements and stresses can be used to evaluate the four integrals J_{Sx_1} , J_{Sx_2} , J_{ASx_1} , J_{ASx_2} using eqn.(7). The integrals J_{Sx_2} and J_{ASx_2} (domain and line components individually) will be identically zero because of the symmetric and anti-symmetric nature of the stress and displacement fields. The individual modes J_I and J_{II} can then be written as

$$\begin{aligned} J_I &= J_{Sx_1} \\ J_{II} &= J_{ASx_1} \\ J_{total} &= J_{Sx_1} + J_{ASx_1} \end{aligned} \quad (4.12)$$

The line integrals J_{Sx_k} and J_{ASx_k} using the symmetric and antisymmetric components of stresses and displacements can be written as

$$\begin{aligned} (J_{Sx_1})_{line} &= 2 \int_F^C \sigma_{22} \frac{\partial u_2}{\partial x_1} S dx_1 + 2 \int_C^O \sigma_{22} \frac{\partial u_2}{\partial x_1} dx_1 \\ (J_{Sx_2})_{line} &= 0 \\ (J_{ASx_1})_{line} &= 2 \int_F^C \sigma_{12} \frac{\partial u_1}{\partial x_1} S dx_1 + 2 \int_C^O \sigma_{12} \frac{\partial u_1}{\partial x_1} dx_1 \\ (J_{ASx_2})_{line} &= 0 \end{aligned} \quad (4.13)$$

As mentioned earlier $(J_{Sx_1})_{line}$ and $(J_{ASx_2})_{line}$ vanish due the symmetric and anti-symmetric nature of the stress and displacement fields. $(J_{Sx_1})_{line}$ and $(J_{ASx_1})_{line}$ are non-zero only in the presence of crack face tractions. Simplified expressions for the above line integrals are available in Ref. 21. The total J-integral J_{x_1} can be expressed as

$$J_{x_1} = (J_{Sx_1})_{domain} + (J_{Sx_1})_{line} + (J_{ASx_1})_{domain} + (J_{ASx_1})_{line} \quad (4.14)$$

The formulation described above is implemented through user subroutines in the finite element code MARC²⁴. The program computations were validated with typical problems including ones with cracks along bimaterial interfaces subjected to remote and crack face normal and shear tractions. Many of the results were also checked with those in the literature²¹.

About 5 paths were used to check for path independency. A typical path used is shown in Figure 4.2. The maximum variation of the total J-integral (eqn. 14) was found to be less than 0.5% between first (innermost) and the last (outermost) paths for all the cases. Since the decomposition method allows separation of individual modes, mode I and II contributions were also examined. It was found that the individual modes were *path dependent* (variation of 4% between first and last paths) even though the total integral was *path-independent*. This is consistent with observations in Ref. 21. The individual modes even though being path dependent can still provide rough estimates of the mode I and II contributions.

4.3 Numerical Modeling of the Interface Using Finite Element Methods

The fiber-matrix interface is modeled using a contact-friction formulation and the bonding at the interface is simulated with high stiffness *springs*⁵. The fiber and the matrix phases are modeled using quadrilateral elements. Duplicate nodes are created at the interface on fiber and matrix sides. The fiber-matrix bonding is achieved by connecting these duplicate nodes by means of springs with a stiffness greater than the elastic modulus of the fiber by a factor of 100. The mutual penetration of the matrix and the fiber elements is avoided by defining the fiber and matrix phases as deformable contact surfaces. A typical finite element discretization used along with details of the interface element are shown in Figure 4.3. Refinement was carried out until the variations in displacement fields between successive refinements were less than 0.01%. The presence of a small pre-existing crack is essential for the computation of energy release rates using the EDI method. Thus an interface crack of size less than $0.5 r_f$ (where r_f is the fiber radius) is assumed to be present at each end of the push-out specimen. Numerical investigations have shown that the presence of cracks of this magnitude does not affect G_i or the peak load. The element size around the crack front was $a/20$, where a is the length of the pre-existing crack. The regions used for computing the J-integral have a mesh which is symmetric about the crack plane. This is a requirement for the decomposition method. The stresses at the interface at each increment are monitored in the user subroutine. Initially a relative motion flag is set to 0. When the interface failure criterion is satisfied then the flag is changed to 1 and the stiffness of the springs is dropped to zero, indicating the onset of frictional sliding. Coulomb's law is used to model the frictional behavior.

An important consideration when computing energy release rates in the presence of Coulomb type of sliding friction is the path independency of the J-integral. Deng^{25,26} using an asymptotic approach reported that the strength of the crack tip field singularity will be weaker than $r^{-1/2}$ for a moving interface crack with frictional surface contact, as a result of which the conventional strain energy release rate G will be zero at the crack tip. This is a however a mathematical phenomenon. According to Deng^{25,27} G will have finite values away from the crack tip. The variation of G with distance from the crack tip was studied in a push-out test simulation after substantial debonding had occurred. For the push-out problem with

the geometry as described previously and with the coefficient of friction used, even with a very fine mesh near the crack tip, we could not numerically observe any appreciable decrease in G , save the numerical error (less than 0.5%) which was present even in the validation studies. A possible explanation for the failure to observe the decrease in G may be due to the fact that in the case of thin-slice push-out test where the cracks initiate at the support end, frictional effects are not found to be appreciable. This is mainly due to the relaxation of residual stresses in the debonded region and the absence of additional radial compressive stresses caused by Poisson's expansion of the fiber (as in the case of loading end crack initiation in CMCs). According to Deng^{25,27} a strain energy release rate type of fracture criterion and any contour around the crack tip can be used to represent G values as long as one is consistent with the path distance from the crack tip. In this paper an integral path with radius $r_c = 0.075r_f$ is consistently used in all the cases. In the case of bimaterial interfaces with Coulomb friction since the classical strain energy release rate vanishes at the crack tip the evaluated value of the J-integral cannot be interpreted as an intrinsic fracture energy quantity in precise terms. However, this value can be used for comparison purposes between different composite systems. In all the cases studied here (except section 4.3) the crack length is extremely small and the crack is stationary. Negligible sliding and friction occurs near the crack tip; hence the J-integral values computed for these cases was path independent. The line integral contributions are found to be insignificant for these cases and the value of the J-integral is from the domain integral contributions.

Elastic constitutive behavior is assumed for the fiber phase. Matrix is assumed to be a rate independent elastic-plastic material. The region in the vicinity of the interface crack is assumed to be elastic as experimental observations²⁸ have shown that crack tip plasticity is not present for interface cracks in the metal and ceramic matrix composite systems considered in this study. The temperature dependency of the elastic and inelastic properties^{1,29-32} of the constituent phases are included in the analysis. The material properties used in this study are given in Figure 4.4 and Table 1.

4.3.1 Simulation of the Single Fiber Push-out test

The single fiber push-out test is analyzed using an axisymmetric cylindrical model. A three phase model consisting of fiber, matrix and a composite phase with homogenized properties has been used. The push-out test is modeled following a sequence of steps described in detail elsewhere⁵. The appropriate boundary conditions for the steps are shown in Figure 4.5. Residual thermal stresses are induced during the composite consolidation process due to the CTE mismatch between the fiber and the matrix. A brief outline of the steps involved is given below:

1. Cooling of the bulk composite from the reference or stress free temperature.
2. Preparing the push-out specimen by cutting a thin slice from the bulk composite. This process results in shear stresses at the interface due to differential axial residual strains between the fiber and matrix.

3. The push-out load is applied by prescribing incremental displacements to the top face of the fiber.

The state of residual stress at the interface can be modified by pre-straining the composite to levels sufficiently high so as to introduce plastic strains in the matrix. In this case an additional step is introduced in between 1 and 2 with the same boundary conditions as that of step 1. The composite is strained in the longitudinal (or fiber) direction by prescribing displacements to the top face of the composite.

4.4 Results and Discussion:

The push-out test is simulated following the sequence of steps listed in the previous section. SCS-6/Ti-15-3, SCS-6/Ti-6-4 and SCS-6/Timetal-21S are the typical MMC systems considered in this study. The thickness of the push-out specimens in all the cases is taken to be 0.5 mm and the fibre volume fraction was chosen to be 35%. Both mode I and mode II energy release rates are measured for the push out problem. Preliminary studies of the push-out problem showed that the mode II energy release rate contribution to the total J-integral was 10^4 times that of mode I. Thus the mode I contribution is negligible and the problem of interface debonding due to push-out load can be treated essentially as a mode II problem.

4.4.1 G_i after Specimen Slicing

As mentioned earlier the specimen preparation stage which is modeled as per step 2 in the simulation sequence, results in the redistribution of the residual stresses near the composite ends. This causes stress concentration at the pre-existing cracks at both the ends of the specimen. The calculations of G_{ir} (the value of G_i after slicing and before the application of indenter load) from the EDI method for different material systems are shown in Table 2. These are values obtained from the total J-integral. It can be seen that G_{ir} of the order of 40 J/m^2 are present at the specimen ends. The variation of interfacial shear stress along the specimen thickness (Figure 4.6) indicates that the stress state at both ends of the specimen is symmetric in nature and so are the other components of stress. This leads to symmetric values for the energy release rates at both the ends of the specimen. This also indicates the tendency of the fiber to protrude out of the matrix at either end. G_{ic} , which is the critical value required for debonding is taken to be higher than G_{ir} in these simulations, as microscopic studies of MMC specimens do not reveal significant interfacial debonding before the application of the mechanical load. Hence the values of G_{ir} listed in Table 2 serve as a lower bound for G_{ic} of these MMC systems. To illustrate this, step 2 is simulated by assuming G_{ic} value to be lower than 40 J/m^2 in the case of SCS-6/Ti-15-3 composite. In this case debonding occurs after the end of the processing stage (even before application of load by the punch) and proceeds with unstable crack propagation from either end for

most of the specimen thickness. It should however be pointed out that surface roughness in interfaces may play a role in arresting this unstable crack propagation.

The processing simulations are also performed on some CMCs like SCS-6/CAS I and SCS-6/Borosilicate to compare energy release rate values with those obtained for the MMCs. These energy values are also listed in Table 2. As expected the G_{ir} values for the CMCs were at least one order less than those for the MMCs. This is to be expected since the residual stresses generated in the CMCs are much smaller compared to that in MMCs. To examine the contribution to the energy release rates from residual stresses, numerical simulations were performed in which the MMC specimens after processing were plastically strained before slicing. The results for 0.5% and 1.3% total strain are shown in Table 2. The effect of inducing plastic strain in the matrix is to relax the residual stresses. This is manifested as a reduction in the G_{ir} values obtained after slicing. We notice from Table 2 that with increase in the amount of plastic strain the energy release rates reduce to levels which are comparable with those obtained for CMCs.

The relative contribution of the fiber axial residual stress to the overall residual stress state is also examined. The strain energy in the fiber can be estimated from the axial residual stress (neglecting other stress components) in the fiber using the following relation:

$$U = \frac{\sigma^2}{2E} \pi r^2 l \quad (4.15)$$

where E is the Young's modulus of the fiber and r is its radius. The strain energy release rate contribution from the fiber can be computed by differentiating the above relation with respect to the crack surface area A . This is given by

$$\frac{\partial U}{\partial A} = \frac{\sigma^2}{4E} r \quad (4.16)$$

Eqn. 4.16 gives the contribution of axial residual stress towards the strain energy release rate G_{ir} . It can be seen that the energy computed from this equation depends only on the stress level and the Young's modulus of the fiber. To examine the validity of this equation, a parametric study is conducted for different levels of elastic mismatch given by E_M/E_F which is related to the Dundur's parameter α^{33} . The strain energy release rates computed from the EDI method are shown in Table 3 along with the corresponding residual stress values. The error in the estimation of G_{ir} due to residual stress from Eqn. 4.16 and the EDI method is plotted in Figure 4.7. It can be seen that the % error decreases as $\alpha \rightarrow 0$ (the case of $E_{matrix} = E_{fiber}$). This can be attributed to the crack driving force being of the same order in the fiber and in the matrix as $\alpha \rightarrow 0$. This analysis also implies that axial residual stress is a major contributor to G_{ir} . For the composite system SCS-6/Ti-15-3 ($E_M/E_F=0.23$) under consideration in this study, the error in the G_{ir} calculation is about 25% (Figure 4.7).

4.4.2 Debond Initiation

Previous studies⁶ have indicated that in the presence of processing induced residual stresses, debonding initiated at the support end for the thicknesses of the order of 0.5 mm or lower considered in this work. This observation is supported by experimental push-out test results³⁴. In this paper the energy release rates for both the ends at the time of crack initiation are examined. The applied displacement u has been normalized with respect to u_{max} in the plots where u_{max} is the maximum applied displacement at which debond initiation occurs. The results for the loading and support ends are shown in Figure 4.8. From this figure it is observed that the energy release rate for the support end keeps on increasing (from the value at the end of the slicing stage) till the assigned critical value of the energy release rate G_{ic} of 50 J/m^2 is reached at which point crack initiation occurs. This is in contrast to the energy release rate curve for the loading side which shows negligible change from its value at the end of the slicing stage. This phenomenon is a direct consequence of the presence of processing induced residual stresses. As mentioned in the previous section, even before the application of load, the fibers have a tendency to protrude from the ends due to the redistribution of residual stresses after slicing. When the load is applied the axial residual stresses at the support end are in the same direction as the applied load whereas at the loading end they oppose the applied load. This causes the stress intensity at the support end to increase and thus debonding initiates from this end. In this case the strain energy at the support end shoots up and reaches the critical value even before any appreciable change is seen at the loading end.

The application of push-out load is simulated after altering the residual stress state by introducing plastic strains in the matrix by subjecting the specimen to tensile loads (refer section 4.1). The variation of these stresses with equivalent plastic strain is shown in Figure 4.9. Results for three specimens which are subjected to three different applied strains of (a) 0.9% (b) 1.3% and (c) 1.5% are presented in this section. The strain energy release rates for crack initiation for these cases are taken to be different (21 J/m^2 for cases (a) and (b) and 7 J/m^2 for case (c)) from the zero plastic strain case discussed earlier. This is done for keeping the loads about the same for crack initiation. The emphasis here is not to extract the critical energy release rates, but to study the variation of the strain energy release rates with increasing load. The variation of strain energy release rates at the loading and support ends are discussed in the subsequent paragraphs.

In the first case the specimen is subjected to 0.9% strain, sliced and then compressive load is applied on the fiber. The variation of energy release rates at the two ends of the specimen after slicing and upto initiation of debonding are shown in Figure 4.10. The behavior exhibited in this case by the energy release rates is similar to the case when no tensile strain is applied. The support end G_i continues to increase until debonding is initiated at this end. However G_i for the loading end decreases in magnitude from the value at the end of slicing and reaches very small values and maintains these values for the rest of the initiation stage. The decrease in G_i at the loading end is due to the drop in the stress intensity at this end as the influence of the axial residual stresses is reduced.

In the second case the specimen is subjected to 1.3% tensile strain before slicing. The G_{ir} value after slicing is only of the order of $4 J/m^2$ compared to the as-received value of the order of $40 J/m^2$. The results for this case are shown in Figure 4.11. The variation of the energy release rates show a markedly different behavior from the previous cases. Towards the beginning, the energy release rates for both ends increase more or less similarly. With increase in displacement the loading end energy release rate attains values far higher than that of the support end. Debonding finally initiates at the loading end. It has to be noted that in this case the ratio of the energy release rates at the two ends is much lower compared to the earlier cases. This case is very near the transition of the debond initiation switching from the support to the loading end.

In the third case the specimen is strained to 1.5% strain uniaxially. The axial residual compressive stresses in the fiber are completely removed. The energy release rates for both ends of the specimen are shown in Figure 4.12. In this case debonding is observed to initiate from the loading side similar to the behavior exhibited by CMCs^{10,16} where residual stresses are negligible. The energy release rate for the loading side gradually increases in magnitude till debonding occurs. The support end energy release rates remains constant and do not increase. This effect is observed experimentally by Majumdar et al³⁴.

To evaluate the response of CMCs, the push out test is simulated for the SCS-6/Borosilicate system for the same thickness. The residual stresses induced in this case due to processing are much smaller compared to the stresses induced in MMCs. The energy release rates upto debond initiation are shown in Figure 4.13. With application of load by the indenter the loading end energy release rates continue to increase until debonding initiates from this end. The energy release rates for the support end show negligible change from the value at the end of the slicing stage which leads us to conclude that debonding is not likely to initiate from this end. Fiber will get pushed out when the loading end crack reaches the support end. These results illustrates the considerable role played by processing induced residual stresses on interface debonding initiation.

4.4.3 Application of the EDI Method to Interfacial Crack Propagation

The EDI method is advantageous for crack propagation studies as non-singular elements can be used in the region around the crack tip. This eliminates the need to remesh with every stage of crack advance. The crack is advanced when the energy release rate for the crack tip G_i exceeded the prescribed G_{ic} of $50 J/m^2$. The behavior exhibited by the energy release rates during the course of crack propagation is examined for the SCS-6/Ti-15-3 system. After the processing stage, the specimen is sliced and load is applied with a punch till the fiber is completely debonded. The sequence of debonding is shown in Figure 4.14. In this figure the crack tip locations for both sides are plotted as a function of fiber displacement u which has been normalized with respect to maximum fiber displacement u_{max} . $u/u_{max} = 0$ indicates the end of the slicing stage and start of the application of load by the punch.

$u/u_{max} = 1$ indicates the stage where the fiber gets pushed out. The location of the crack tip x is normalized with respect to the specimen thickness L . The curve which represents the support side crack tip location rises steadily till it intersects the curve which represents the loading end crack. At this point the fiber gets pushed out. The curve which represents the loading end crack maintains zero slope for all of the duration of the push-out test indicating that this crack does not propagate.

The energy release rates for both ends are measured during the course of debonding and are shown in Figure 4.15. From this figure we see that the energy release rates for the support end rises until debonding occurs. From the point of debond initiation till the fiber gets pushed out, the energy release rate remains essentially constant. When complete debonding takes place and the fiber gets pushed out, the energy levels drop to a negligible value. The energy release rate curve for the loading side exhibits a behavior different from that of the support. In this case the energy release rate shows negligible change from the value obtained at the end of the slicing stage until the support side crack tip crosses the centre of the specimen. Then the energy release rates continue to decrease until very near the stage at which the fiber gets pushed out. This is because the effect of the compressive residual stresses (acting opposite to the direction of the applied load) decreases which leads to a reduction in stress intensity at the loading end crack tip. When the fiber gets pushed out the support end energy release rate drops to a very low value as the resistance to further sliding is only due to friction.

4.5 Summary and Conclusions

A fracture mechanics approach based on the J-integral, computed using the Equivalent Domain Integral (EDI) method, is used to examine the interfacial debonding process in MMCs and CMCs during a fiber push-out test. Strain energy release rates for the fiber-matrix interface due to processing induced residual stresses are determined by the above method. These rates serve as a lower bound for the Mode II fracture toughness of the composite systems examined. The phenomenon of bottom (support end) debonding observed in MMC systems during the push-out test is explained by the study of the variation of energy release rates for the loading and support end cracks upto debond initiation. The effect of residual stresses on crack initiation is studied by altering the residual stress state by plastic straining. It is found that crack initiation switches from the support to the loading end with reduction in residual stresses with increase in plastic strain. For the specimen geometry and material system studied, this switching occurs when the G_{ir} values drop to values of the order of $4J/m^2$ from the as-received value of around $40J/m^2$. It is shown that the EDI method can be used to simulate interface crack propagation without the need for remeshing with crack advance. Evaluation of strain energy release rates through the use of J-integral for cracks along bimaterial interfaces in the presence of friction is still a "mathematical problem" and care needs to be exercised in the interpretation of the numerical predictions.

Bibliography

1. Nimmer, R. P., Bankert, R. J., Russel, E. S., Smith, G. A. & Wright, P. K., Micromechanical Modeling of Fiber-Matrix Interface Effects in Transversely Loaded SiC/Ti-6-4 Metal Matrix Composites, *Journal of Composites Technology and Research*, **13**, 1 (Spring 1991), pp. 3-13.
2. Majumdar, B. S. & Newaz, G. M., Inelastic Deformation of Metal Matrix Composites: Plasticity and Damage Mechanisms, *Philosophical Magazine A*, **66**, 2 (1992), pp.187-212.
3. Brindley, P. K. & Draper, S. L., Failure Mechanisms of 0° and 90° SiC/Ti-24Al-11Nb Composites Under Various Loading Conditions. In *Structural Intermetallics*, ed. R. Darolia, J. J. Lewandowski, C. T. Liu, P. L. Martin, D. B. Miracle & M. V. Nathal. The Minerals, Metals & Materials Society, 1993, pp. 727-737.
4. Ghosn, L. J., Eldridge, J. I. & Kantzos, P., Analytical Modeling of the Interfacial Stress State During Pushout Testing of SCS-6/Ti-Based Composites, *Acta Metallurgica et Materialia*, **42**, 11 (1994), pp. 3895-3908.
5. Ananth, C. R. & Chandra, N., Numerical Modeling of Fiber Push-out Test in Metallic and Intermetallic Matrix Composites - Mechanics of the Failure Process, *Journal of Composite Materials*, **29**, 11 (1995), pp. 1488-1514.
6. Chandra, N. & Ananth, C. R., Analysis of Interfacial Behavior in MMCs and IMCs using Thin-slice Push-out Tests, *Composites Science and Technology*, **54**, 1 (1995), pp. 87-100.
7. Leung, C. K. Y. & Li, V. C., New Strength based Model for the Debonding of Discontinuous Fibres in an Elastic Matrix, *Journal of Materials Science*, **26** (1991), pp. 5996-6010.
8. Kim, J-K., Zhou, L. & Neu, R. W., Effects of Fibre Volume Fraction on the Stress Transfer in Fibre Pull-out Tests, *Composites*, **25**, 7 (1994), pp. 470-475.
9. Hsueh, C. H., Interfacial Debonding and Fiber Pull-out Stresses of Fiber-reinforced Composites, *Materials Science and Engineering*, **A123** (1990), pp. 1-11.
10. Kerans, R. J. & Parthasarathy, T. A., Theoretical Analysis of the Fiber Pullout and Pushout Tests, *Journal of American Ceramic Society*, **74**, 7 (1991), pp. 1585-1596.
11. Stang, H. & Shah, S. P., Failure of Fiber-Reinforced Composites by Pull-out Fracture, *Journal of Materials Science*, **21** (1986), pp. 953-957.

12. Gao, Y. C., Mai, Y. W. & Cotterell, B., Fracture of fiber-reinforced materials, *Journal of Applied Mathematics and Physics*, **39** (July 1988), pp. 550-72.
13. Butler, E. P., Fuller Jr, E. R. & Chan, H. M., Interface Properties for Ceramic Composites from a Single-Fiber Pull-out Test, *Materials Research Society Symposium Proceedings*, **170**, 1990, pp. 17-24.
14. Hutchinson, J. W. & Jensen, H. M., Models of Fiber Debonding and Pull-out in Brittle Composites with Friction, *Mechanics of Materials*, **9** (1990), pp. 139-163.
15. Marshall, D. B., Analysis of Fiber Debonding and Sliding Experiments in Brittle Matrix Composites, *Acta Metallurgica et Materialia*, **40**, 3 (1992), pp. 427-441.
16. Liang, C. & Hutchinson, J. W., Models of the Fiber Pushout Test, *Mechanics of Materials*, **14** (1993), pp. 207-221.
17. Ananth, C. R. & Chandra, N., Evaluation of Interfacial Shear Properties of Metal Matrix Composites from Fiber Push-out Tests, *Mechanics of Composite Materials and Structures*, **2** (1995), pp. 309-328.
18. Eldridge, J. I., Fiber Push-out Testing of Intermetallic Matrix Composites at Elevated Temperatures. In *Intermetallic Matrix Composites II*, ed. D.B. Miracle, D.L. Anton & J.A. Graves, Materials Research Society Symposium Proceedings, **273**, 1992, pp. 325-330.
19. Nikishkov, G. P. & Atluri, S. N., An Equivalent Domain Integral Method for Computing Crack Tip Integral Parameters in Non-Elastic, Thermomechanical Fracture, *Engineering Fracture Mechanics*, **26** 1987, pp. 851-867.
20. Nikishkov, G. P. & Atluri, S. N., Calculation of Fracture Mechanics Parameters for an Arbitrary Three-Dimensional Crack by the Equivalent Domain Integral Method, *International Journal for Numerical Methods in Engineering*, **24** (1987), pp. 1801-1821.
21. Raju, I. S. & Shivakumar, K. N., An Equivalent Domain Integral Method in the Two-Dimensional Analysis of Mixed Mode Crack Problems, *Engineering Fracture Mechanics*, **37**, 4 (1990), pp. 707-725.
22. Nishioka, T. & Atluri, S. N., On the Computation of Mixed-mode K-factors for a Dynamically Propagating Crack Using Path-independent Integrals, *Engineering Fracture Mechanics*, **20** (1984), pp. 193-208.
23. Ishikawa H., A finite element analysis of Stress Intensity Factors for Combined Tensile and Shear Loading by only a Virtual Crack Extension, *International Journal of Fracture*, **16** (1980), pp. R243-R246.
24. MARC Analysis Corporation, *MARC version: K6, User Manuals*, (1996).
25. Deng, X., An Asymptotic Analysis of Stationary and Moving Cracks with Frictional Contact Along Bimaterial Interfaces and in Homogeneous Solids, *International Journal of Solids and Structures*, **31** (1994), pp. 2407-2429.
26. Deng, X., Mechanics of Debonding and Delamination in Composites: Asymptotic Studies, *Composites Engineering*, **5**, 10-11 (1995), pp. 1299-1315.

27. Deng, X., *Private Communication*, (1996).
28. Roman, I. & Jero, P. D., Interfacial Shear Behavior of Two Titanium-Based SCS-6 Model Composites. In *Intermetallic Matrix Composites II*, ed. D.B. Miracle, D.L. Anton and J.A. Graves. Materials Research Society Symposium Proceedings, **273**, 1992, pp. 337-342.
29. Arnold, S. M., Arya, V. K. & Melis, M. E., Elastic/Plastic Analyses of Advanced Composites Investigating the Use of the Compliant Layer Concept in Reducing Residual Stresses Resulting from Processing, NASA TM 103204, 1990.
30. Majumdar, B. S. & Newaz, G. M., Isothermal Fatigue Mechanisms in Ti-Based Metal Matrix Composites. NASA CR 191181, 1993.
31. Grande, D. H., Mandell, J. F. & Hong, K. C. C., Fiber-matrix bond strength studies of glass, ceramic, and metal matrix composites, *Journal of Materials Science*, **23**, 1 (1988), pp. 311-328.
32. Kroupa, J. L. and Neu, R. W., The Nonisothermal Viscoplastic Behavior of a Titanium-Matrix Composite, *Composites Engineering*, **4**, 9 (1994), pp. 965-977.
33. Dundurs, J., Discussion, *Journal of Applied Mechanics*, **36** (1969), pp. 650-652.
34. Majumdar, B. S. & Miracle, D. B., Interface Measurements and Applications in Fiber Reinforced MMCs, *Journal of Key Engineering Materials - Special issue on Interfaces in Composites and Laminated Structures*, **116-117** (1996), pp. 153-172.

Table: Material properties for ceramic matrices

Matrices	E (GPa)	G (GPa)	α ($\times 10^{-6} / ^\circ \text{C}$)
Borosilicate	68	28	3.2
CAS I	88	36	5.0

Material properties obtained from: Ref. 31

Table 4.1: Material properties for ceramic matrices

Table: Computed strain energy release rates for different composite systems

Material System (fiber volume fraction= 0.35)	ΔT ($^\circ \text{C}$)	Fiber Residual Stress		G_i (Residual) (J/m^2)
		Axial (MPa)	Radial (MPa)	
SCS-6/Ti-15-3 \diamond	790	-750	-223	37.6
SCS-6/Ti-6-4 *	875	-858	-272	42.3
SCS-6/Timetal 21s †	875	-985	-304	47.6
SCS-6/CAS I \div	1230	-220	-100	7.86
SCS-6/Borosilicate \div	600	20	8	0.19
SCS-6/Ti-15-3 (after straining to 0.5% strain)		-582	-248	14.5
SCS-6/Ti-15-3 (after straining to 1.3% strain)		-423	-94	3.79

Material properties obtained from:

\diamond Ref. 30

* Ref. 1

† Ref. 32

\div Ref. 31

Table 4.2: Material properties for ceramic matrices

Table : Parametric study to examine effect of elastic mismatch

Material System * (fiber volume fraction = 0.35)	Dundur's Parameter α	Fiber Residual Stress Axial (MPa)	Radial (MPa)	G_i (Residual) (J/m ²)
$E_m = 0.23 E_f$	0.619	-750	-223	37.6
$E_m = 0.3 E_f$	0.489	-906	-387	62.3
$E_m = 0.5 E_f$	0.320	-1120	-458	73.9
$E_m = 0.75 E_f$	0.128	-1350	-497	84.5
$E_m = E_f$	-0.015	-1450	-536	94

* Thermal properties used is the same as that of SCS-6/Ti-15-3 composite

E_f - Young's Modulus of Fiber

E_m - Young's Modulus of Matrix

Table 4.3: Material properties for ceramic matrices

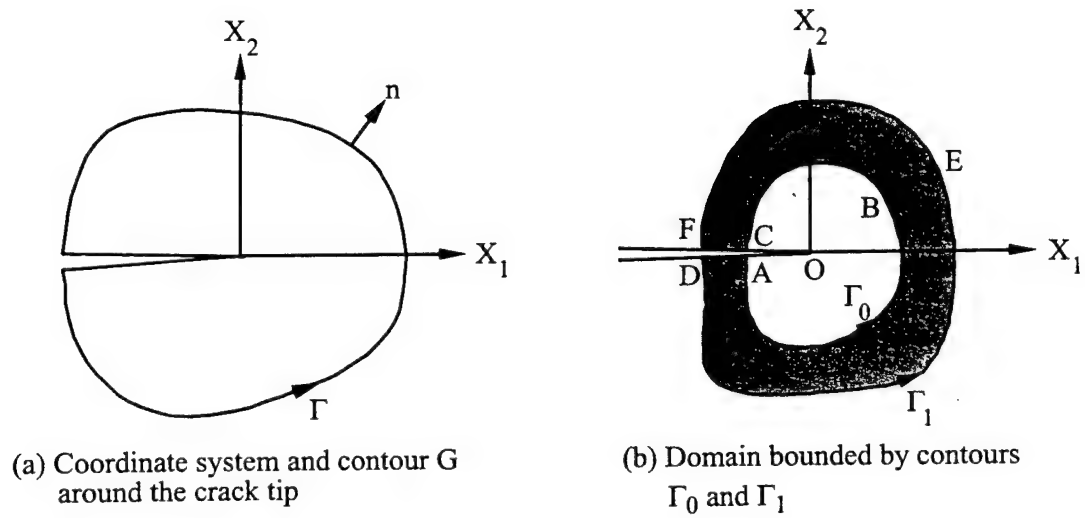


Figure 4.1: Contours used in the Equivalent Domain Integral Method

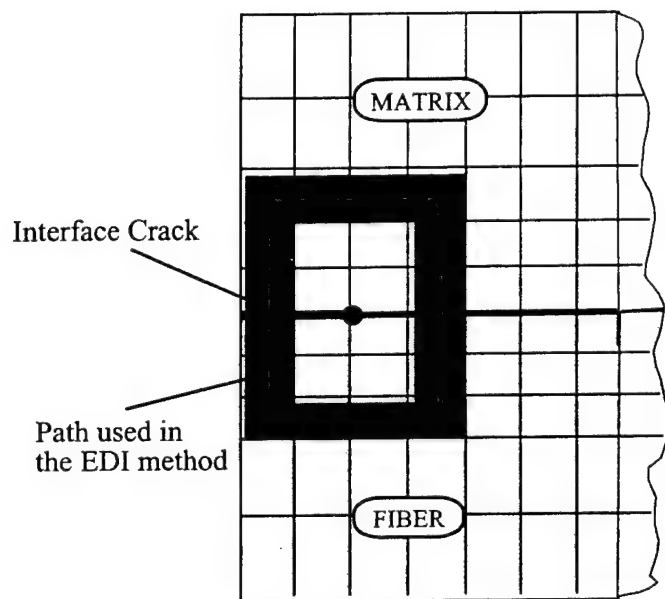


Figure 4.2: Typical path used in the energy release rate computations

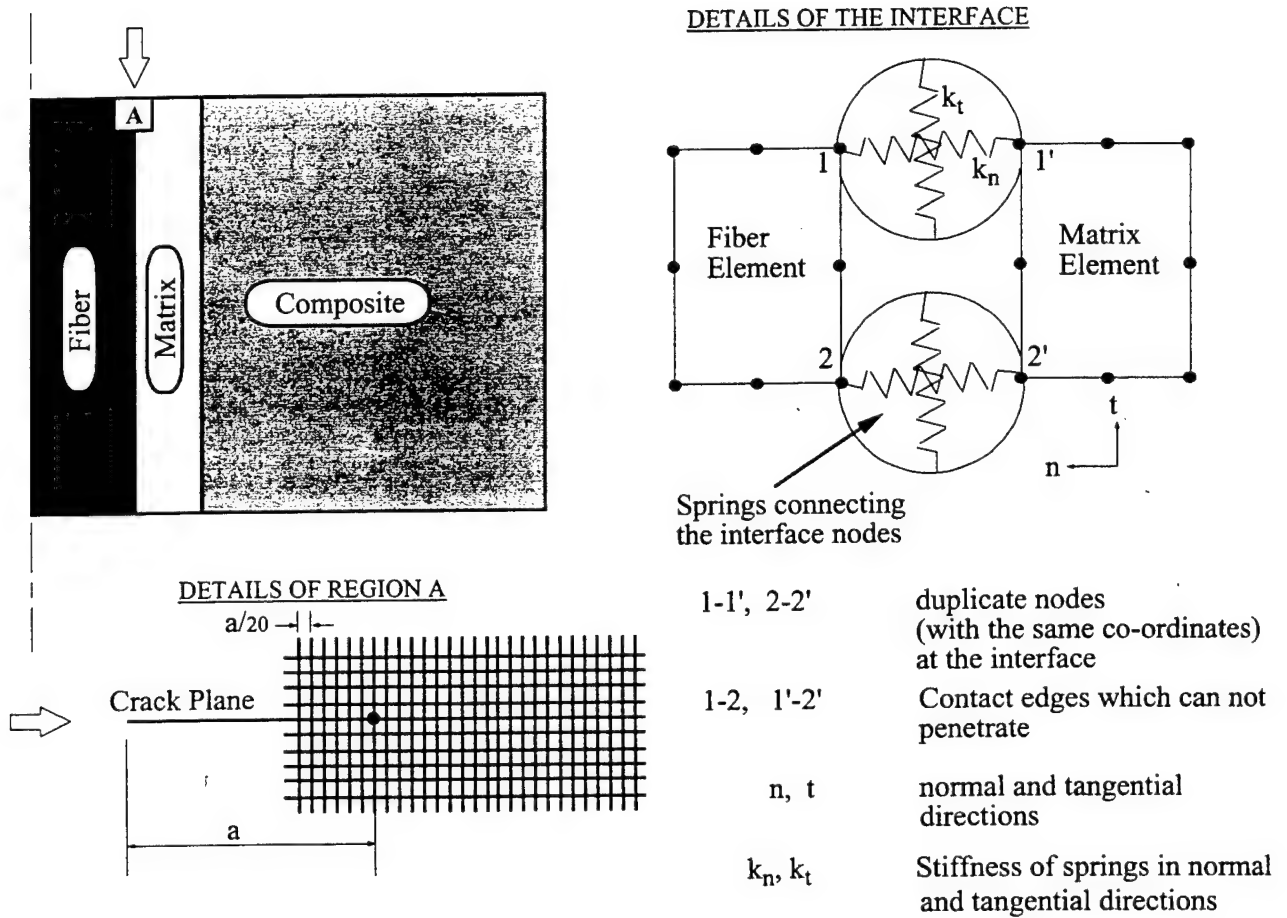
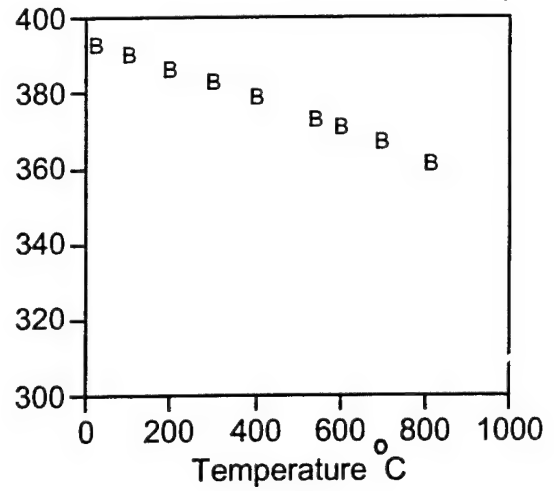
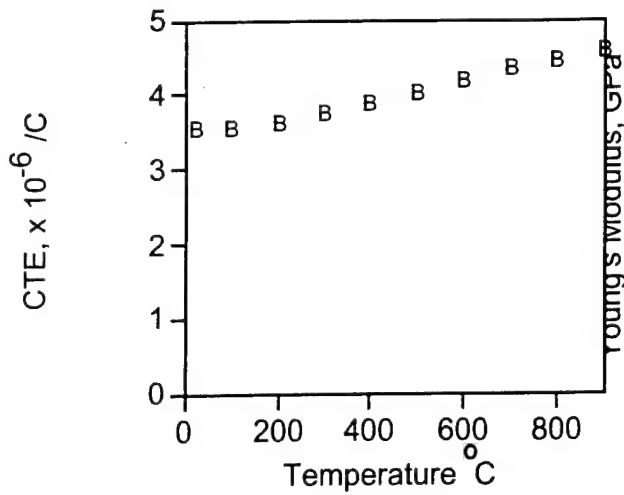


Figure 4.3: Finite element model and details of the interface

Fiber: Silicon Carbide (SCS-6); $\nu = 0.25$; diameter = 140 μm



Matrix:

Ti-15V-3Al

$\nu = 0.36$

Timetal 21s

$\nu = 0.34$

Ti-6Al-4V

$\nu = 0.3$

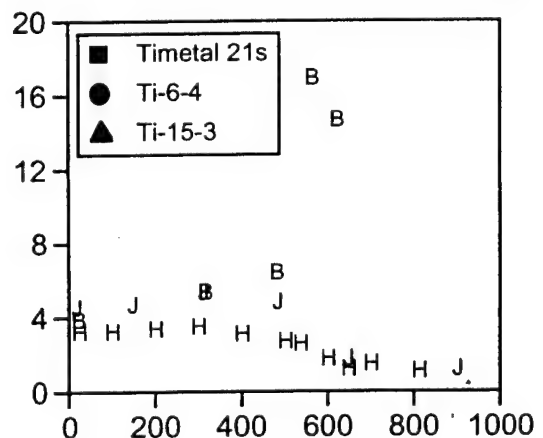
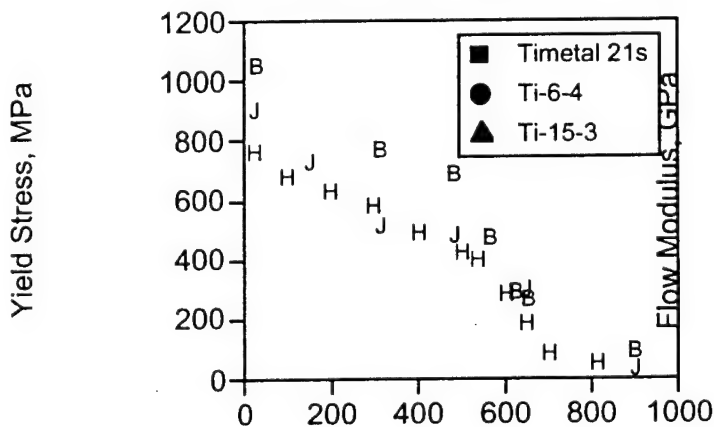
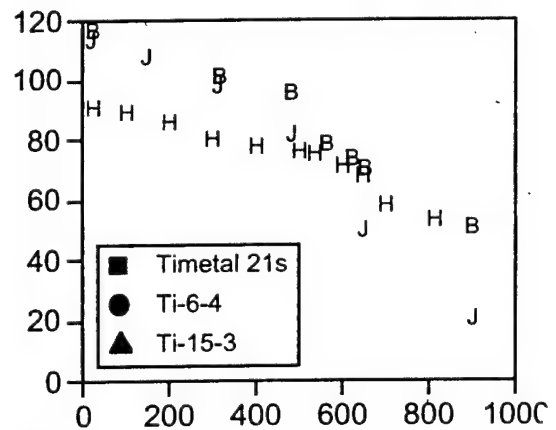
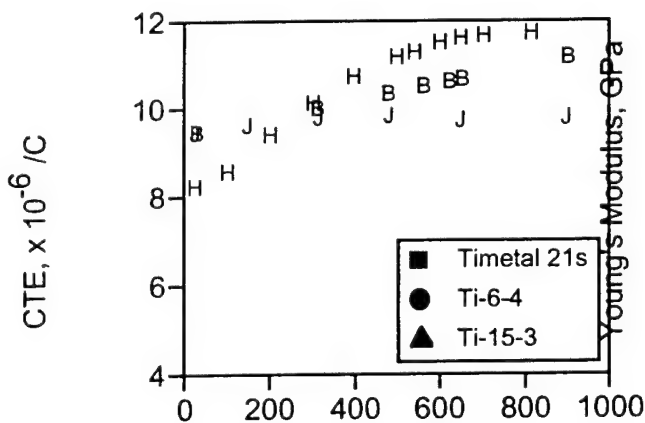


Figure 4.4: Variation of material properties with temperature

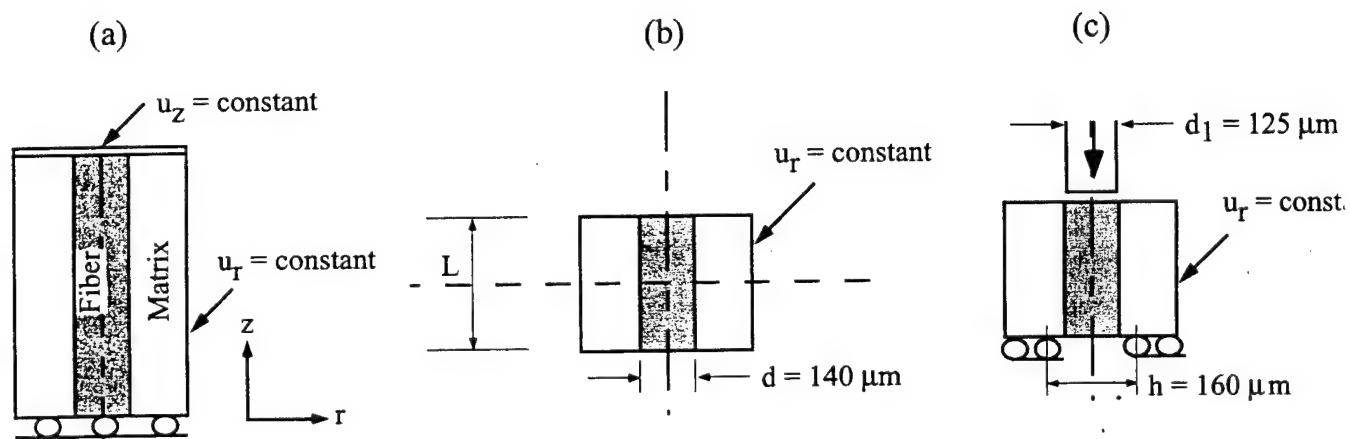


Figure 4.5: Boundary conditions used in the Finite Element Analysis

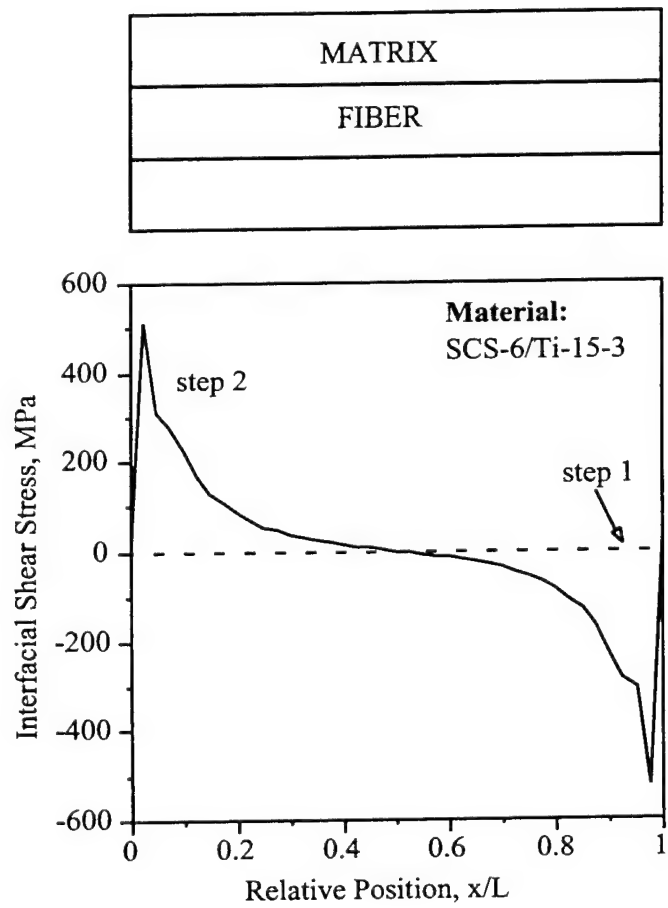


Figure 4.6: Shear stress distributions along the interface for specimen thickness of 0.5 mm

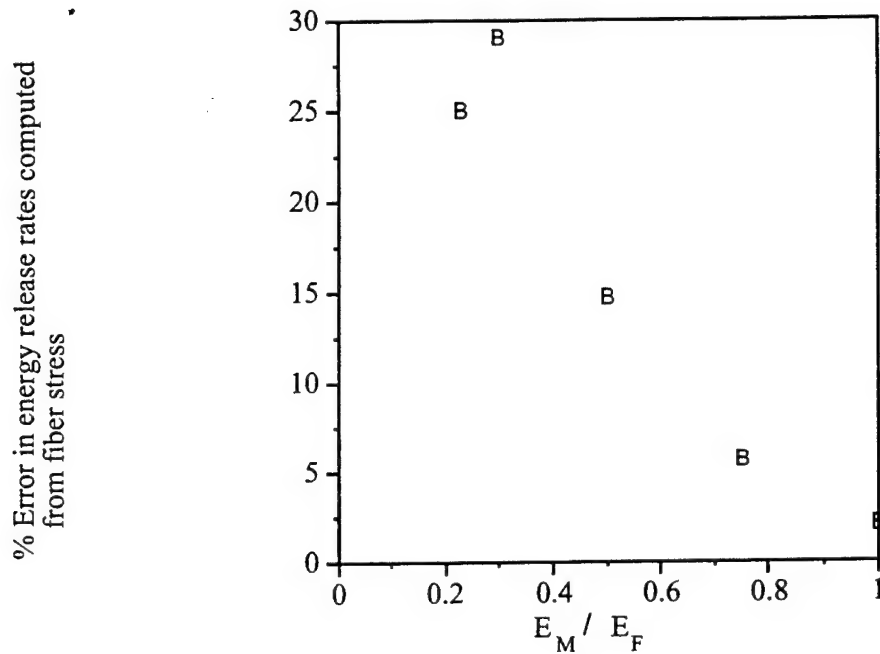


Figure 4.7: Percentage error in energy release rates calculated using the axial fiber residual stress plotted as a function of the ratio of the matrix modulus to the fiber modulus

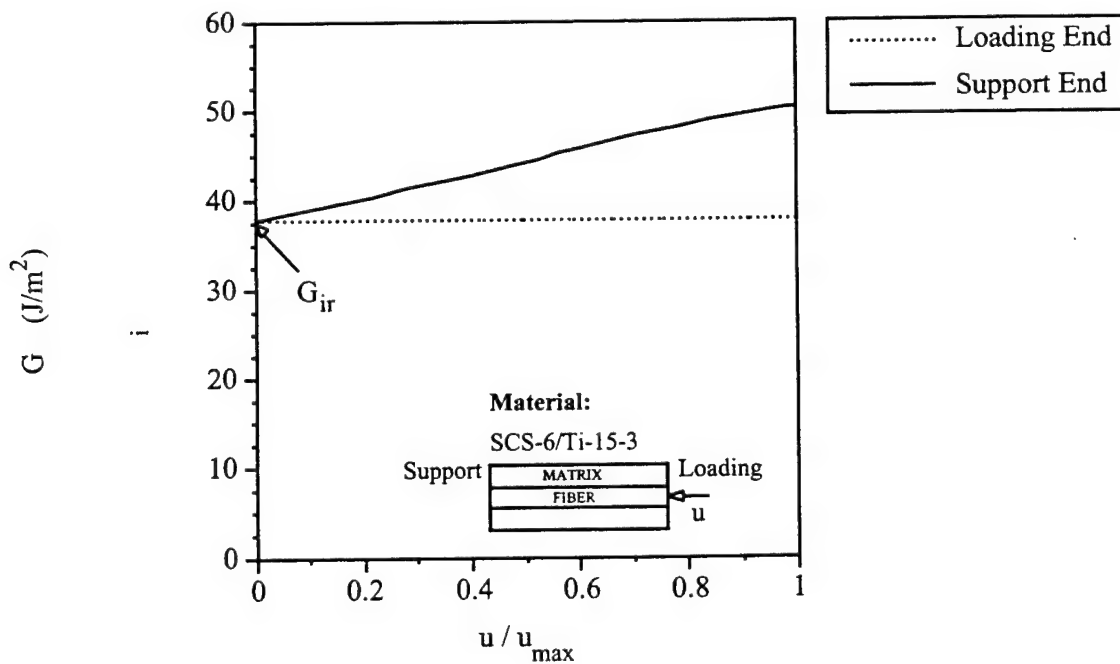


Figure 4.8: Variation of the energy release rates from the end of the processing stage till debond initiation as a result of indenter load application

Fiber Residual Stress (absolute, MPa)

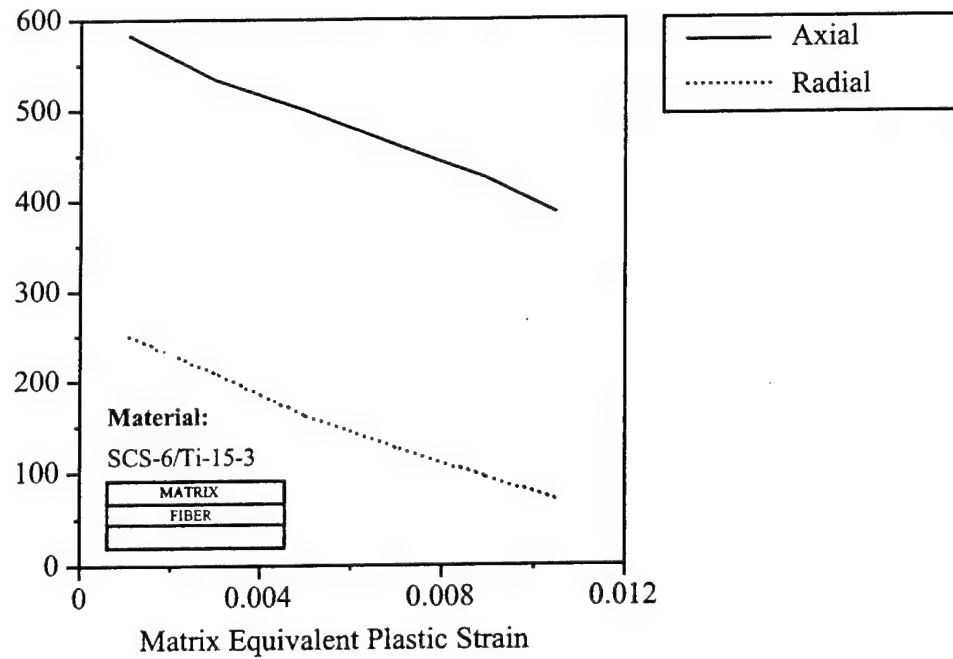


Figure 4.9: Variation of axial and radial components of residual stress in the fiber with equivalent plastic strain induced in the matrix as a result of straining

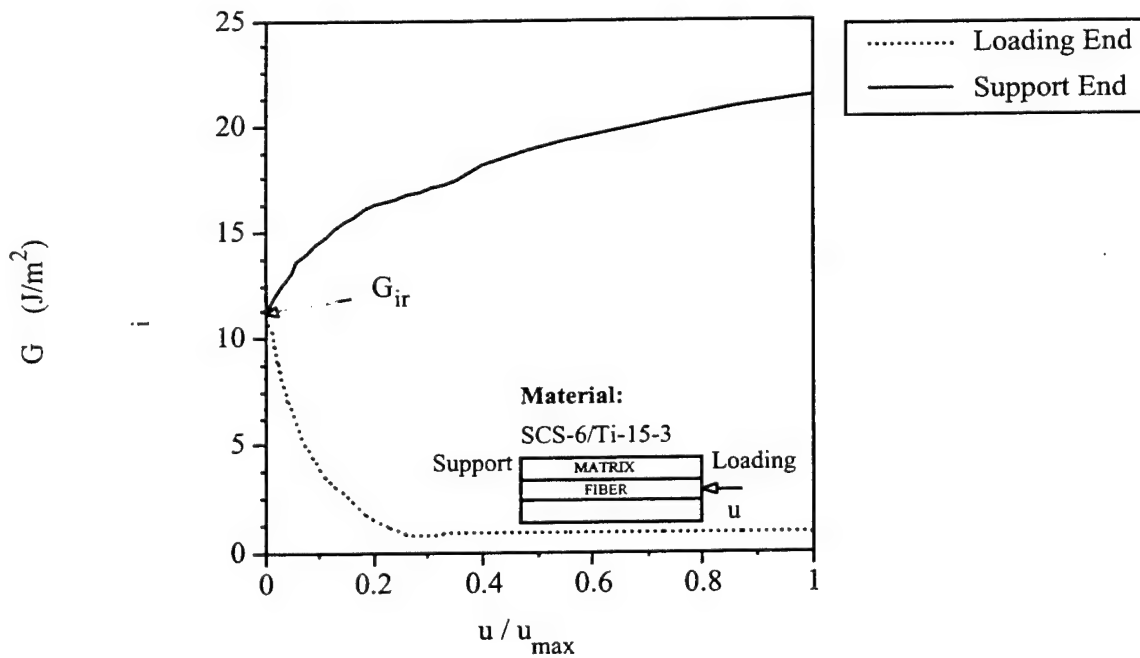


Figure 4.10: Variation of energy release rates till debond initiation upon application of load by the indenter after straining to 0.9 % total strain

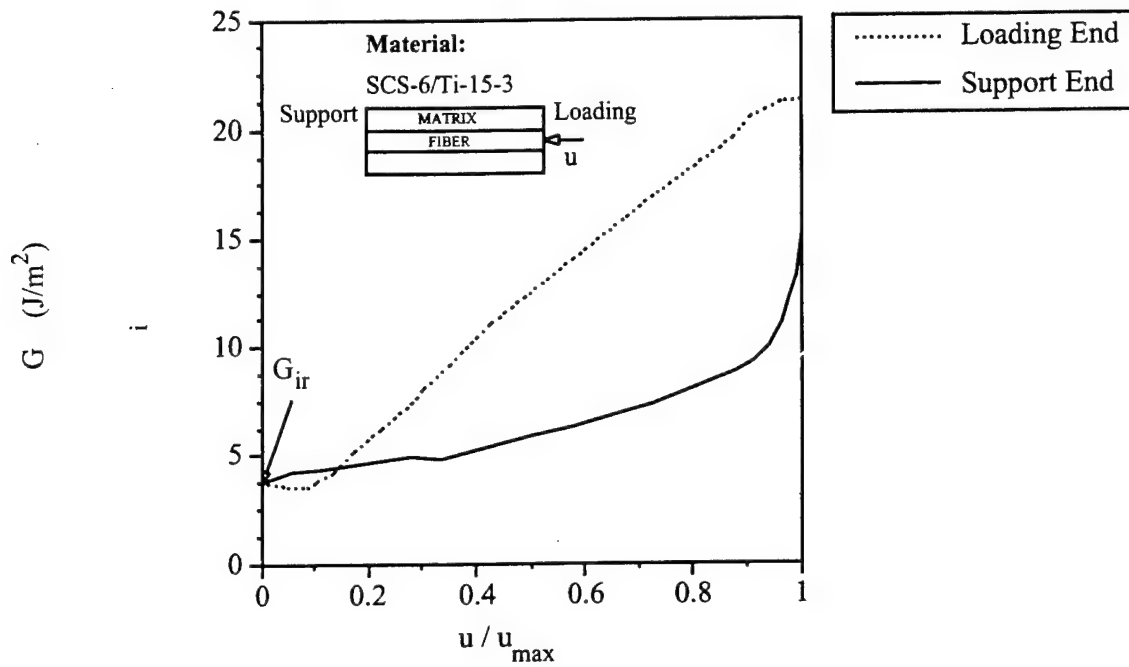


Figure 4.11: Variation of energy release rates till debond initiation upon application of load by the indenter after straining to 1.3 % total strain

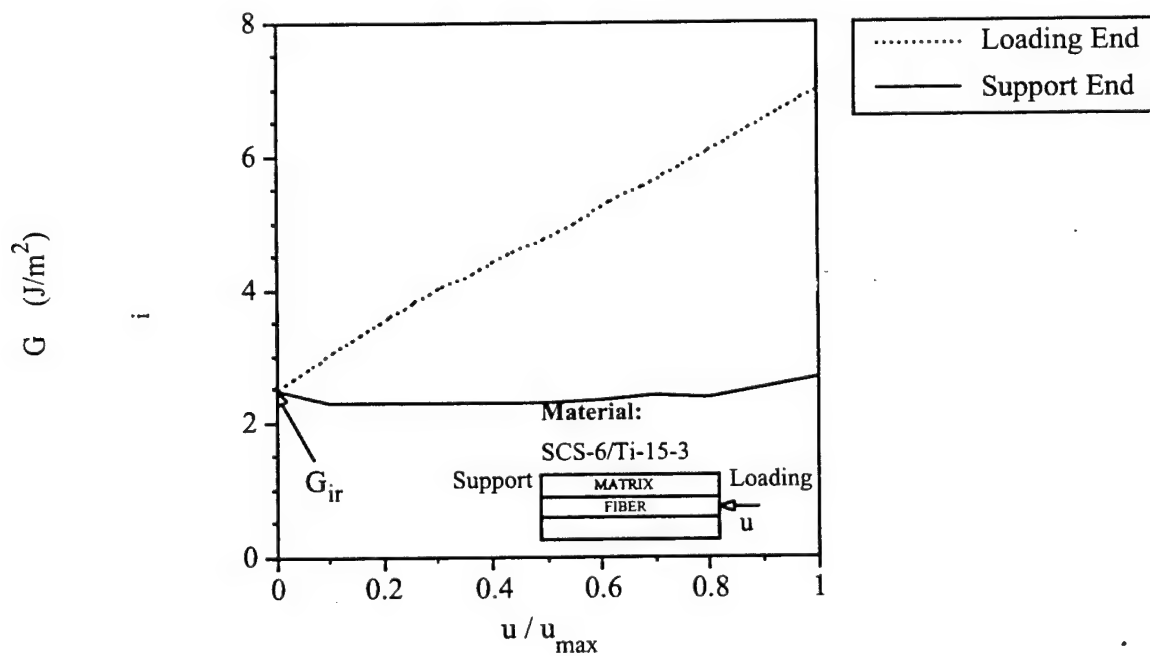


Figure 4.12: Variation of energy release rates till debond initiation upon application of load by the indenter after straining to 1.5 % total strain

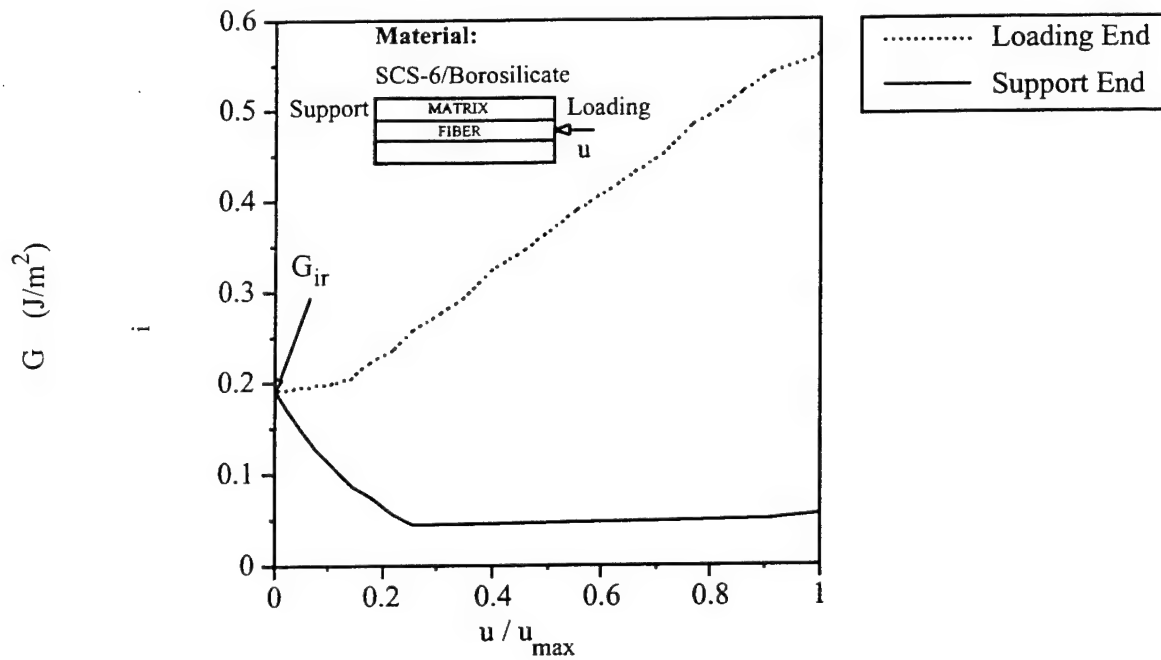


Figure 4.13: Variation of energy release rates till debond initiation upon application of load by the indenter for ceramic matrix composites

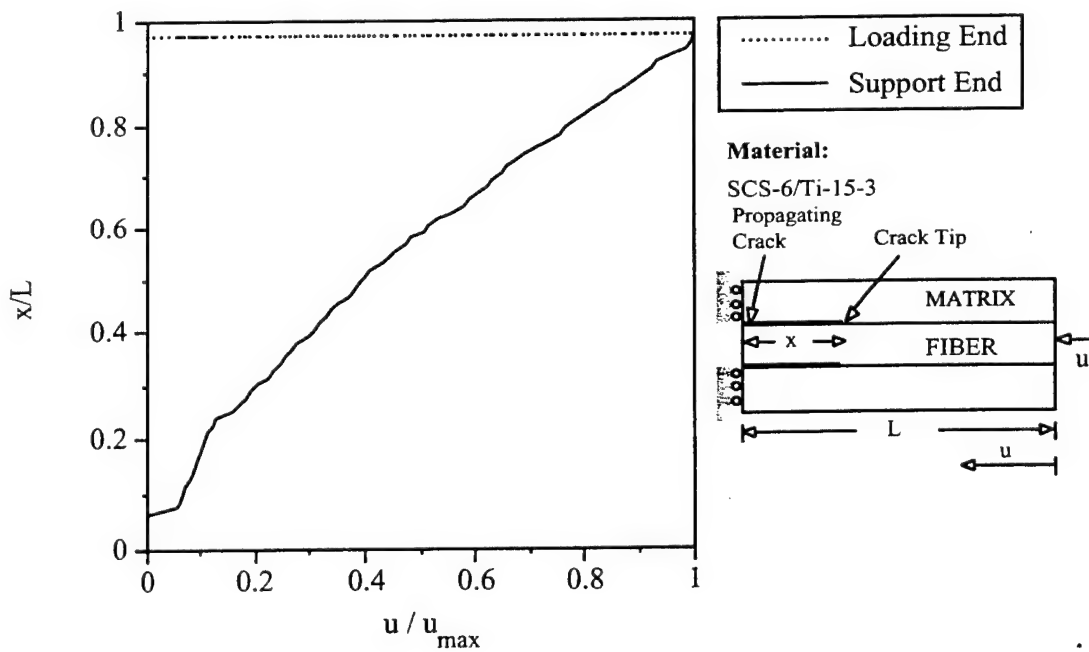


Figure 4.14: Crack tip locations for the loading and support ends from the end of processing stage till the fiber gets pushed out

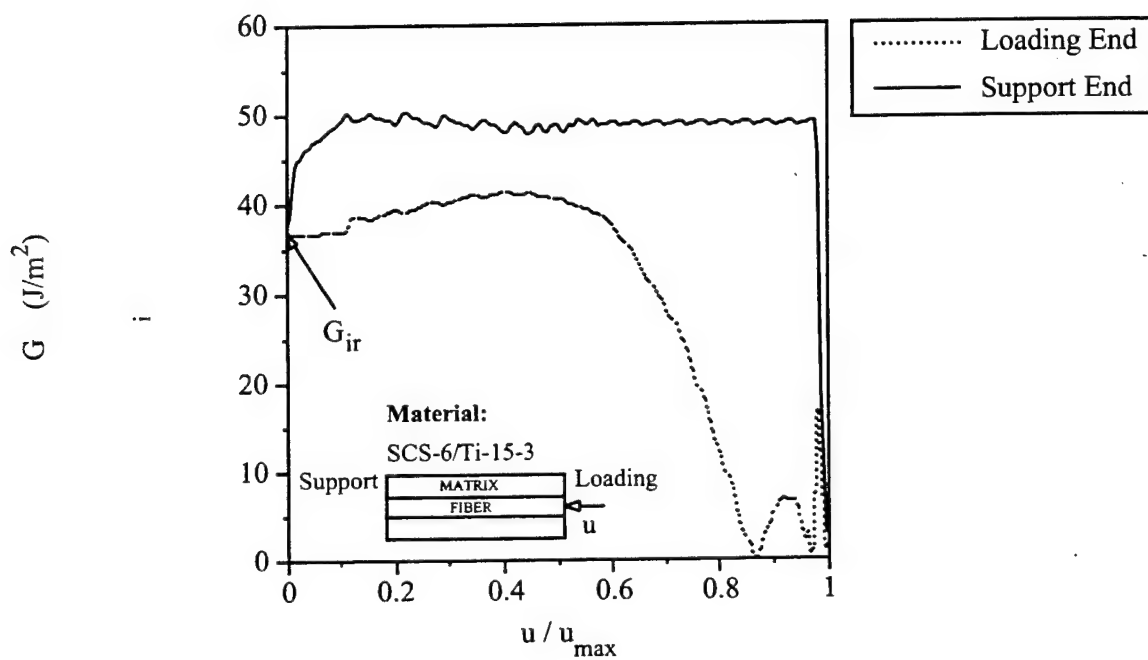


Figure 4.15: Variation of energy release rates from the end of processing stage till the fiber gets pushed out

Chapter 5

Evaluation of Fracture Toughness of MMC Interfaces Using Thin-slice Push-out Tests

5.1 Introduction

Metal matrix composites (MMC) are being considered as potential material systems of choice for the advanced propulsion systems of twenty-first century aircraft, owing to their high specific stiffness and strength. The role of fiber-matrix interface in MMCs is critical to the performance of these composites. Push-out test is emerging as an important experimental tool for characterizing the interface behavior of MMCs mainly after its widespread use in the study of interfaces in ceramic matrix composites (CMC). The presence of high levels of residual stresses in MMCs alters the mechanics of the failure process, making the interpretation of test results and evaluation of interfacial properties very difficult. Moreover the relatively high bond strength of MMCs and residual clamping stresses at the interface limit the specimen thickness for push-out experiments. In the thin slice push-out tests it is observed that [1] interface failure initiates from the bottom of the specimen and not from the loading end as in the case of CMCs [2]. Chandra and co-workers [2,3,4] analyzed the thin-slice push-out test and simulated the initiation of interface failure and its propagation using non-linear finite element methods. This work was able to explain many of the experimental observations [5] of push-out behavior at room and elevated temperatures. They also proposed a method for evaluating the interfacial shear strength from the push-out data. However fracture toughness (G_{ic}) is increasingly being considered as a more appropriate quantitative measure of the bond at the interface. The interfacial fracture energies of metal matrix composites are not currently available in the literature because of the difficulty in evaluating these from the experimental results.

In this paper, a numerical method based on the equivalent domain integral technique developed previously is used to simulate the fracture process during a thin slice push-out test

and determine the critical interfacial fracture toughness G_{ic} . Experimental correlations are made with push-out test results of ceramic matrix composites to validate the G_{ic} predictions using the EDI method. This approach is then used to evaluate the G_{ic} of some as processed SCS-6/Titanium matrix composites from the experimental data.

5.2 Numerical Simulation of the Push-out Test Using Finite Element Method

The thin slice push out test involves pushing a fiber out of a composite specimen by the application of compressive load through a flat indenter. Modeling such a test involves three major stages. Step 1 involves modeling the composite consolidation at high temperatures and then cooling down to room temperature which induces residual stresses in the composite. Step 2 is the specimen preparation stage consisting of slicing a thin push-out specimen from the bulk composite which results in stress redistribution at the two ends of a fiber. Step 3 is modeling the loading stage where compressive load is applied to the fiber until it is pushed out of the specimen. A detailed description of the above sequence of steps is provided elsewhere [2]. The test is analyzed using an axisymmetric cylindrical model. A three phase model consisting of fiber, matrix and a composite phase with homogeneous properties has been used. The interface is modeled as a contact surface and the bonding at the interface is simulated using high stiffness springs. The interface failure process is modeled using a strain energy based failure criteria given by:

$$G_i \geq G_{ic} \quad (5.1)$$

where G_i is the strain energy release rate for the interface crack and G_{ic} is the critical value of the strain energy release rate. The interface crack propagates further when its strain energy release rate exceeds the critical value. The total strain energy release rate of the propagating interface crack is computed using the Equivalent Domain Integral (EDI)[6,7] method. The EDI method was implemented in the commercial finite element analysis software MARC [8] through user subroutines. A schematic of the finite element model is shown in Figure 5.1. A small interface crack of the order of $0.5r_f$ (where r_f is the fiber radius) is introduced at both the ends of the specimen during step 2 of the simulation for the purpose of computation of energy release rates. A path of radius $r_c = 0.075r_f$ from the crack tip is consistently used in all the cases to compute G_i as theoretical studies [9] have shown that the strain energy release rate is mathematically zero at the crack tip for a crack at a bimaterial interface in the presence of Coulomb friction.

5.3 Results and Discussion

The numerical method described in the previous section is applied to different composite systems. The material properties and the reference temperatures are taken from available

literature [10,11,12,13]. The levels of the axial residual stress in the fiber predicted by the numerical simulation for SCS-6/Ti-15-3 (fiber volume fraction = 0.35) shown in Table 1 is of the order of 750 MPa. This compares reasonably well with the values of 749 ± 47 MPa measured experimentally by Pickard et al.[14] using the dissolution technique. The values obtained for other composite systems are also shown in Table 1.

Slicing of a push-out specimen from a bulk composite (step 2) results in the redistribution of the residual stresses near the composite ends. This causes stress concentration at the pre-existing cracks at both the ends of the specimen. The calculations of G_{ir} (the value of G_i after slicing and before the application of indenter load; purely due to residual stresses) from the EDI method for different material systems are also shown in Table 1. It can be seen that a G_{ir} of 37.6 J/m^2 is present at the specimen ends for SCS-6/Ti-15-3. The stress state at both ends of the specimen is symmetric in nature. This leads to symmetric values for the energy release rates at both the ends of the specimen. This also indicates the tendency of the fiber to protrude out of the matrix at either end. G_{ic} , which is the critical value required for debonding is taken to be higher than G_{ir} in these simulations, as microscopic studies of MMC specimens do not reveal significant interfacial debonding before the application of the mechanical load. Hence the values of G_{ir} listed in Table 1 serve as a lower bound for G_{ic} of these MMC systems. The processing simulations are also performed on typical CMCs such as SCS-6/CAS I and SCS-6/Borosilicate to compare energy release rate values with those obtained for the MMCs. As expected the G_{ir} values for the CMCs were at least one order less than those for the MMCs. This is to be expected since the residual stresses generated in the CMCs are much smaller compared to that in MMCs.

Previous studies [4] have indicated that in the presence of processing induced residual stresses debonding initiated at the support end for MMCs for the thicknesses of the order of 0.5 mm. Profilograph measurements are conducted on interrupted push-out test specimens before and after the tests and are shown in Figure 5.2. The loaded fiber (Fiber 2 in Figure 2) does not show any change in height after the tests on the loading side whereas the measurements on the support end indicate that the loaded fiber pops significantly out of the matrix. Positions of the fiber at both ends of the specimen before and after application of the load from the numerical simulation is shown in Figure 5.3. From this figure it can be seen that the numerical simulations show a behavior similar to that observed in the experiments. The shear stress distribution along the interface obtained from the simulation is shown in Figure 5.4 when the debonded length has reached $0.6t$ where t is the thickness of the specimen. The crack tip is characterized by the high shear stress levels. From this figure it can be clearly observed that the debonding is proceeding from the support end. A typical load displacement curve obtained from the simulation and variation of energy release rates for the loading and support end cracks is shown in Figure 5.5. From the energy variation curve it is seen that the energy release rates for the support end increase from the value at the end of the slicing stage till the critical value when debonding initiates. For the period in which steady propagation takes place, the support end energy release rates maintain a constant level close to the critical value. Unsteady propagation is characterized by the energy release rates shooting up and then falling as the fiber is about to be pushed out. The energy release rates for the loading end maintains a value which is much smaller than the critical value for

most of the duration of debonding and rises up to meet the support end value just as the fiber is about to be pushed out.

The debonding process in MMCs is significantly affected by the presence of processing induced residual stresses and results in debonding initiating from the support end. The state of residual stress at the interface can be modified by prestraining the composite to levels sufficiently high so as to introduce plastic strains in the matrix. Push-out experiments conducted by Majumdar et. al [15] on SCS-6/Ti-15-3 specimens which were prestrained to 0.9% strain in tension prior to push-out showed that debonding initiation switched from the support end to the loading end. This test is also simulated numerically. The shear stress distribution along the interface from the simulation is shown in Figure 5.6 when the specimen is loaded to 28 N which is considerably less than the push-out load. It can be seen from this figure that the debonding is propagating from the loading end which is similar to the behavior observed experimentally. It was also seen experimentally that the push-out load increased considerably when the specimen is prestrained. From the numerical simulations it was observed that for SCS-6/Ti-15-3 specimen which was prestrained debonding did not even initiate for the load of ≈ 20 N (Table 2) which corresponds to the peak load for as received specimens.

As mentioned previously interfacial fracture properties for MMCs are not currently available in the literature as there are no established procedures for evaluating them from test data. These are essential to fully characterize interface behavior. The numerical simulations are repeated at varying values of G_i . The peak loads obtained from the simulations are correlated with experimental data [16,17,18] to arrive at the critical strain energy release rate of the interface G_{ic} which is a material property. In order to validate the numerical predictions the push-out test was simulated for Silicon Carbide/Reaction bonded Silicon carbide ceramic matrix composite as the residual stresses are minimum in CMCs and the fracture energies are already reported [19]. The predicted value of G_{ic} using our methodology matched closely with the value of 2.1 J/m^2 reported for the experimental peak load as shown in Table 2. The above methodology is applied to different MMC systems (Table 2). As expected the G_{ic} values of the MMCs are considerably higher than the CMC systems considered in this study. It can also be seen that the predicted fracture toughnesses are about 10 J/m^2 higher than the values of G_{ir} the energy obtained after slicing for the MMCs. This indicates that most of the energy contribution to the failure process comes from the residual stresses. Also the interfacial fracture energies of the three systems are not far apart being in the range of $50\text{-}60 \text{ J/m}^2$. These values are on the lower side as they are based on the minimum energies required for fiber push-out assuming that there are no pre-existing flaws such as matrix cracks in the vicinity of the interface. The interface model used in this work does not take into account the mechanical locking effect due to asperities at the interface which may increase the apparent G_{ic} values. Efforts are underway to incorporate this effect.

5.4 Summary and Conclusions

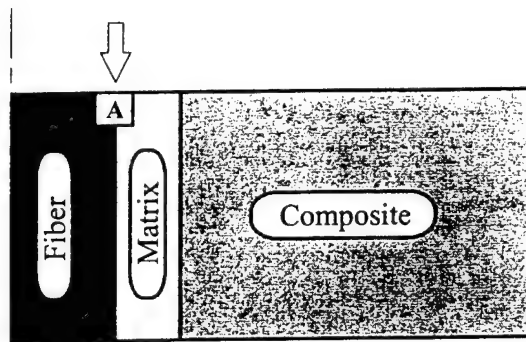
A fracture mechanics based approach is used to compute residual and interfacial fracture energies of some MMC and CMC systems during push-out tests. The phenomenon of bottom debonding in MMC thin slice specimens is examined using experimental results and strain energy computations. Residual stress predictions are correlated with experimentally reported values. The main contribution to the interfacial fracture toughness in MMCs is found to be from the residual stresses and thus the values of G_{ir} can be considered as a lower bound for the critical strain energy release rate of the interface G_{ic} . This factor is also demonstrated in the push-out test simulations for pre-strained specimens, where in the absence of residual stresses, a far higher push-out load is necessary for the same critical strain energy release rate; consequently no fiber push-out is observed at lower loads. Interface fracture toughnesses for certain typical MMC and CMC systems are predicted using the developed methodology.

5.5 Bibliography

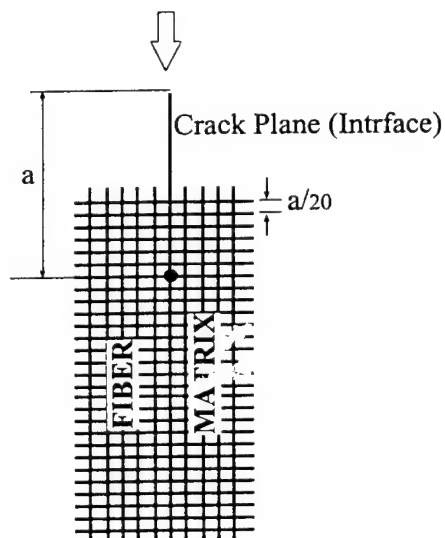
1. L. J. Ghosn, J. I. Eldridge and P. Kantzos, *Acta Metallurgica et Materialia*, **42**, 11, 3895 (1994).
2. C. R. Ananth and N. Chandra, *Journal of Composite Materials*, **29**, 11, 1488 (1995).
3. C. R. Ananth and N. Chandra, *Mechanics of Composite Materials and Structures*, **2**, 309 (1995).
4. N. Chandra and C. R. Ananth, *Composites Science and Technology*, **54**, 1, 87 (1995).
5. J. I. Eldridge, *Intermetallic Matrix Composites II, MRS Symposium Proceedings*, 273, p. 325, Materials Research Society (1992).
6. G. P. Nikishkov and S. N. Atluri, *Engineering Fracture Mechanics*, **26**, 851 (1987).
7. I. S. Raju and K. N. Shivakumar, *Engineering Fracture Mechanics*, **37**, 4, 707 (1990).
8. MARC, User Manual, (1995).
9. X. Deng, *International Journal of Solids and Structures*, **31**, 2407 (1994).
10. R. P. Nimmer, R. J. Bankert, E. S. Russel, G. A. Smith and P. K. Wright, *Journal of Composite Technology and Research*, **13**, 1, 3 (1991).
11. B. S. Majumdar and G. M. Newaz, Technical Report NASA CR 191181, NASA (1993).
12. D. H. Grande, J. F. Mandell and K. C. C. Hong, *Journal of Materials Science*, **23**, 1, 311 (1988).
13. J. L. Kroupa and R. W. Neu, *Composites Engineering*, **4**, 9, 965 (1994).
14. S. M. Pickard, D. B. Miracle, B. S. Majumdar, K. L. Kendig, L. Rothenflue and D. Coker, *Acta Metallurgica et Materialia*, **43**, 8, 3105 (1995).
15. B. S. Majumdar and D. B. Miracle, *Journal of Key Engineering Materials - Special Issue on Interfaces in Composites and Laminated Structures*, **116-117**, 153 (1996).
16. J. I. Eldridge and B. T. Ebihara, *Journal of Materials Research*, **9**, 4, 1035 (1994).
17. I. Roman and P. D. Jero, *Intermetallic Matrix Composites II, MRS Symposium Proceedings*, **273**, p. 337, Materials Research Society (1992).
18. K. M. Fox and P. Bowen, *Metallurgy and Technology of Practical Titanium Alloys*, 337,

Metallurgy and Technology of Practical Titanium Alloys, p. 333, The Minerals, Metals & Materials Society (1994)

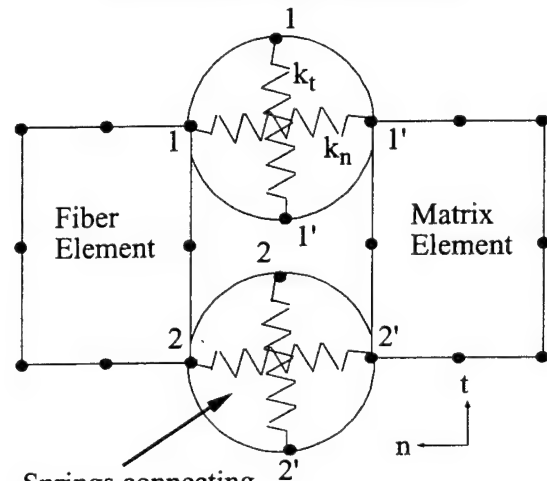
19. W. A. Curtin, J. I. Eldridge and G. V. Srinivasan, *Journal of the American Ceramic Society*, **76**, 9, 2300 (1993)



DETAILS OF REGION A



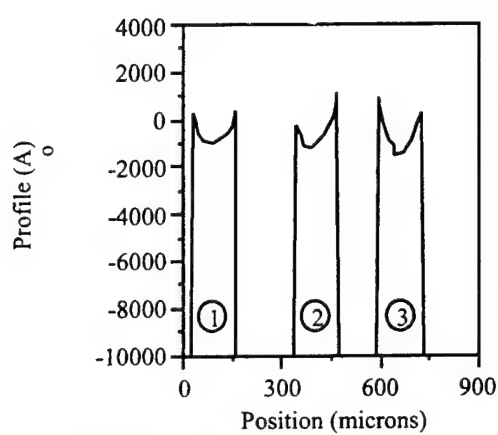
DETAILS OF THE INTERFACE



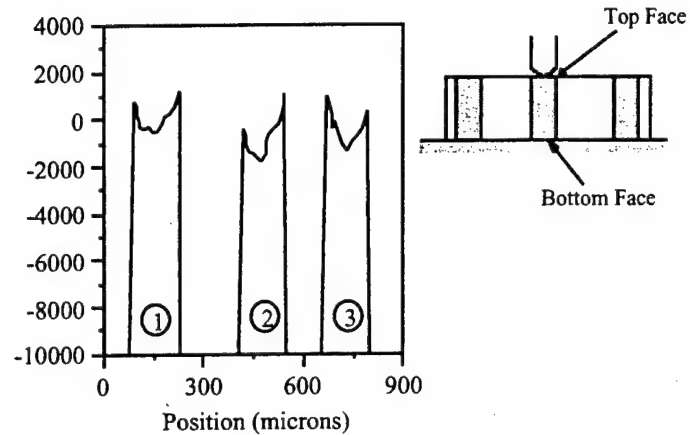
Springs connecting the interface nodes

- | | |
|------------|---|
| 1-1', 2-2' | duplicate nodes
(with the same co-ordinates)
at the interface |
| 1-2, 1'-2' | Contact edges which cannot
penetrate |
| n, t | normal and tangential
directions |
| k_n, k_t | Stiffness of springs in normal
and tangential directions |

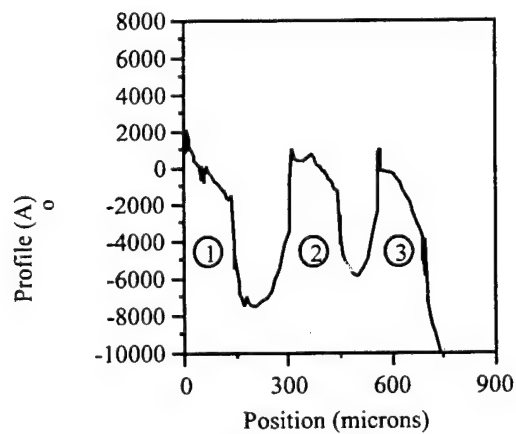
Figure 5.1: finite element model



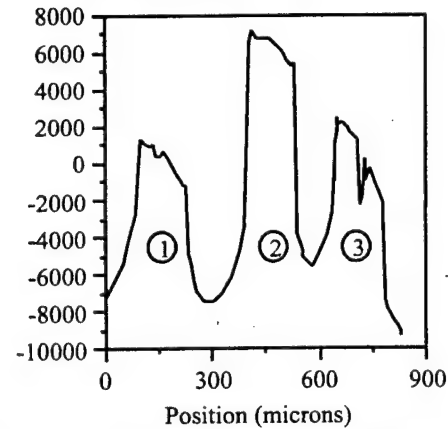
(a) Top face of as received specimen before loading



(b) Top face of as received specimen after loading fiber 2 to 37 N



(c) Bottom face of as received specimen before loading



(d) Bottom face of as received specimen after loading fiber 2 to 37 N

Figure 5.2: profilometry-as received specimen

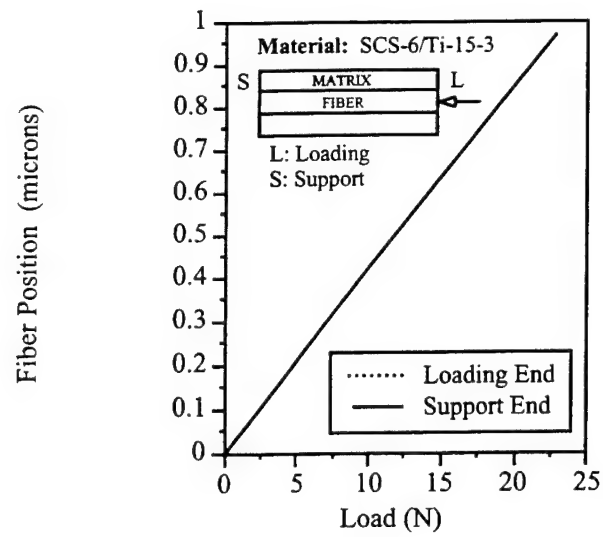


Figure 5.3: profilometry-as received specimen

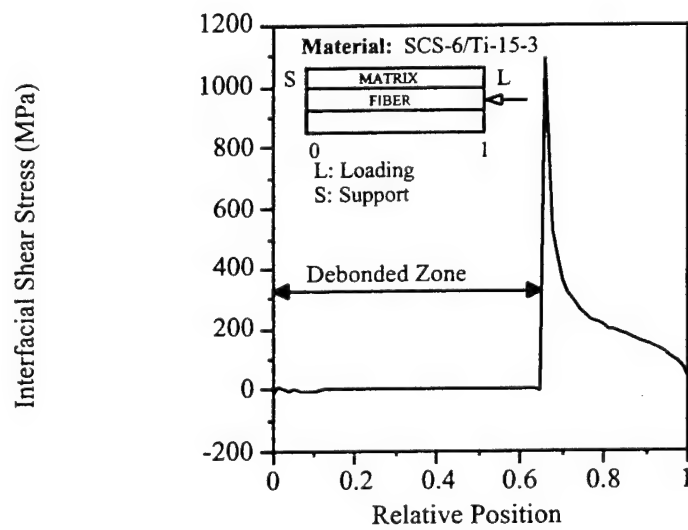


Figure 5.4: shear stress for residual stress case

Figure 3. Position of center of fiber for loading and support ends

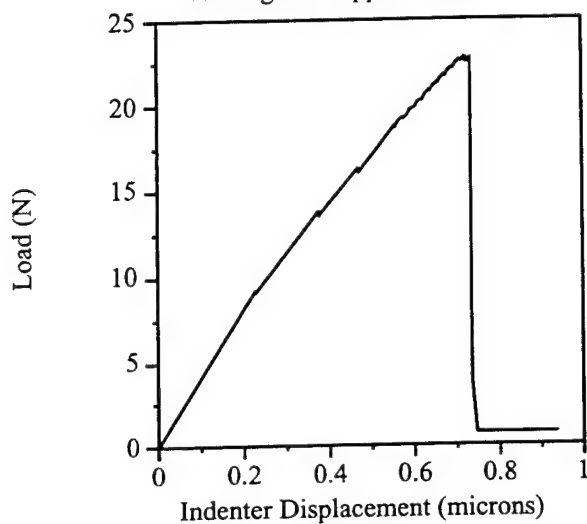


Figure 4. Shear stress distribution along the interface when residual stresses are present

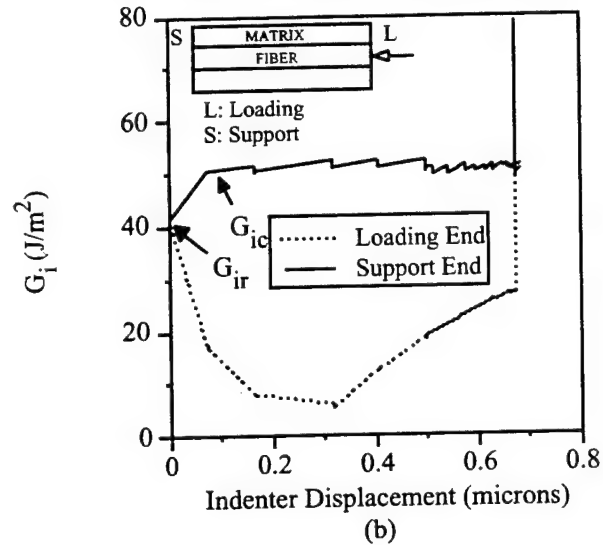


Figure 5.5: profilometry-as received specimen

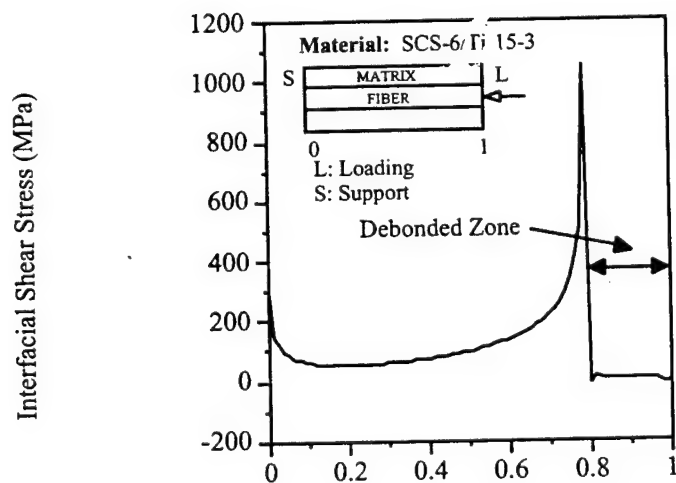


Figure 5.6: shear stress for no residual stress case

Chapter 6

Effect of Fiber Fracture and Interfacial Debonding on the Evolution of Damage in Metal Matrix Composites

6.1 Introduction

The failure of fiber-reinforced metal matrix composites is a complex process involving various mechanisms such as fiber fracture, interfacial debonding and matrix plasticity. The interaction of these mechanisms makes the damage in composites a highly non-linear process. While progress has been made in understanding and quantifying damage in composite materials, there is no established procedure base on how to assess and characterize damage [1].

Voyiadjis [2] studied the initiation and evolution of damage in a composite lamina using a damage tensor to describe the initiation, growth and coalescence of voids, cracks and debonding. The damage tensor on this case was developed based on laminate experimental data and not from the micromechanical level. Ladeveze [3] focused on modeling damage to include micromechanical effects at a macroscopic level. Continuum damage mechanics principles were used to describe matrix micro-cracking and fiber-matrix debonding. The longitudinal, transverse and shear behavior of a carbon-epoxy lamina was arrived at experimentally and applied to laminates. However, fiber fracture and debonding were not modeled explicitly. Allen investigated the issue of delamination of composite laminates and treated the problem using a stochastic approach. Robertson and Mall [4] investigated the problem of micromechanical damage using the 'Method of Cells' approach by Aboudi [5] to predict the mechanical response of metal matrix composite (MMC) laminates under fatigue loading.

Recent work by Lacy et al. [6] have emphasized the need for accounting for the interaction

of damage entities. They showed that the distribution and interaction of damage entities at the micro-scale (within a Representative Volume Element) can affect the evolution of the damage (and hence the final failure) significantly, while having only a minor effect on the effective moduli. Hence, the size, distribution and interaction of the defects need to be explicitly taken into account in the damage evolution studies.

6.2 Damage Mechanics

A general formulation for the thermomechanical response of a composite body undergoing damage can be derived from [7] the Helmholtz free energy potential ψ :

$$\psi = \frac{1}{2\rho} C_{ijkl}^* \epsilon_{ij}^e \epsilon_{kl}^e + \psi_p \quad (6.1)$$

$$\sigma_{ij} = \rho \frac{\partial \psi}{\partial \epsilon_{ij}^e} = C_{ijkl}^* \epsilon_{kl}^e \quad (6.2)$$

where

ψ_p - plastic part of the potential which is not dependent on the damage

ρ - Density

C_{ijkl}^* - Elastic tensor modified by damage

$C_{ijkl}^* = (I_{ijrs} - D_{ijrs}) C_{rskl}$ where D_{ijrs} is the damage tensor

C_{ijkl} - Elastic tensor without damage

ϵ_{kl}^e in equation 6.2 is the elastic strain which is defined as $\epsilon_{kl}^t - \epsilon_{kl}^i$, where ϵ_{kl}^t is the total strain and ϵ_{kl}^i is the inelastic strain due to plasticity and creep. For the special case of 2-D transversely isotropic material which is the case of the composite lamina, C_{ijkl}^* or the stiffness matrix S_{ijkl}^* which is its inverse reduces to the following:

$$S_{ijkl}^* = \begin{bmatrix} S_{11}^* & S_{12}^* & 0 \\ S_{12}^* & S_{22}^* & 0 \\ 0 & 0 & S_{66}^* \end{bmatrix} \quad (6.3)$$

$$\begin{aligned} S_{11}^* &= \frac{1}{E_{11}(1 - D_{11})}; S_{22}^* = \frac{1}{E_{22}(1 - D_{22})}; \\ S_{12}^* &= \frac{\nu_{12} D_{12}}{E_{11}(1 - D_{11})}; S_{21}^* = \frac{\nu_{21} D_{21}}{E_{22}(1 - D_{22})}; \\ S_{66}^* &= \frac{1}{G_{12}(1 - D_{66})} \end{aligned}$$

D_{11} , D_{22} , D_{12} , D_{21} and D_{66} are the damage parameters. As $S_{12}^* = S_{21}^*$, D_{12} and D_{21} are related. This reduces the number of independent damage parameters for the 2-D transversely isotropic case to four. These parameters can be determined from longitudinal and transverse tension tests as well as shear tests.

Currently, experimental methods are being used to investigate the role of local failure mechanisms on the macroscopic behavior of composites. Local damage in a fiber-reinforced composite can be affected by several geometric and material parameters, e.g. fiber volume fraction, fiber arrangement, mechanical and statistical properties of the fiber, matrix constitutive behavior, interfacial strength and any local perturbations of the above parameters. This makes experimental quantification of damage under different conditions (geometrical, material and loading) difficult. In this study computational techniques are used to simulate the micromechanical tests for extracting the damage parameters. This enables a parametric study of the influence of micromechanical parameters such as fiber, matrix and interfacial properties, fiber arrangement and volume fraction on the damage evolution.

6.3 Monte Carlo simulation

As mentioned earlier, fracture of fiber-reinforced metal matrix composites (MMCs) is a complex process involving several mechanisms that cause deterioration of composite properties such as fiber fracture, interfacial debonding and matrix plasticity. Among the above mechanisms, matrix plasticity and interfacial debonding are essentially deterministic, but the fracture of brittle fibers is stochastic in nature. Fiber failure occurs over a range of stress values determined by the random distribution of microscopic flaws in the fiber (Curtin [2, 3]).

A simulation of damage in a composite laminate can account for the stochastic variations of the strengths of the fiber using a Monte Carlo simulation [10]. This method has been used to analyze a wide range of physical processes [11]. In general, it involves a computer simulation using random numbers to solve stochastic problems [12]. Such simulations may be regarded as 'numerical experiments'. Voleti et al. [13] applied Monte Carlo simulation procedure to model the fiber failure process in single fiber composite test. The stochastic variation of the fiber strength along its length is modeled using a 'two-parameter Weibull model' [14], which is described in detail in the next subsection.

6.3.1 Statistical Model for Fiber Strength and its Distribution

A statistical method commonly used to determine the strength of a brittle fiber is the Weibull model [14]. In this model, it is assumed that the fiber material is isotropic and statistically homogeneous [15]. This method has been used to model fiber-fragmentation test or single fiber composite test, which has been used in the study of fiber-matrix interface properties [13, 11, 12] of polymer matrix composites.

Coleman [18] examined the strength of long fibers taken from a common source (e.g. a spool of fiber). He showed that $P(\sigma_f)$, the cumulative strength distribution function, has the form of a Weibull distribution (σ_f is the failure stress of a fiber). The cumulative probability of failure for a fiber of length ratio L is given by:

$$P_f(\sigma_f) = 1 - e^{-L(\frac{\sigma_f}{\sigma_0})^m} \quad (6.4)$$

where P_f is the probability of failure of a fiber at a stress level equal to or less than σ_f , σ_0 is the Weibull scale parameter for the unit fiber length ratio, 'm' is the Weibull shape parameter and 'L' is the length ratio with respect to a reference length (the fiber length at which the σ_0 and 'm' are determined). The Weibull scale and shape parameters for a fiber material are determined from several experiments [1].

The above model is adapted to perform the Monte Carlo simulation of a single-fiber-composite test using the following approach. In this method, the length of the given fiber is divided into a fixed number of equally-sized 'links' [20]. The strength of a link (σ_l) of any length (l) is given by the following equation:

$$\sigma_l = \sigma_0 \left(\frac{L_0}{l} \right)^{1/m} \quad (6.5)$$

where, L_0 is the gage length at which the Weibull scale parameter σ_0 is determined experimentally. In a fiber, the strength of the links has a random distribution. This strength distribution is assigned using the equation below:

$$\sigma_r(i) = \sigma_l \left[\ln \left(\frac{1}{1 - r(i)} \right) \right]^{1/m} \quad (6.6)$$

where $\sigma_r(i)$ is the strength of the i^{th} link, i is the number of the fiber link and $r(i)$ is a random number between zero and one. 'm' is the Weibull shape factor. This equation assigns a strength value to each link in the fiber, based on the value of the random number used for that link.

6.3.2 Fiber-matrix interface

Interface (or interphase) is the zone of transition separating the matrix from the fiber with thermal, physical and mechanical properties that can be different from that of fiber and matrix. The role of interface is very critical to the performance of the composites. Recent experimental investigations [21, 1, 23] give clear evidence of premature interfacial debonding in metal matrix composites. This emphasizes the need to account for the interfacial behavior of this class of composites. Chandra and Ananth [7] modeled the interface using *spring layer model*. In this model, the interface is considered as a region of negligible thickness possessing the required stiffness and strength. Debonding is postulated to occur under the combined action of normal tensile stress which could cause mode I failure and shear stress which could cause mode II failure at the interface. A quadratic stress based failure theory

$$F(\sigma) \equiv \left(\frac{\sigma_r}{\sigma_r^f} \right)^2 + \left(\frac{\tau}{\tau^f} \right)^2 \geq 1 \quad (6.7)$$

is applied [25, 26] where σ_r^f is the interfacial strength in the normal direction resisting crack opening, and τ^f is the shear strength of the interface. In the above equation the effect of σ_r^f is included only when it is positive. Subsequent to the debonding process, interfacial frictional sliding occurs in the mating debonded surfaces according to Coulomb's law.

6.4 Computational Models

Nonlinear finite element analysis is used to capture local damage in composite lamina. The commercial Finite Element Analysis software MARC [6] is used for this purpose. External subroutines are linked to the main program to model phenomena such as fiber failure and interfacial debonding.

6.4.1 Numerical Implementation of the Weibull Model

The two-parameter Weibull model described in section on statistical model for fiber strength is used for representing the experimentally observed strength distribution of the silicon carbide fiber. The fiber used in the study is considered as being made up of a number of 'links' or divisions. L_o in equation 6.5 is taken as 25 mm and $l = 0.3$ mm. The values for the Weibull parameters used in this case are shown in Table 6.1.

6.4.2 Numerical Implementation of the Monte Carlo Method for modeling fiber breakage

The Monte Carlo simulation procedure to model the process of fiber fracture is shown in the flow chart in Figure 6.1. The finite element model (described in detail in the following section) comprises of five fibers embedded in a matrix. Each fiber is divided into an arbitrary number of links. Initially, a specific strength value, based on equation 6.6, is assigned to each of the links in all the fibers. Next, the finite element model is subjected to a series of increasing displacements. For each load step, the stresses in the fiber and matrix are calculated. The MARC subroutine ELEVAR, linked to this program, extracts the fiber stresses from the solution and these values are compared with the strength of each fiber link through the use of another user-subroutine, HYPELA. If the fiber stress exceeds the assigned link strength, the link breaks. This is simulated by dropping the elastic modulus of the fiber link (element) to a very low value. After each load increment, dummy increments are applied to capture new breaks which may occur due to a re-distribution of stresses. The incremental loading process is continued till a steep drop in the stress-strain curve occurs (as will be shown in the results) indicating the failure of the lamina. At this point, the lamina has little resistance to applied load.

6.4.3 Numerical Modeling of interfacial debonding

The *spring-layer* approach described in the section on fiber-matrix interface is used to study interfacial debonding in 0° and 90° models. Duplicate nodes are created at the interface on fiber and matrix sides. The fiber-matrix bonding is achieved by connecting these duplicate nodes by means of high stiffness springs with a stiffness greater than the elastic modulus of the fiber by a factor of 100. The penetration of matrix elements into the fiber elements is avoided by defining the fiber and matrix phases as deformable contact surfaces. A typical finite element discretization used along with details of the interface element are shown in Fig. 6.2. The stresses at the interface are monitored in this subroutine. Initially a relative motion flag is set to 0. When the interface failure criterion is satisfied then the flag is changed to 1 and the stiffness of the springs is dropped to zero resulting in the separation of the interface nodes. The frictional stresses are neglected in this study.

In the case of 45° lamina model the spring-layer model is not used because once the fiber debonds completely there will be a total separation between the fiber and matrix, thus splitting the composite lamina. This does not correctly capture the actual case where the matrix continues to take the load even after debonding. An alternative approach known as 'matrix layer' approach is used to simulate the stiffness reduction due to interface in the 45° lamina. In this model, fiber elements in the debonded region are assigned matrix properties. The failure criterion used is the same as in the spring layer approach.

6.4.4 Finite Element Models and Boundary Conditions

Longitudinal Model:

A schematic of the 0° lamina is shown in Figure 6.3. The lamina contains 5 fibers (the central fiber has two neighbors on either side) with the inter-fiber spacing determined by the volume fraction (16% or 35%). The length of the lamina is 18 mm which is found sufficiently longer than the load transfer length of this fiber-matrix system. A 4-node, plane-stress element was used for the model. The fiber is elastic, and the random strength distribution of the links is determined by the Weibull equation. A length of about $0.1 L$ (where L is the length of the composite) is made infinitely strong on both the ends to minimize the end-effects. The boundary conditions and loads applied are shown in Figure 6.3. The nodes along the top and the lower edges of the lamina are constrained as shown, to simulate the representative volume element or a repeating unit cell.

The Monte Carlo simulation model described above can not predict the local stresses around in the presence of a fiber break accurately. To examine the effect of stress redistribution due to a broken fiber, a finite element model representing three fibers with the broken fiber in the middle is used. Due to the symmetry only one intact fiber is considered adjacent to the broken fiber as shown in Fig. 6.4. The boundary conditions and applied loads are also shown in the same figure. This model helps in understanding the cause of preferential fractures (if any) in the Monte Carlo simulation model explained in the previous paragraph.

Transverse Model

A schematic of the transverse (90°) loading model is shown in Figure 6.5. Since fiber fracture does not occur at transverse strains of about 3% or less, a simple finite element model capable of simulating interfacial debonding and matrix plasticity was used. The boundary conditions are seen in the schematic. The boundary conditions are also indicated in Figure 6.5. Debonding is modeled using the spring-layer model through the user-subroutine USPRNG.

Shear Model:

The shear behavior of the lamina is studied using a 45° ply model. A schematic of the model is shown in Figure 6.6. The lamina has several fibers oriented at an angle of 45° to the load axis which is the most accurate angle to orient a specimen for shear modulus measurement [28]. The inter-fiber spacing is 260 microns corresponding to a volume fraction of 35%. The boundary conditions are also indicated in Figure 6.6. As discussed earlier, debonding is simulated using the matrix layer model. Debonding and fiber fracture are incorporated through user subroutines.

6.5 Results and Discussion

SCS-6/Ti-15-3 composite is studied as the model system. SCS-6 is a silicon carbide fiber (140 microns diameter) made by Textron Specialty Materials. Matrix is elastic-plastic with linear work hardening. The fiber and matrix properties are given in Table 6.1 (Mital et. al. [29], Gambone [15]).

6.5.1 Longitudinal Behavior

Figure 6.7 (a) shows the stress-strain curves resulting from a simulation conducted for a 35 % volume fraction lamina (curve A) and a 16 % volume fraction lamina (curve B). The elastic portion of curve A ends at point Y, after which the change in slope indicates the onset of matrix plasticity. The first fiber break occurs at a stress value very close to the peak value in the figure. Subsequent breaks occur rapidly within a very small increase in applied strain, causing a steep drop in the stiffness of the lamina. This indicates a catastrophic failure of the lamina. The failure of the lamina immediately after the first break is confirmed from experimental observations by Majumdar [13] and Lerch and Saltsman [32]. Figure 6.7 (b) shows the schematic of the location of fiber breaks that occurred in the 35 % volume fraction case. The breaks are marked by a circle and the numbers indicate the sequence of breaks, signifying the evolution of damage. For the 35 % volume fraction lamina, detailed finite element analyses by Voleti et al. [20] have shown that the stress elevation in the fiber adjacent to a break occurs in the same plane, increasing the probability of a co-planar fracture. This co-planar stress elevation is magnified when plasticity occurs.

Figure 6.8 shows the fracture pattern for the 16 % volume fraction lamina. The fracture

pattern is at an angle to the y-axis (termed as 'inclined fracture' in this work). It may be mentioned that the stochastic distribution of fiber flaws for both the volume fractions are identical. Finite element analysis of the fracture plane for this volume fraction [20] has shown that the peak stress due to fiber fracture occurs at an angle to the fracture plane due to the propagation of the plastic front increasing the probability of a non-coplanar cracking.

In both the cases, a cluster of preferential breaks (co-planar and inclined fracture) caused the failure of the lamina. These results agree with the single ply tensile experiments [13] on Titanium matrix composites having SiC as the reinforcement. Metallurgical examination of the tested specimens showed the presence of local intense slip bands (Figure 7.16 a) in the matrix near a fiber break. The fiber spacing in this case is about 0.7 mm which is equivalent to 16.6% fiber volume fraction. Ultrasonic Shear Back Reflection analysis (Figure 7.16 b) revealed fiber fractures were more correlated occurring in a narrow band. Fiber breaks were predominantly found to occur at locations where the slip bands contact the neighboring fiber. This validates the numerical predictions.

Figure 6.10 shows the results from a simulation where the fiber fractures were *forced* to occur in a pre-determined pattern; co-planar, inclined and random. These load-displacement curves reflect the qualitative behavior of the lamina. The stiffness response of the lamina is distinctly different when the fractures are randomly located in the lamina as compared to the case where the breaks occur preferentially. The co-planar failure shows the weakest lamina response. The lamina failure involving 'inclined' fracture showed marginally better lamina response than the co-planar case; but in the actual simulation little difference was observed, and catastrophic failure resulted soon after the first break. These simulations do not include the effect of residual stresses. It was found from other studies that inclusion of residual stresses caused the initiation of matrix plasticity at a lower strain level while delaying the strain at which the first fiber break occurred. The stress-strain behavior was otherwise similar.

Effect of Interface

To study the role of interface in the propagation of fiber fracture, a 3-fiber model (Figure 6.4) of a composite lamina is examined. The middle fiber in this system was fractured and the stress elevation due to the fracture on the neighboring intact fiber was examined. Debonding reduces the stress concentration near the broken end of the fiber and causes a reduction in the maximum plastic strain. However, debonding in the broken fiber increases the load in the adjacent matrix creating diffused plastic zone as shown in Figure 7.14. The volume fraction used in this case is 35%. The net effect is a reduction in the peak stress in the intact fiber but a greater length of the intact fiber experiences higher stresses (figure 7.15). This reduces the probability of coplanar (0°) fracture. In this study frictional effects in the debonded interface are neglected.

6.5.2 Transverse Behavior

The transverse modulus of the lamina model is shown in Table 6.2, and compared with values derived from theories (Rule of mixtures and Tsai-Halpin equations). The table reflects the undamaged elastic modulus. There is a good match between the Tsai-Halpin and finite element results for the case of strong bond, thus validating the numerical model. The damaged lamina response was computed for two different values of interfacial bond strength, 200 MPa and 1500 MPa, representing weak and strong bonds, respectively. The stress-strain curves for weak and strong interfacial bonds are shown in Figure 6.13.

In the case of higher interfacial bond strength, matrix plasticity initiates much earlier to debonding as seen by the first non-linearity in the curve (Point Y). Debonding occurs subsequently causing a major drop in stress values (Point A to B). The weak bond case shows the characteristic 3-stage behavior seen in the experiments [33]. The first stage (upto Point A') is completely elastic. The second stage is dominated by debonding. Debonding initiates at this point and continues until the total debonding occurs at Point B'. Local plasticity in the matrix is seen at about 0.33% and steadily increases with load. The third stage (after Point B') is completely dominated by the plastic deformation of the matrix.

6.5.3 Shear Behavior

The shear modulus of the lamina evaluated from the model is shown in Table 6.2, and compared with the values derived from two different theories, Rule of mixtures and Tsai-Halpin model. There is a good match between the two values. Figure 6.14 shows the results from the Monte-Carlo simulation. Cases were run for two different interfacial bond strengths of 200 MPa and 1500 MPa. These bond strengths make the fiber debond *before* and *after* matrix becomes plastic, corresponding to weak and strong interfacial bond strengths. Some of the observations are:

- No fiber fracture is observed in the simulations indicating that debonding and matrix plasticity are the only mechanisms invoked.
- In the case of weak bond strength, debonding initiates at a longitudinal strain of 0.24 % and matrix plasticity initiates subsequently.
- For higher bond strength, matrix plasticity initiates at 0.57 % (figure 6.14) and debonding initiates subsequently.
- In both the cases failure of the lamina does not occur even at 2% strain agreeing with the experimental observations [32].

6.5.4 Evaluation of the damage tensor

Each lamina along its material (fiber) direction is assumed to be transversely-isotropic and requires five independent constants (four in the plane of isotropy) to completely describe its elastic behavior. The stiffness tensor for two-dimensional response with damage is given in equation 6.3. In this study the evolution of the Poisson's ratio D_{12} is not considered. D_{11} , D_{22} , D_{66} are derived from longitudinal, transverse and shear tests described earlier. The variation of D_{11} , D_{22} , D_{66} with applied load, models the evolution of damage in each coordinate direction. The stress state at any applied strain can be determined uniquely using equation 6.2 by knowing the evolution of the Damage parameters (or the deterioration of the elastic moduli) and the inelastic strain. This data can be obtained from the numerical predictions. The reduction in the elastic moduli is determined by numerically simulating unloading and reloading experiments at different applied strain levels. The damage parameters in the transverse direction (D_{22}) is shown in in Table 6.3 as a function of the applied strain.

6.6 Summary and Conclusions

A micromechanics based modeling approach is developed to study the local failure mechanisms such as fiber fracture and interfacial debonding in continuous fiber metal-matrix composites. The fiber, matrix and the interface are modeled explicitly. Monte Carlo simulation procedure was used to model the stochastic nature of the fiber failure. The fracture patterns predicted from the simulation of 0° -lamina response matched well with experimental results. The effect of interfacial debonding on the stress elevation in the presence of a fiber fracture is investigated. It is found that debonding results in diffused plastic region in the matrix near the fiber break thereby shifting the location of the peak stress. The evolution of damage under different interfacial conditions is studied using the models. A damage-dependent constitutive tensor is developed for the lamina from the numerical simulations. This approach will help in studying the influence of micromechanical parameters on the evolution of damage in composites not only under static loads but also when subjected to cyclic loading.

Bibliography

- [1] Sierakowski R.L. and Newaz G.M. *Damage tolerance in advanced composites*. Technomic Publishing Co., Inc, 1994.
- [2] Voyiadjis G.Z., Venson A.R., and Kattan P.I. Experimental determination of damage parameters in uniaxially loaded metal-matrix composites using the overall approach. *International Journal of Plasticity*, 11:895-926, 1995.
- [3] Ladeveze P. and LeDantec E. Damage modeling of the elementary ply for laminated composites. *Composites Science and Technology*, 43:257-267, 1992.
- [4] Robertson D.R. and Mall S. Incorporating fiber damage in a micromechanical analysis of metal matrix composites. *Composites Science and Technology*, 43:759-769, 1995.
- [5] J. Aboudi. *Mechanics of Composite Materials-A Unified Micromechanical Approach*. Elsevier, Amsterdam, Netherlands, 1991.
- [6] Lacy T.E., McDowell D.L., P.A. Willice, and Talreja R. On representation of damage evolution in continuum damage mechanics. *International Journal of Damage Mechanics*, 6(1):62-95, 1997.
- [7] Lemaitre J. *A course on damage mechanics*. Springer, 1996.
- [8] Curtin W. A. Exact theory of fibre fragmentation in a single-filament composite. *Journal of Materials Science*, 26(6):5239-5253, 1991.
- [9] Curtin W. A. Determining Fiber Strength vs. Gage Length. *Polymer Composites*, 15(6):474-478, 1994.
- [10] Yuan J., Xia Y., and Yang B. A note on the Monte-Carlo simulation of the tensile deformation and failure process of unidirectional composites. *Composites Science and Technology*, 52:197-204, 1994.
- [11] Oh K.P. A Monte Carlo study of the strength of unidirectional fiber-reinforced composites. *Journal of Composite Materials*, 13:311-328, 1979.
- [12] Engelstad S.P. and Reddy J.N. Probabilistic methods for the analysis of metal-matrix composites. *Composites Science and Technology*, 50:91-107, 1994.

- [13] Voleti S.R., Ananth C.R., and Chandra N. Effect of interfacial properties on fiber fragmentation (in print). *Journal of Composites Technology and Research*, 1997.
- [14] Weibull W. A statistical distribution function of wide applicability. *Journal of Applied Mechanics*, 18:293, 1951.
- [15] Jayatilaka A. *Fracture of engineering brittle materials*. Elsevier, Amsterdam, Netherlands, 1991.
- [16] Feillard P., Desarmot G., and Favre J.F. Theoretical aspects of the fragmentation test. *Composites Science and Technology*, 50:265–279, 1994.
- [17] LaCroix T., Keunnings R., Desager M., and Verpoest I. A new data reduction scheme for the fragmentation testing of polymer composites. *Composites Science and Technology*, 43:379–387, 1992.
- [18] Coleman B.D. On the strength of classical fibers and fiber bundles. *Journal of Mechanics and Physics of Solids*, 7:60, 1958.
- [19] Chou T.W. *Microstructural design of fiber composites*. Cambridge University Press, Cambridge, U.K., 1991.
- [20] S. R. Voleti, C. R. Ananth, and N. Chandra. Evolution of Micro-damage in Metal Matrix Composites. In Atluri S.N. and Yagawa G., editors, *Advances in Computational Engineering Science*, pages 1214–1219. Tech. Science Press, 1997.
- [21] R. P. Nimmer, R. J. Bankert, E. S. Russel, G. A. Smith, and P. K. Wright. Micromechanical Modeling of Fiber-Matrix Interface Effects in Transversely Loaded SiC/Ti-6-4 Metal Matrix Composites. *Journal of Composites Technology and Research*, 13(1):3–13, Spring 1991.
- [22] B. S. Majumdar and G. M. Newaz. Inelastic Deformation of Metal Matrix Composites: Plasticity and Damage Mechanisms. *Philosophical Magazine A*, 66(2):187–212, 1992.
- [23] P. K. Brindley and S. L. Draper. Failure Mechanisms of 0° and 90° SiC/Ti-24Al-11Nb Composites Under Various Loading Conditions. In R. Darolia, J. J. Lewandowski, C. T. Liu, P. L. Martin, D. B. Miracle, and M. V. Nathal, editors, *Structural Intermetallics*, pages 727–737. The Minerals, Metals & Materials Society, 1993.
- [24] N. Chandra and C. R. Ananth. Analysis of Interfacial Behavior in MMCs and IMCs using Thin-slice Push-out Tests. *Composites Science and Technology*, 54(1):87–100, 1995.
- [25] Z. Hashin. Failure Criteria for Unidirectional Fibre Composites. *Journal of Applied Mechanics*, 47:329–334, 1980.
- [26] M. R. Wisnom. Micromechanical Modeling of the Transverse Tensile Ductility of Unidirectional Silicon Carbide/6061 Aluminum. *Journal of Composites Technology and Research*, 14(1):61–69, 1992.

- [27] MARC Analysis Corporation. *MARC Version: K6, User Manuals*, 1995.
- [28] Pindera M.J. and Herakovich C.T. Shear characterization of unidirectional composites with the off-axis tensions test. *Experimental Mechanics*, 58(3):453-464, 1996.
- [29] Gambone M.L. SiC fiber strength after consolidation and heat-treatment in Ti-22Al-23Nb matrix composite. *Scripta Materialia*, 34:507-512, 1996.
- [30] Mital S. K., Caruso J.J., and Chamis C. C. Metal matrix microfracture: Computational Simulation. *Computers and Structures*, 37(2):141-150, 1990.
- [31] Majumdar B.S. Interfaces in metal matrix composites. In Mall S. and Nicholas T., editors, *Titanium matrix composites*. Technomic publications, 1996.
- [32] Lerch B.A. and Saltsman J.F. Tensile deformation damage in SiC/Ti-15-3 laminates. Technical Report NASA TM 103620, NASA, 1991.
- [33] B. S. Majumdar and G. M. Newaz. Inelastic Deformation of Metal Matrix Composites: Plasticity and Damage Mechanisms. *Philosophical Magazine A*, 66(2):187-212, 1992.

	Material Properties	Weibull Properties
Fiber	E = 428 GPa, $\nu = 0.3$, CTE = 3.56 E-06 /°C	$\sigma_0 = 4510$ MPa, m = 10.4
Matrix	E = 85 GPa, $\nu = 0.32$, Yield = 760 MPa, CTE = 7.812 E-06 /°C Work Hardening = 3.2 E3 MPa	

Table 6.1: Material properties of the fiber and matrix

	Theoretical Model	FEM Model
0 degree lamina (longit. modulus)	205 GPa (Rule of. Mix)	205 GPa
90 degree lamina (transverse modulus)	149.0 GPa Tsai-Halpin 118.1 GPa Rule of Mix.	155 GPa
45 degree lamina (shear modulus)	44.81GPa Rule of Mix. 52.0 GPa Tsai-Halpin	45.35 GPa

Table 6.2: Elastic modulli calculated from FEM and theoretical solutions

Applied Strain	Transverse Modulus GPa	D ₂₂	Inelastic Strain
2.8E-4	156.21	0.0	0.0
2.47E-3	50.80	0.675	0.0
8.19E-3	44.28	0.72	6.85E-4
1.08E-2	44.27	0.72	2.46E-3

Table 6.3: Material behavior changes due to damage and plasticity

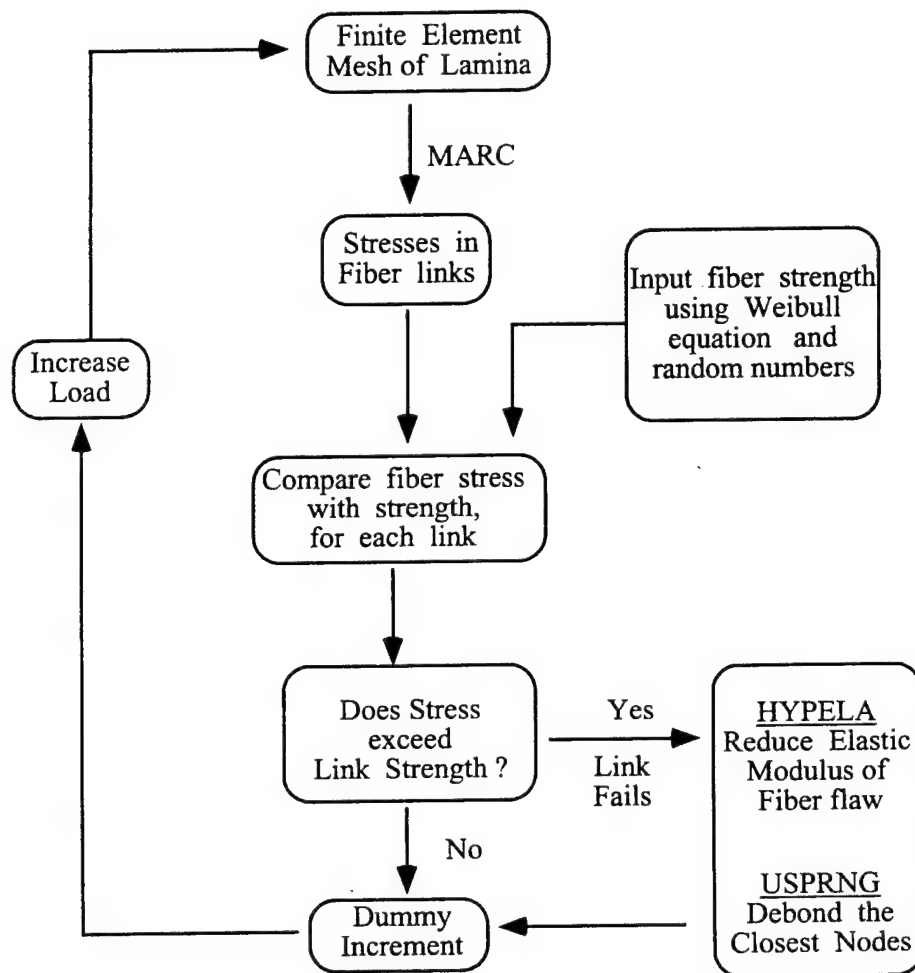
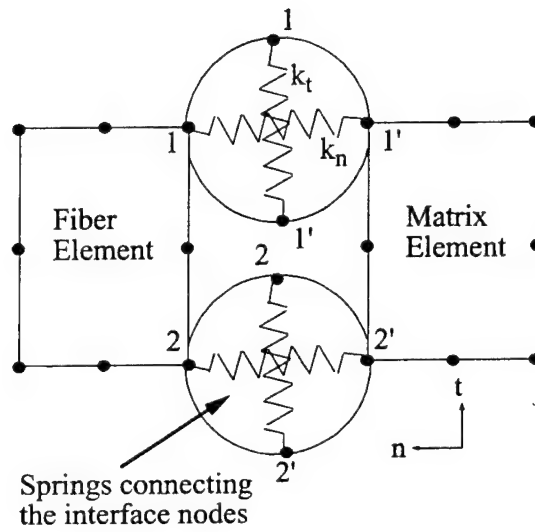


Figure 6.1: Flow-chart of the Monte Carlo simulation



1-1', 2-2'	duplicate nodes (with the same co-ordinates) at the interface
1-2, 1'-2'	Contact edges which cannot penetrate
n, t	normal and tangential directions
k_n, k_t	Stiffness of springs in normal and tangential directions

Figure 6.2: Spring-layer model for fiber-matrix interface

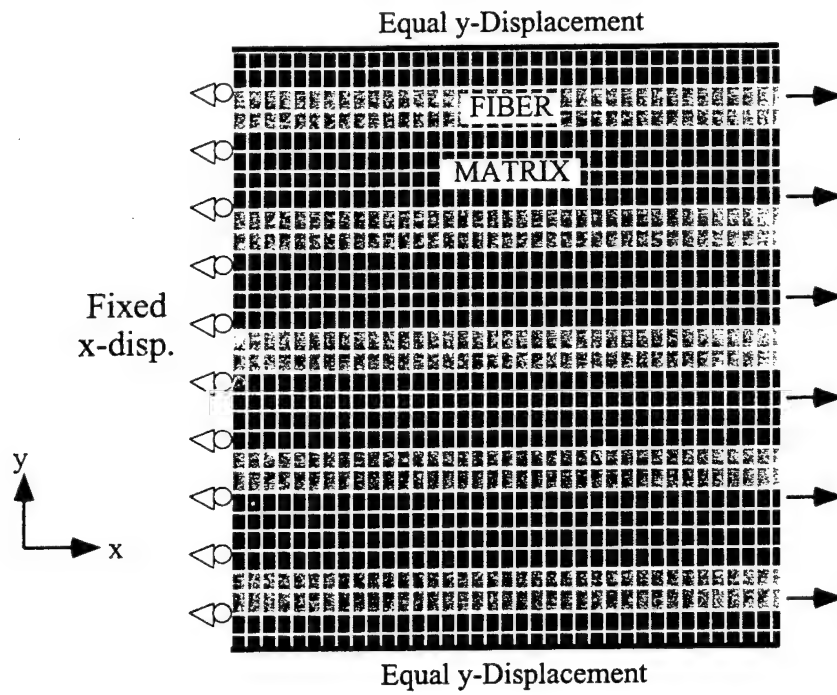


Figure 6.3: Schematic of the 0° lamina and boundary conditions

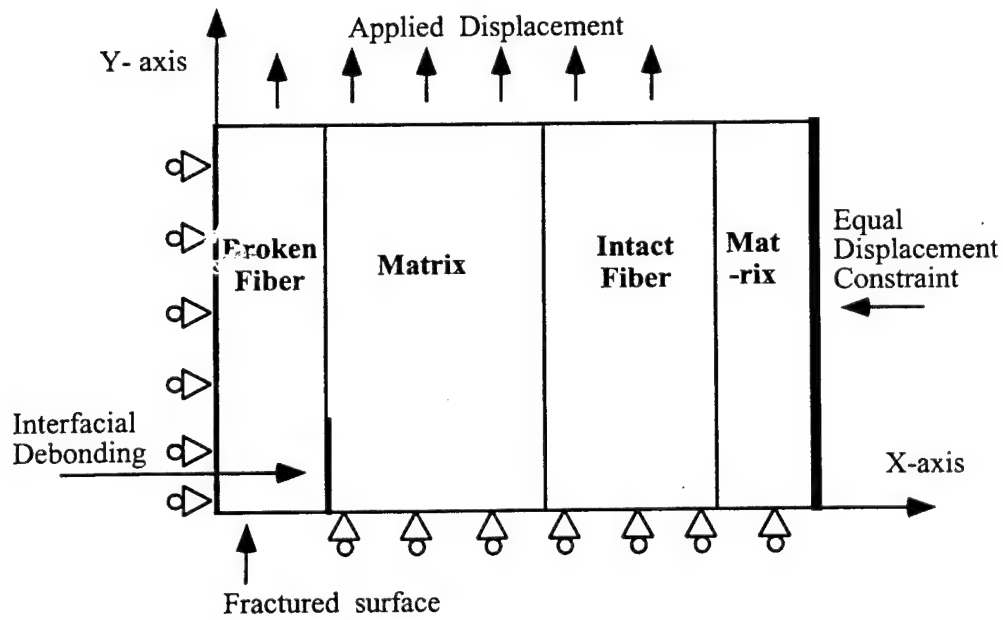


Figure 6.4: Schematic of the 3-fiber model and boundary conditions

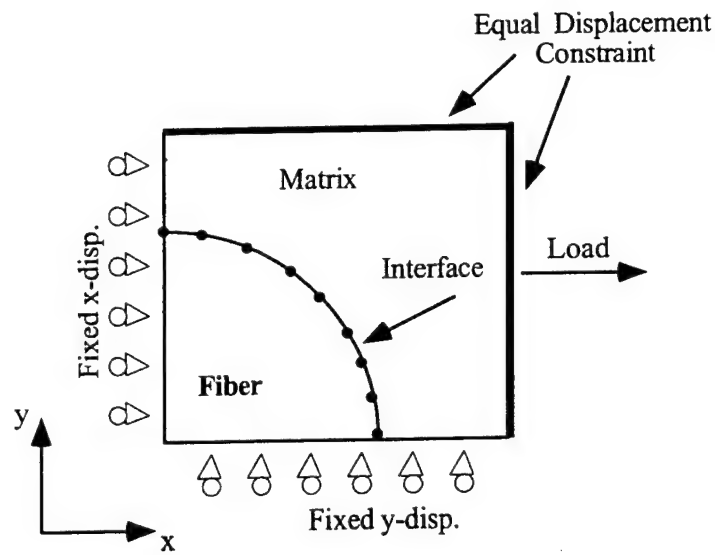


Figure 6.5: Schematic and boundary conditions of the finite element model to study transverse behavior

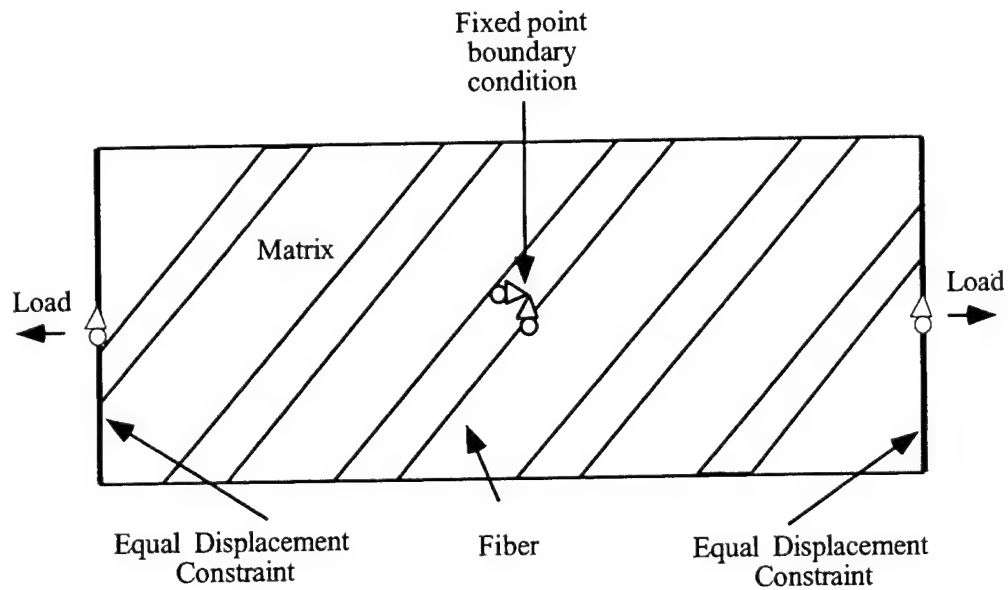
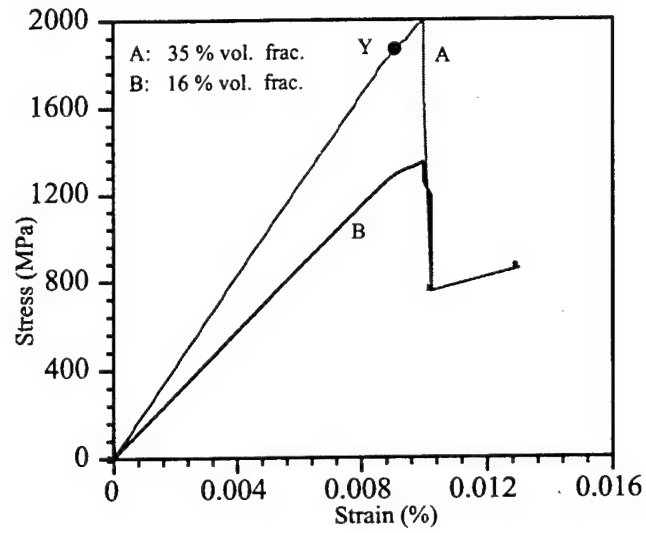
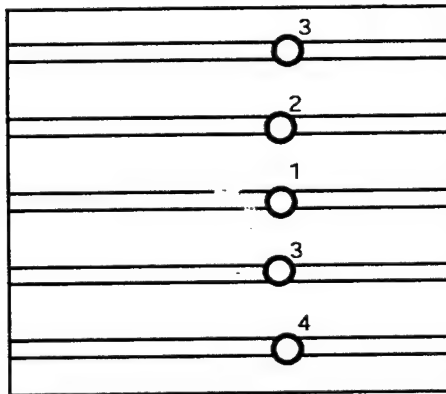


Figure 6.6: Schematic diagram of the loading and boundary conditions of the 45° ply model



(a)



(b)

Figure 6.7: (a) Stress-strain curves for 0° degree laminae, (b) fracture pattern for a 35 % volume fraction lamina

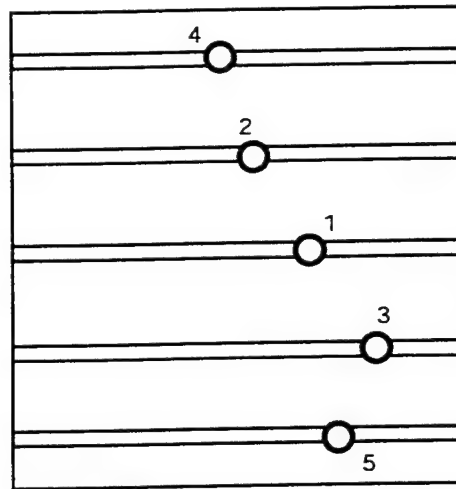


Figure 6.8: Fracture pattern for a 16 % fiber volume fraction lamina

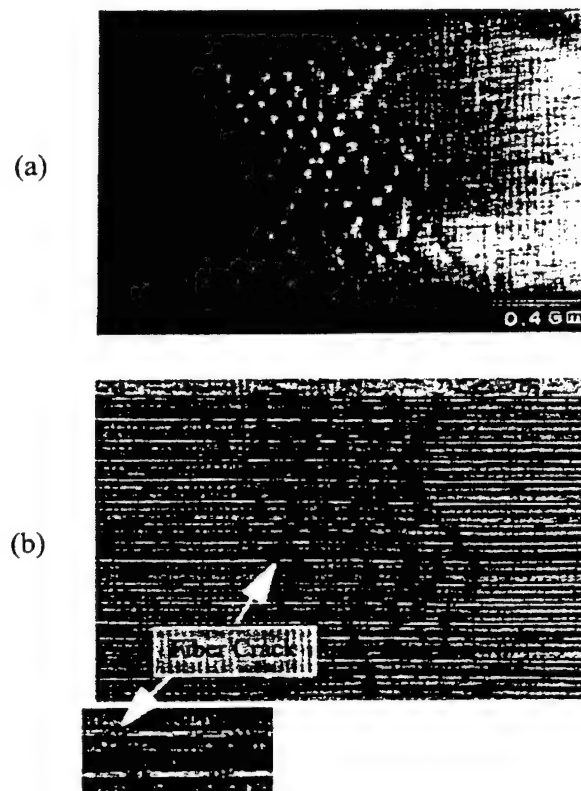


Figure 6.9: Experimental results

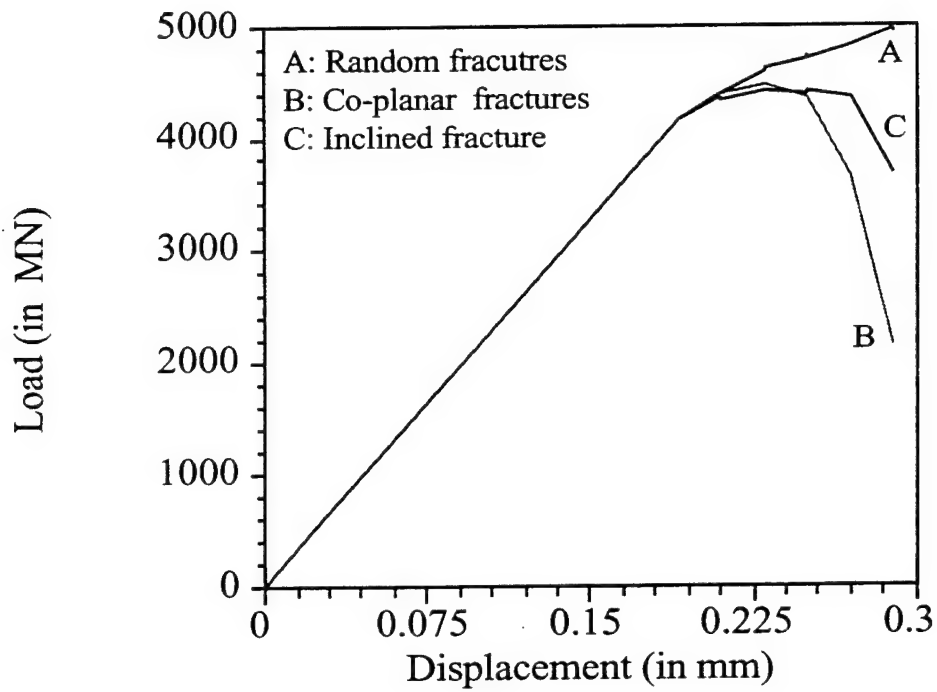


Figure 6.10: Load-displacement curves for pre-determined damage patterns

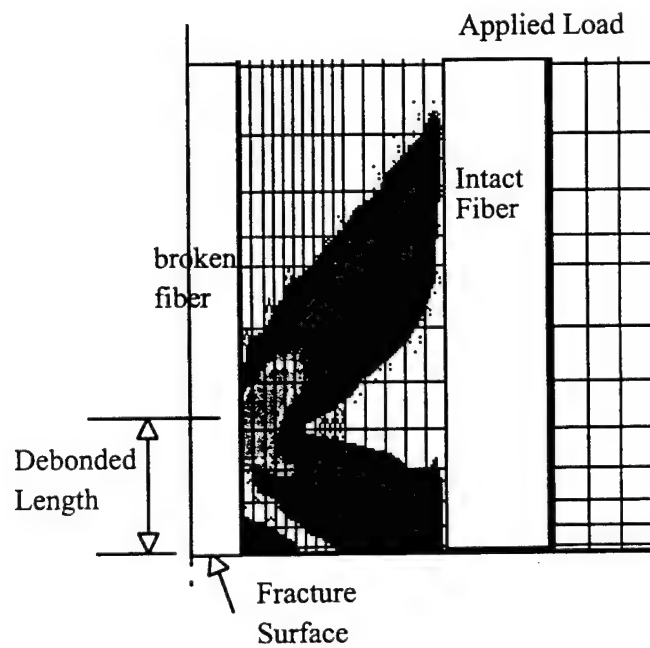


Figure 6.11: Propagation of plastic front in the case of broken fiber with debonding

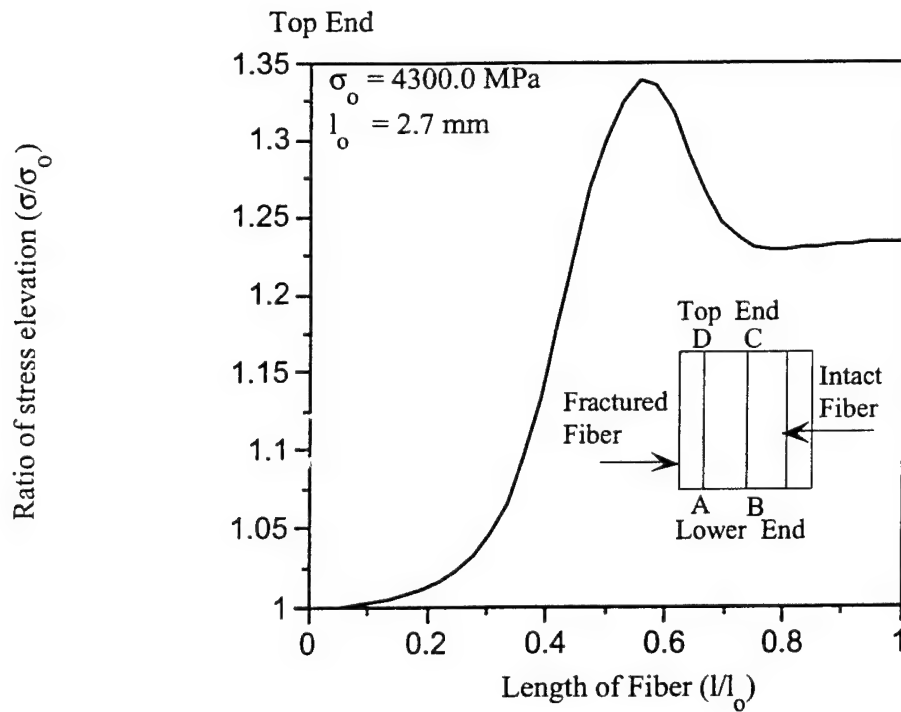


Figure 6.12: Variation of axial stress in the intact fiber upon debonding of the broken fiber

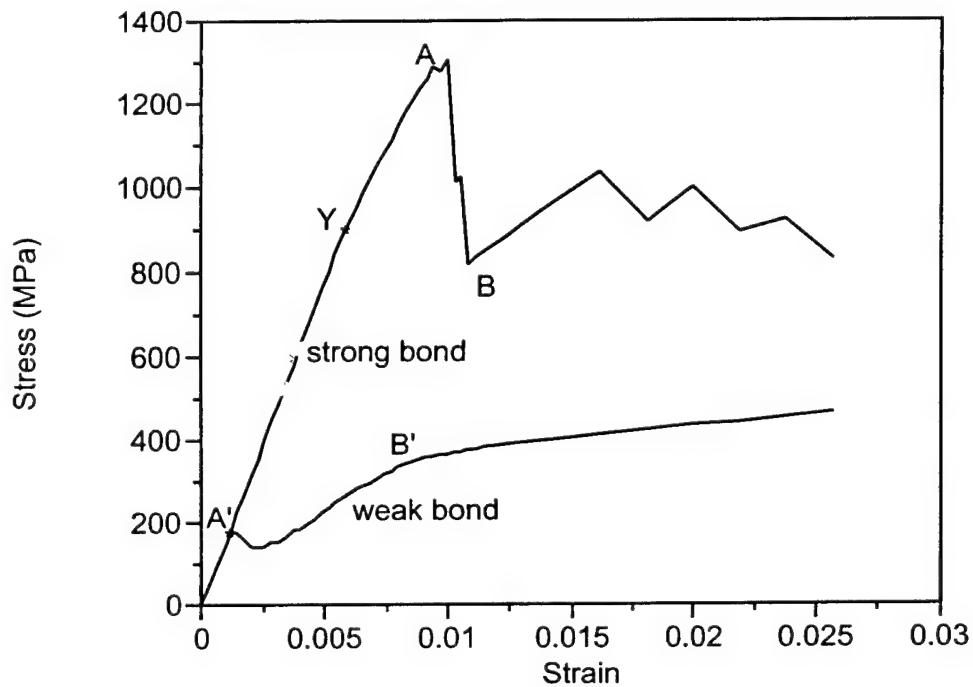


Figure 6.13: Stress-strain curve for a weakly-bonded, transversely-loaded composite .

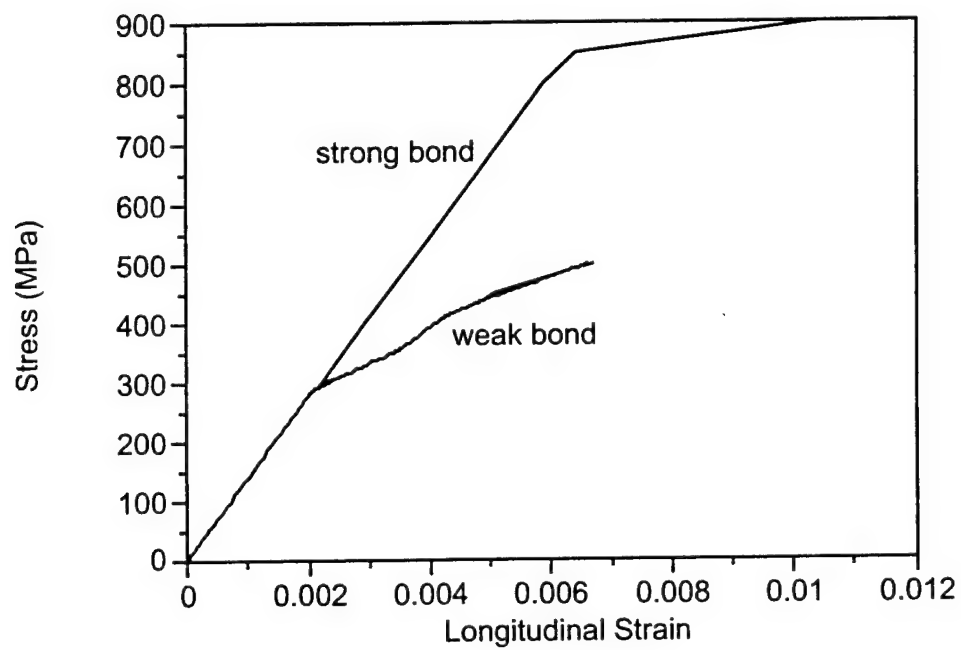


Figure 6.14: Stress vs. longitudinal strain for 45°-lamina

Chapter 7

Effect of Fiber Fracture and Matrix Yielding on Load Sharing in Continuous Fiber Metal Matrix Composites

7.1 Introduction

The tensile response of a composite lamina is governed by the strength of the fiber and the load transfer properties of the matrix. In continuous fiber composites, individual fibers can fail well before the ultimate failure of the composite. Any fiber break causes a re-distribution of load [1], to other fibers causing stress elevation on the adjacent fibers. This results in a non-uniform stress distribution along the length of those fibers. The strength of the fiber also varies randomly across its length due to the stochastic failure behavior of the brittle fibers. Under these conditions, the fiber break occurs not necessarily at the weakest link, but where the stress exceeds the local strength of the fiber.

The effect of an isolated fiber break on the occurrence of subsequent breaks, and their effect on the stiffness of the composite are important issues. Different rules for load sharing have been proposed in this context, such as equal (or global) load sharing [2] and local load sharing [3]. The prevalence of one over the other is determined by various factors including the fiber and matrix properties and fiber volume fraction. In the case of local load sharing, the stress elevation in the neighboring fibers caused by load re-distribution could be sufficient to create preferential fiber fractures or coordinated fractures (such as coplanar or angled), leading to premature failure of the composite. Thus, a study of the load re-distribution is critical to the evaluation of the tensile properties of a lamina.

The problem of load transfer in composites has been studied using shear-lag theory by Rosen [2] and others [4, 5, 6]. Most of these analyses are developed for Polymer Matrix

Composites (PMC) where the assumptions of shear-lag theory are valid. Metal Matrix Composite (MMC) which is the focus of the present study significantly differs from the PMC's in that the behavior of fiber, matrix and interface is quite different. There are issues such as interfacial debonding [7], processing induced residual stresses [8] and the inelastic deformation of the matrix [1] that are specific to MMCs. Nicholas et al. [10] studied the problem of strain accumulation from fiber breaks in MMCs during in-phase thermomechanical fatigue. Iremonger et. al. [11] performed simplified computational analysis of the problem. He et. al. [12] used linear elastic model to study the stress elevation in the next, and the next-to-next fibers in the presence of a broken fiber. Probabilistic arguments were then used to determine whether global load sharing or local load sharing would occur in those composites. But the effect of local plasticity and debond length on the stress redistribution were not addressed in that study. Majumdar et. al. [13] performed 0° tensile tests on a SiC/Ti-6-4 lamina to study the effect of fiber breakage and matrix plasticity on the fracture behavior of the lamina. Their experimental results showed the presence of extensive slip band formation due to fiber breaks. The impingement of those slip bands on adjacent fibers caused the latter to fail at the location of impingement. The presence of slip bands indicate that plasticity might have a significant effect on local load sharing in the case of MMCs. The objective of the present study is to examine the role of matrix plasticity and interfacial debonding on the global/local load sharing characteristics of MMCs.

7.2 Computational Model

A 3-fiber unit cell is selected to study the stress elevation in the adjacent fiber in the presence of a broken fiber in the middle. Due to symmetry only one half of the unit cell is considered as shown in Figure 7.1. 8-noded plane stress quadrilateral elements are used with boundary conditions as shown in Figure 7.1. Plane stress assumption represents the closest 2-D approximation of the thin section with layers of fibers and matrix (as shown in the figure). MARC [6], a non-linear finite element code, is used to perform the numerical simulations. Duplicate nodes are created along the fiber-matrix interface and are connected using high stiffness springs to create a bonded interface. Debonding is simulated by reducing the spring constant to a very low value. Contact-friction algorithm inherent in the software is used to model the post-debonding friction and also to prevent the penetration of nodes at the contact surface. This model has been successfully used in a number of micromechanical studies of interfacial debonding [7]. Nodal displacements are applied to the top edge of the model to simulate the application of uniform uniaxial strain.

7.3 Results and Discussion

The three-fiber unit cell model is used to study the effect of stress redistribution due to a fiber break on the adjacent fiber. SiC/Ti-15-3 MMC system is considered in this study. The fiber and matrix properties are shown in Table 1 [15]. The fiber diameter is 140 microns.

Fiber spacing is computed based on the load carrying capacity, thus the area ratio of the fiber to total (fiber+matrix) represents the fiber volume fraction. If s is the distance between the edges of the two fibers and d_f is the diameter of the fiber, i.e, the volume fraction $v_f = \frac{d_f}{d_f+s}$. Fiber-matrix interface is perfectly bonded prior to the propagation of fracture along the interface. Two types of constitutive models are considered for the matrix material: (i) linear elastic (ii) elastic-perfectly plastic. First the results from purely elastic stress analysis are discussed followed by a section devoted to elastic-plastic behavior.

7.3.1 Effect of Fiber Fracture: Elastic Analysis

Fiber fracture causes redistribution of stresses in the vicinity of the break resulting in a localized zone of high stresses in the neighboring fibers. This is primarily due to the loss in the load-carrying ability near the broken end of the fiber. This is evident from the results from Figure 7.2 which show a drop in the axial stress along the length of the broken fiber. It can be seen from this figure that the axial stress drops from the far field value to almost zero at the broken end. The neighboring fibers have to take the extra load due to the fiber break. Results from the three-fiber model also indicate that the peak stress along the *fiber* axis (Figure 7.3) in the intact fiber shows a 11% increase when compared to the far-field fiber axial stress σ_o which is the same in the broken as well as the intact fiber. In order to determine the effect of the broken fiber on the second neighbor, the analysis was conducted using a separate model with two neighboring fibers. It was found that the stress elevation on the second neighbor was less than 1% for a fiber volume fraction of 35%. These effects are expected to decrease further for lower volume fractions. Hence, the 3-fiber (or one neighbor) model is chosen in all the cases considered in this study. *It has to be noted that the stress elevation from the above analyses are much lower than that predicted by the shear-lag theory [1], which neglects the axial stresses in the matrix.* With decrease in the stiffness of the matrix, the peak stress in the intact fiber increases to reach the levels predicted by the shear-lag analysis, consistent with the assumptions in the theory.

The stress elevation in the neighboring fibers is also caused by the stress concentration effects at the crack tip and due to bending of the neighboring fiber. Fiber fracture causes stress concentration at the edge of the fractured surface. The variation of the axial stresses along the fracture plane is shown in Figure 7.4. It can be seen that the stress is maximum near the crack tip and drops rapidly with increasing distance away from the broken end. To capture the effects of the stress singularity adequately the crack tip was modeled using singular elements (collapsed 8-noded quadrilaterals with quarter point elements). Comparison of the results indicated that though the stresses at the broken end of the fiber increases sharply with the use of singular elements, the stresses in the neighboring fiber show negligible change (for fiber volume fraction of 35%). Based on this analysis it can be concluded that for the fiber spacing under consideration special singular elements are not needed to study the stress concentration effects on adjacent fibers, and hence not used subsequently.

Fiber bending is caused by the shear strain gradients due to the relative displacement between the broken and the intact fiber in the loading direction. Figure 7.5 shows the

variation of the x-displacements of the intact fiber along its axis. As can be seen, the x-displacement is maximum along the fracture plane resulting in a maximum bending stress at location B. This also accounts for the non-uniformity of the axial stresses in this fiber along the x-axis (Figure 7.6) with the peak on the left edge where the bending stresses are tensile. It is clear from the above that the peak stress in the intact fiber is the net effect of the above local mechanisms. In this analysis a debonding of the order of $0.1 r_f$ is always assumed to be present at the interface around the broken fiber, to relieve the high levels of shear stresses present at the crack tip.

7.3.2 Effect of Matrix Plasticity

Inelastic behavior of the matrix affects the stress redistribution due to a fiber break in many ways. Local plastic deformation near the fiber break creates a crack shielding effect that minimizes the effect of stress concentration and also avoids matrix cracking. Though fiber fracture may occur arising from a stochastic distribution of strength, in general, some fibers may have very high strength leading to matrix yielding prior to any fiber breakage. However, when a fiber break occurs in the early loading stages, local plasticity occurs much before bulk matrix yielding. With increase in the applied strain the plastic front grows at an angle towards the adjacent fiber. Figure 7.7 shows the propagation of plastic strains for the case of 35% volume fraction. With the initiation of plasticity the ratio of peak stress in the intact fiber to the far field stress (the stress elevation ratio, q) increases and deviates from the elastic case where it has a constant low value independent of the applied strain (Figure 7.8). This is anticipated since the plastic regions cannot take any additional load, increasing the load on the fiber. It can also be seen from Figure 7.7 and 7.8 that as the plastic front approaches the intact fiber (applied strains of $> 0.6\%$) there is a significant increase in ' q '. At strain levels of 1% global plasticity sets in and ' q ' does not increase any further. It should be noted that the stress elevation in this case is much higher (maximum value of the order of 50%) when compared to 11% (see Figure 7.8) in the elastic case.

Figure 7.9 shows the variation of the plastic deformation of the matrix along the length of the specimen after the plastic front has reached the intact fiber. It can be seen that for this volume fraction, though the plastic front propagates at an angle, the equivalent plastic strain near the interface of the intact fiber along the fracture plane (A-B in the figure) is almost 75% of the peak value which occurs at a distance above the lower end (B). This is very much different from the case of 16% volume fraction to be discussed in the next section. This is because at this high volume fraction the fibers are close enough that by the time the plastic front reach the neighboring intact fiber, plasticity has initiated in the whole region between the two fibers up to the fracture plane (Figure 7.7). Under this condition ' q ' is found to be maximum at B making it the location which is the most probable to fail next (Figure 7.10).

Figure 7.11 shows the peak stress along the intact fiber for a fiber volume fraction of 16%. Figure shows that the peak stress for this case occurs at an angle of about 45° from the fracture plane. This can be explained from the propagation of the plastic front shown in

Figure 7.12. As in the case of 35% volume fraction, the plastic front grows at an angle to the fracture plane and reaches the intact fiber. It can be seen that at this stage the matrix in the vicinity of the intact fiber along the fracture plane shows negligible plastic strain which is very much different from the 35% case. This is also clear from the variation of plastic strain shown in Figure 7.13. Moreover at this low volume fraction levels the effect of stress concentration due to the fiber break on the adjacent fiber is also considerably reduced. This makes matrix plasticity as the predominant factor in causing the stress elevation.

7.3.3 Effect of Interfacial Debonding

Interfacial debonding followed by a fiber break modifies the local stress state. Debonding reduces the stress concentration near the broken end of the fiber and causes a reduction in the maximum plastic strain. However, debonding in the broken fiber increases the load in the adjacent matrix creating a diffused plastic zone as shown in Figure 7.14. A debonded length of $0.3 l_0$ is used in this case. The net effect is a reduction in the peak stress in the intact fiber while a greater length of the intact fiber is subjected to higher stresses (Figure 7.15). This reduces the probability of coplanar (0°) fracture. In this study frictional effects in the debonded zone are neglected.

7.3.4 Experimental Comparisons

Majumdar et. al. [13, 16] conducted single ply tensile experiments on titanium matrix composites having SiC as the reinforcement. Metallurgical examination of the tested specimens showed the presence of local intense slip bands (Figure 7.16 a) in the matrix near a fiber break. The fiber spacing in this case is about 0.7 mm which is equivalent to 16.6% fiber volume fraction. Ultrasonic Shear Back Reflection analysis (Figure 7.16 b) revealed correlated fiber fractures occurred in a narrow band. Fiber breaks were predominantly found to occur at locations where the slip bands contact the neighboring fiber. This validates the numerical predictions. This also clearly indicates the prevalence of local load sharing compared to global load sharing behavior (where the fiber fractures are expected to occur randomly).

7.3.5 Summary and Conclusions

The stress elevation on the adjacent fiber in the presence of a broken fiber in a MMC lamina subjected to longitudinal tension was examined using micromechanical models. The role of various local mechanisms such as the crack tip stress concentration effect, interfacial debonding due to the fiber break were studied for the case of a ductile matrix. The stress elevation was found to be due to the net effect of all these mechanisms. At lower volume fractions the stress concentration in the vicinity of the crack tip (due to the fiber break) was found to have minimum effect on the stress elevation in the adjacent fiber. However it

initiates local matrix plasticity which propagates towards the adjacent fiber much earlier to the occurrence of global matrix plasticity. This results in a significant increase in the stress elevation in that region. At higher volume fractions the probability of coplanar fracture was found to increase. Interfacial debonding was able to decrease the magnitude of stress elevation and also decreased the probability of coplanar breaks which cause catastrophic failure of the composite. The results from this study strongly favor the existence of local load sharing in MMCs at higher volume fractions.

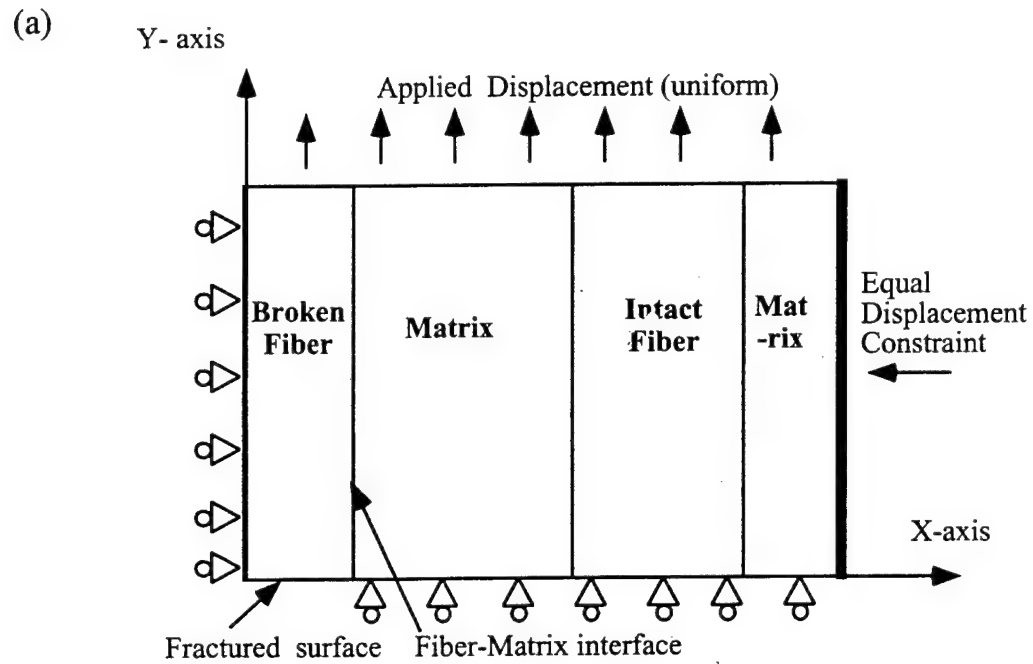
Bibliography

- [1] Chou T.W. *Microstructural design of fiber composites*. Cambridge University Press, Cambridge, U.K., 1991.
- [2] Rosen B.W. Tensile failure of fibrous composites. *AIAA Journal*, 2(11):1985-1991, 1968.
- [3] Zweben C. Tensile failure of fiber composites. *AIAA Journal*, 6:2325, 1968.
- [4] Z. Gao, K.L. Reifsnider, and G. Carman. Strength Prediction and Optimization of Composites with Statistical Fiber Flaw Distributions. *Journal of Composite Materials*, 26:1678-1705, 1992.
- [5] K. Goda and H. Fukunaga. Evaluation of the tensile strength of fiber-reinforced metal matrix composites by Monte-Carlo simulation. In *Proceedings of Second Int. Conf. on Computational Stochastic Mechanics*, pages 307-313, 1995.
- [6] Liangbo D. and Fuqun F. Statistical analysis of failure of unidirectionally fibre-reinforced composites with local load-sharing. *International Journal of Fracture*, 59(1):69-81, 1993.
- [7] N. Chandra and C. R. Ananth. Analysis of Interfacial Behavior in MMCs and IMCs using Thin-slice Push-out Tests. *Composites Science and Technology*, 54(1):87-100, 1995.
- [8] N. Chandra, C. R. Ananth, and H. Garmestani. Micromechanical Modeling of Process Induced Residual Stresses in Ti-24Al-11Nb/SCS-6 Composite. *Journal of Composites Technology and Research*, 16(1):37-46, 1994.
- [9] B. S. Majumdar and G. M. Newaz. Inelastic Deformation of Metal Matrix Composites: Plasticity and Damage Mechanisms. *Philosophical Magazine A*, 66(2):187-212, 1992.
- [10] Nicholas T. and Ahmad J. Modeling fiber breakage in a metal-matrix composite. *Composites Science and Technology*, 52:29-38, 1994.
- [11] Iremongor, M. J. and Wood, W. G. . *Journal of Strain Analysis*, 5:212-222, 1970.
- [12] He M.Y., Evans A.G., and Curtin W.A. The ultimate tensile strength of metal and ceramic-matrix interfaces. *Acta Metallurgica et Materialia*, 41(3):871-878, 1993.

- [13] Majumdar B.S. Interfaces in metal matrix composites. In Mall S. and Nicholas T., editors, *Titanium matrix composites*, pages 113–168. Technomic publications, 1997.
- [14] MARC Analysis Corporation, Palo Alto, CA, 94306, USA. *MARC Version: K6, User Manuals*, 1995.
- [15] Mital S. K., Caruso J.J., and Chamis C. C. Metal matrix microfracture: Computational Simulation. *Computers and Structures*, 37(2):141–150, 1990.
- [16] B. S. Majumdar, T.E. Matikas, and D. B. Miracle. Experiments and Analysis of Fiber Fragmentation in Single and Multiple Fiber SiC/Ti-6Al-4V MMCs. *Composites*, 29, (2), 131-139, 1998.

	Elastic Modulus	Poisson Ratio	Yield Stress
Fiber (SCS-6)	428 GPa	0.3	—
Matrix (Ti-15-3)	85 GPa	0.32	760 MPa

Table 7.1: Material properties of fiber and matrix



(b)

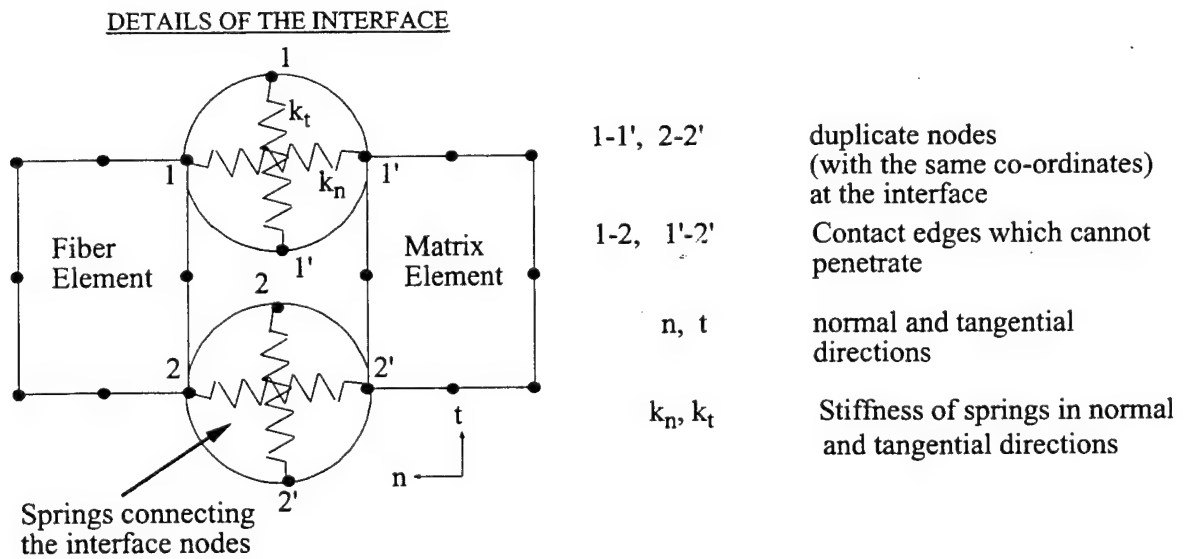


Figure 7.1: Finite element model with boundary conditions

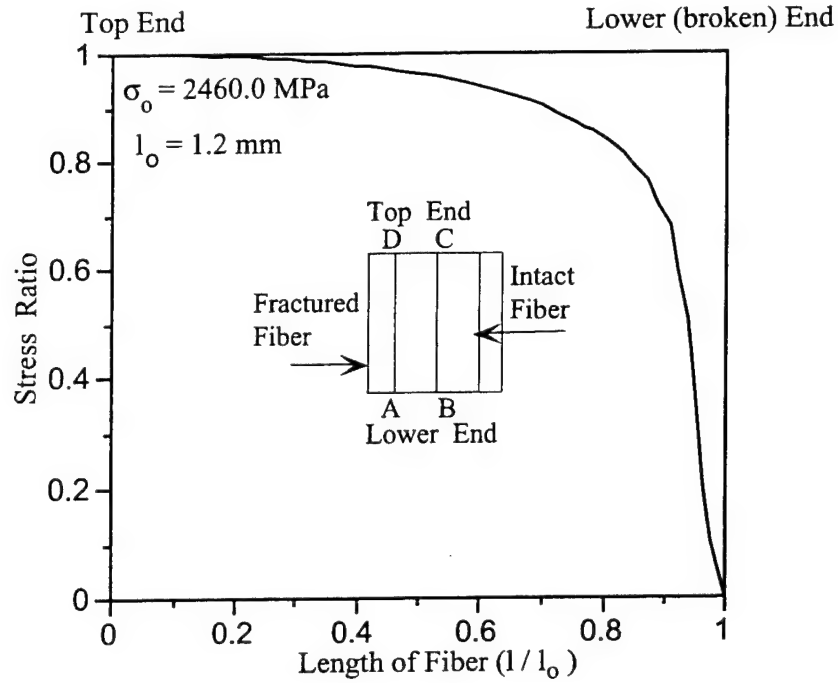


Figure 7.2: axial elastic broken

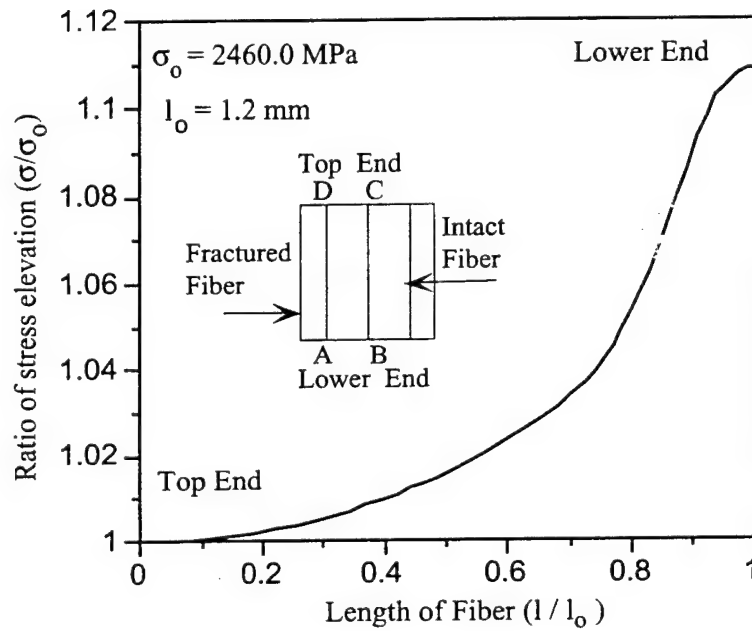


Figure 7.3: axial elastic y

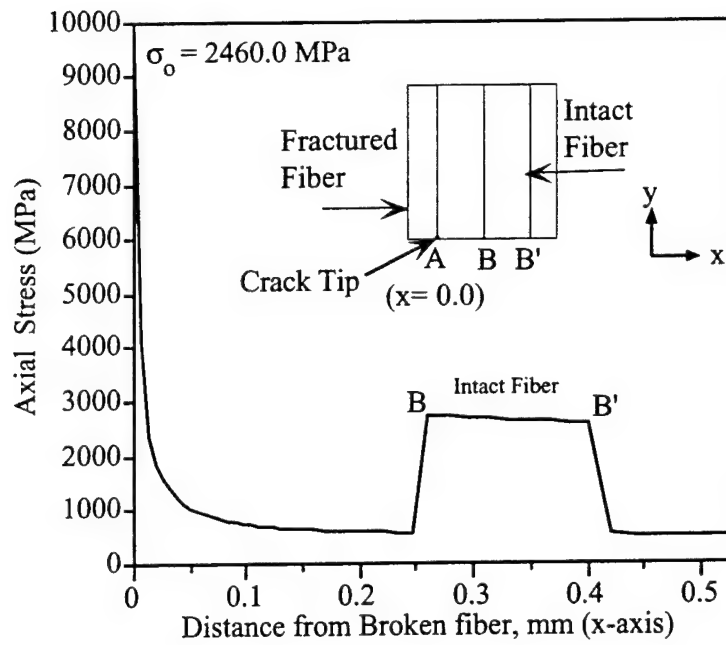


Figure 7.4: axial elastic x

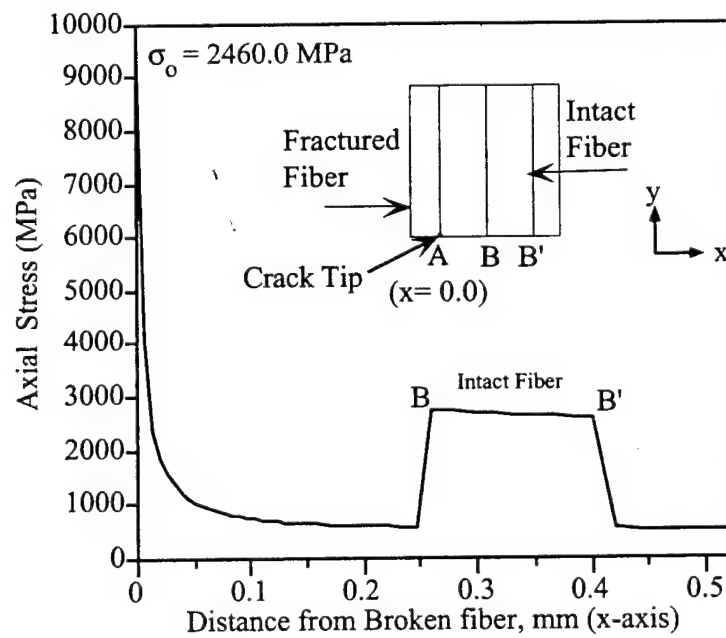


Figure 7.5: x disp bending

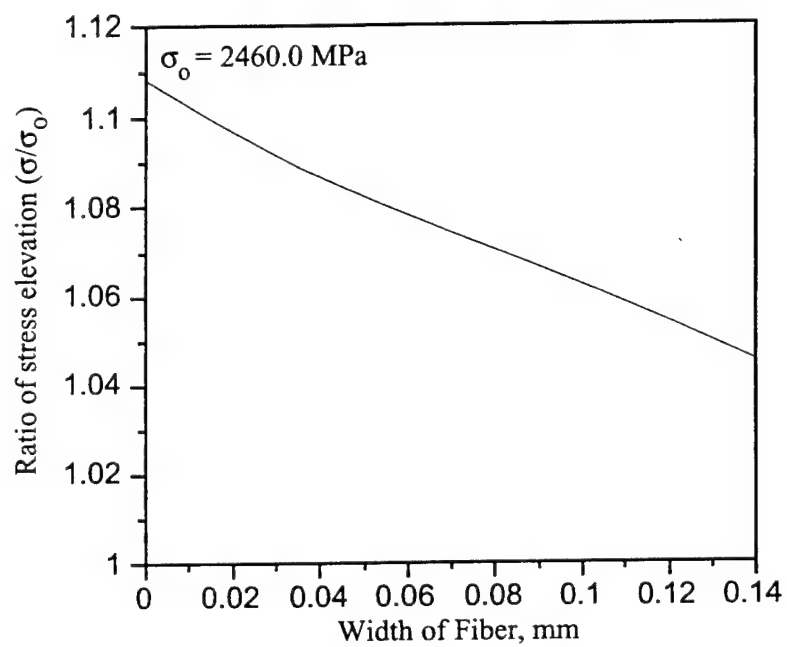


Figure 7.6: nonuniform stress bending

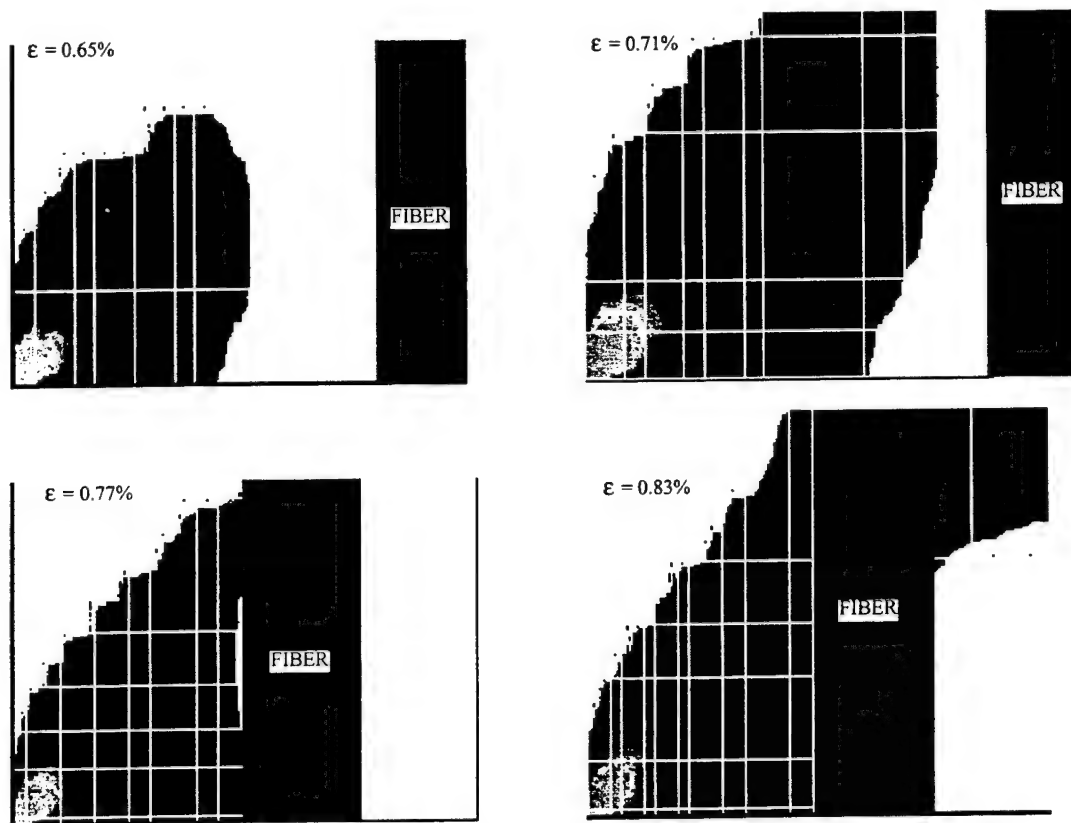


Figure 7.7: propagation vf 35

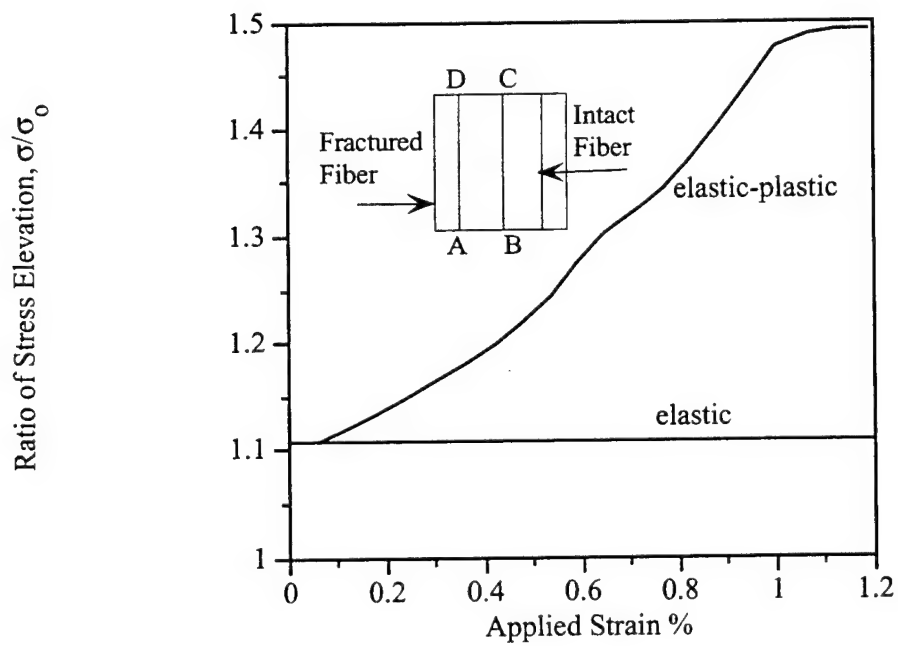


Figure 7.8: P-delta vf 35

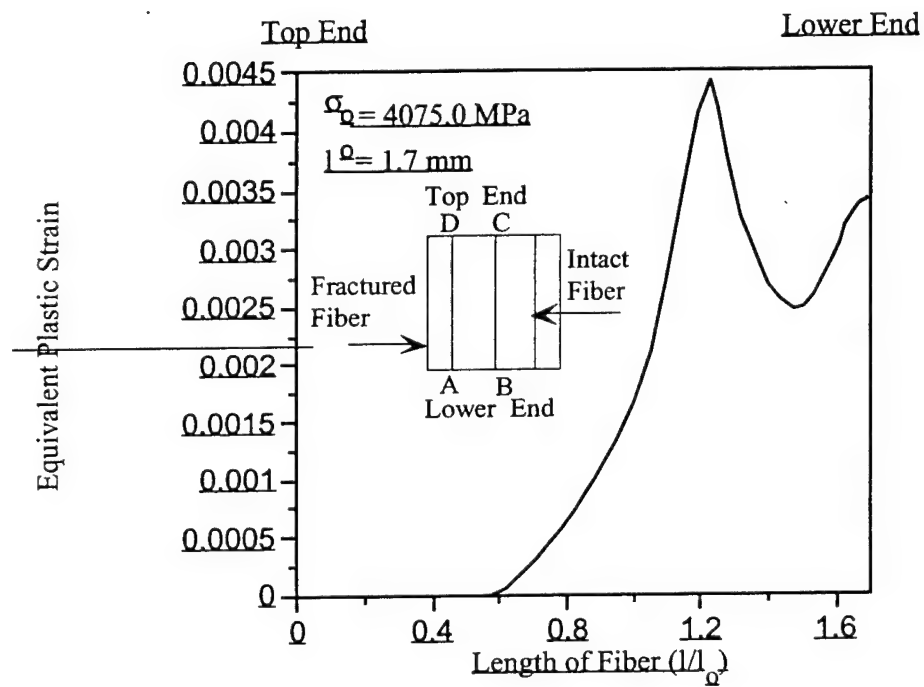


Figure 7.9: variation pl str fiber length vf 35

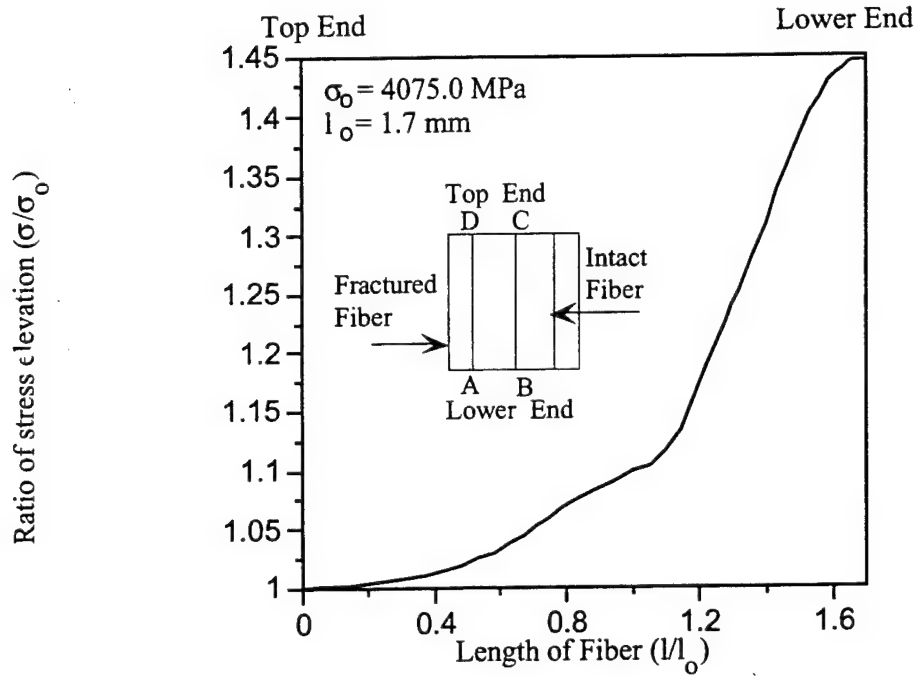


Figure 7.10: variation stress fiber length vf 35

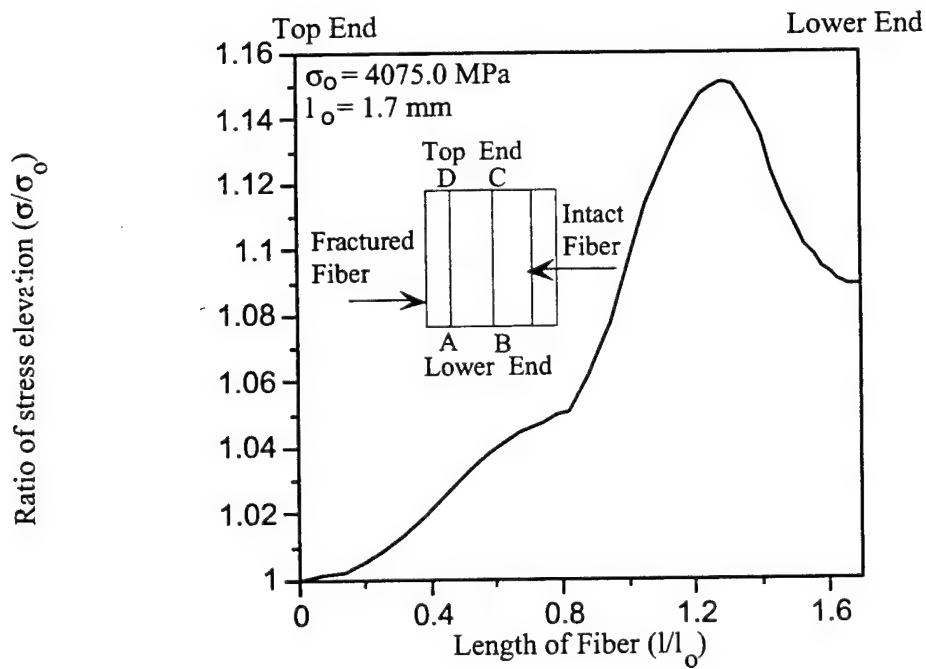


Figure 7.11: variation stress fiber length vf 16

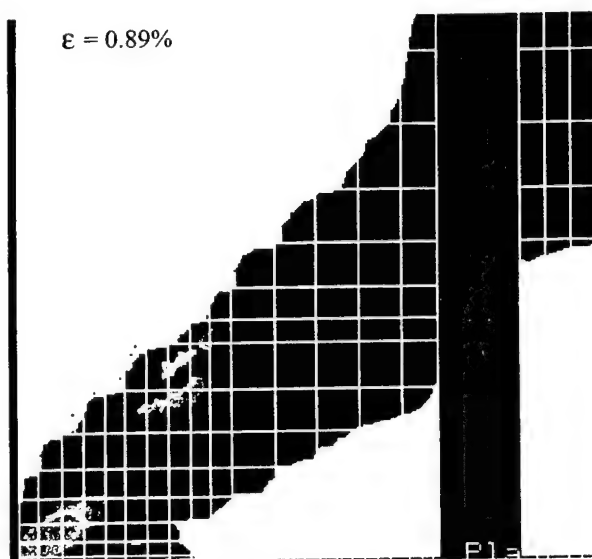
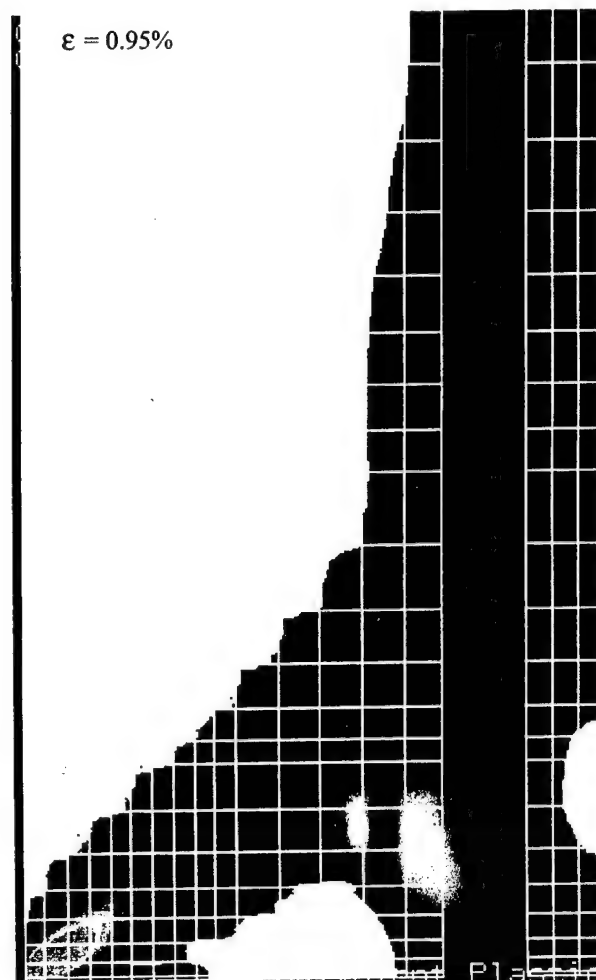
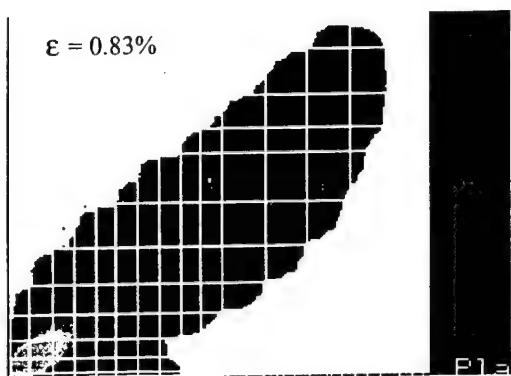


Figure 7.12: propagation vf 16

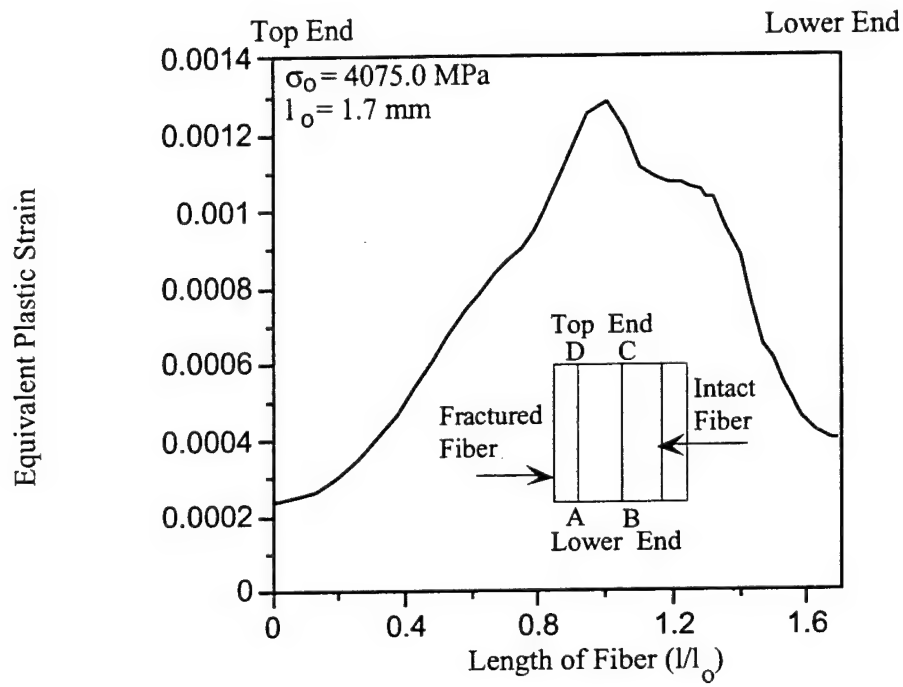


Figure 7.13: variation pl str fiber length vf 16

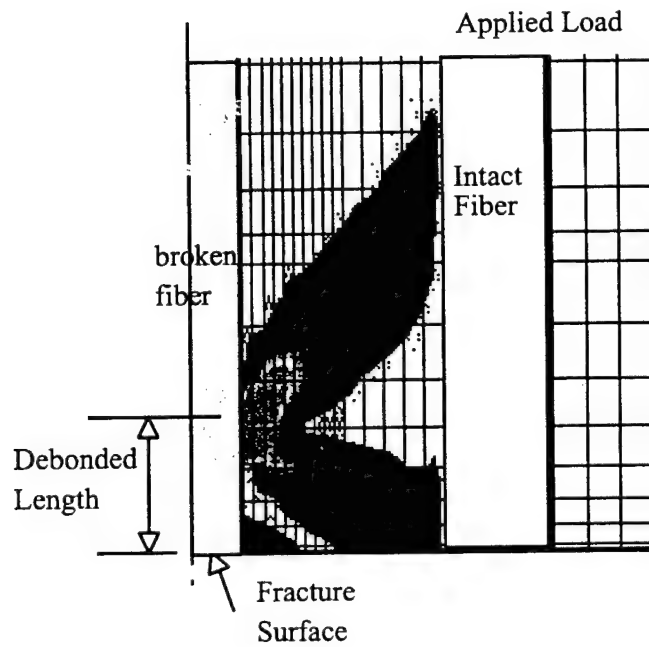


Figure 7.14: plasticity with debonding

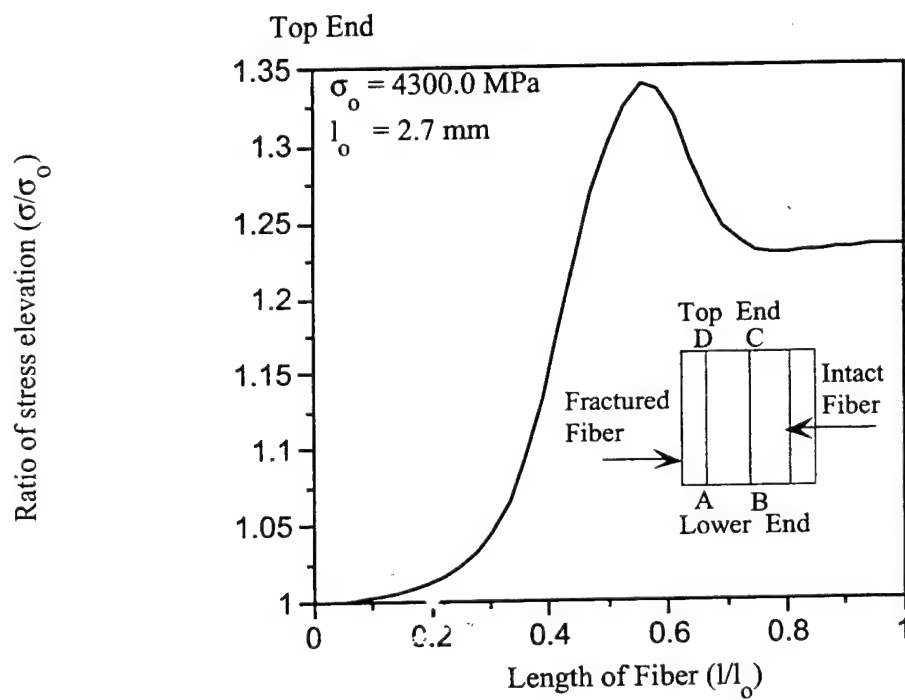
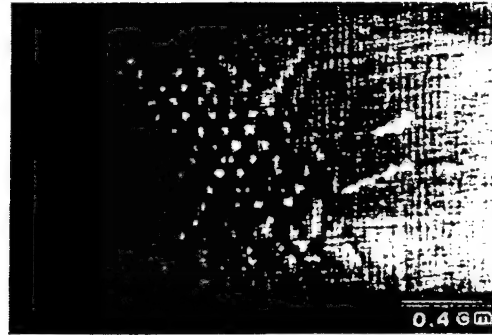


Figure 7.15: stress debonding vf 35

(a)



(b)

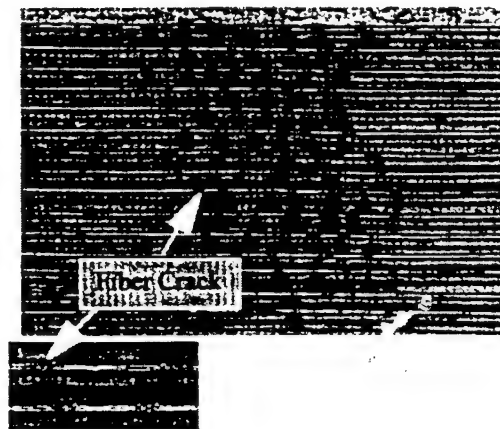


Figure 7.16: slip bands

Chapter 8

Effect of Interfacial Properties on the Fiber Fragmentation Process in Polymer Matrix Composites

8.1 Introduction

The Fiber Fragmentation Test (also called Single Fiber Composite Test, SFC) has become a commonly used method of characterizing interfaces in composites and evaluating quality of bond strength. First developed by Kelly and Tyson [1] to study copper-tungsten composites, this technique has been applied to Polymer Matrix Composites (PMC) for better understanding the mechanics and statistics of fiber fragmentation process [2, 3]. The testing procedure relies on multiple fragmentation of a single fiber embedded in a matrix under the application of an axial strain. The axial strain is progressively increased until a 'saturation' point is reached, when there are no more fiber breaks. The test yields a number of fiber fragments which is related to the fiber-matrix interfacial shear strength. Interpretation of the fragmentation data is generally based on the concept of *critical fiber length*, l_c , and a suitable load transfer model such as the *shear lag theory*. The average shear strength τ of the interface is then estimated from the equation $\tau = \frac{\sigma_s d}{2l_c}$ where σ_s is the tensile strength of the fiber at the critical length and d is the fiber diameter. l_c is derived from the mean fragment length l_m , at saturation.

A large literature base available in the application of SFC to Polymer Matrix Composites [4, 5, 6, 7, 8, 9, 10]. Though it has been accepted that SFC gives useful information about the interfacial bond quality and the fiber strength, there is no clear consensus on how to interpret the data and quantify the interfacial properties [11]. The average shear strength given by Kelly-Tyson equation based on the mean fragment length at saturation from the experiment is the most common result obtained from the test; but, this is purely a qualitative measure and does not consider the history of the fragmentation process and neglects factors such as interfacial debonding which can significantly influence the test results.

To understand the fragmentation process better, numerical modeling of the test has been adopted recently [4, 12, 7]. It has been also recognized that for better understanding of the failure process during SFC, it is necessary to obtain the test data not only at saturation, but also at various levels of applied strain [12].

Interfacial bond strength and frictional stress play a critical role in the load transfer in a single-fiber composite test; hence, understanding the effect of these parameters is crucial to predicting the test response. Thus far, there has been little effort at quantifying the effect of these parameters on the fragmentation characteristics. The influence of interfacial properties (bond strength and frictional stress) on the progression of the fragmentation process is investigated in this work using numerical simulation. A parametric study is conducted using the model to quantify the effect of interfacial bond strength and frictional sliding stress on the mean fragment length and debonding progression. Some of the numerical issues relating to the simulation of the SFC test are also addressed.

8.2 Interface Model

In this study the load transfer at the fiber-matrix interface is modeled using shear-lag theory [13]. The axial and shear stress equations from the shear-lag model are [14, 15]:

$$\sigma_f = \epsilon E_f \left(1 - \frac{\cosh(\beta(\frac{l}{2} - x))}{\cosh(\beta\frac{l}{2})} \right) \quad (8.1)$$

$$\tau = 0.5\epsilon E_f r_f \beta \frac{\sinh(\beta(\frac{l}{2} - x))}{\cosh(\beta\frac{l}{2})} \quad (8.2)$$

where:

$$\beta = \left(\frac{2.0G_M}{E_f r_f^2 \ln(\frac{R}{r_f})} \right)^{1/2} \quad (8.3)$$

and $0 \leq x \leq l$. In the above equations, σ_f is the axial stress in the fiber, ϵ is the applied strain and 'l' is the fragment length. E_f is the fiber modulus and G_m is the matrix shear modulus. r_f is the fiber radius and 'R' is the matrix width (taken about $50 r_f$). The interface is assumed to be perfectly bonded in deriving these equations. The axial and shear stress profiles at the interface are shown in Figure 8.1. It can be seen from Figure 8.1(a) that at both the ends of the fragment there is a region in which the axial stress rises exponentially reaching the far field value at the end of this region. This region where the stresses are lower

than the far field value is known as the ineffective length. The shear stresses drop to zero at the end of the ineffective length as shown in Figure 8.1(b). β in the above equation is a material constant and influences the steepness of the exponential region of the axial stress curve. As can be seen from equation 8.3, β is a function of the shear modulus of the matrix and represents the effectiveness of the load transfer between the fiber and the matrix. A higher β leads to a rapid increase in the axial stress, thereby reducing the ineffective length.

Interfacial debonding is simulated based on maximum shear strength criterion. Debonding results in drop in the stress levels increasing the ineffective length. In the debonded region axial force equilibrium arguments yield the following stress distributions. A constant frictional shear stress condition is assumed in this region.

$$\sigma_f = 2\tau_{fr}x/\tau_f \quad (8.4)$$

$$\tau = \tau_{fr} \quad (8.5)$$

where $0 \leq x \leq l_d$. $l_d = ml/2$ is the debonded length where 'm' is the debonding ratio. The length of debonding is determined based on the axial force equilibrium and by imposing the continuity of the axial stresses at the end of the debonded zone. In the bonded region shear lag equations are applicable and are modified to account for the debonded length [15]:

$$\sigma_f = \epsilon E_f - [\epsilon E_f - 2\tau_{fr}sm] \frac{\cosh(\beta(\frac{l}{2} - x))}{\cosh(\beta r_f s(1 - m))} \quad (8.6)$$

and,

$$\tau = 0.5\beta r_f [\epsilon E_f - 2\tau_{fr}sm] \frac{\sinh(\beta(\frac{l}{2} - x))}{\cosh(\beta r_f s(1 - m))} \quad (8.7)$$

where $s = \frac{l}{d}$ is the aspect ratio (where d is the diameter of the fiber). The debond ratio 'm' is determined by iteratively solving the following equation [15]:

$$m = \frac{\epsilon E_f - 2\frac{\tau_{deb}}{\beta r_f} \coth(\beta r_f s(1 - m))}{2.0\tau_{fr}s} \quad (8.8)$$

The axial stress and shear stress profiles in the presence of debonding are shown in Figure 8.2. As can be seen from equation 8.8 the debonding ratio 'm' is a function of the bond strength τ_{deb} and the frictional stress τ_{fr} . The significance of these two important interfacial parameters will be discussed in detail in section 8.5. The frictional stress $\tau_{fr} = \mu p$ where μ is the coefficient of friction and 'p' is the radial stress. The radial stress gets the contribution from three possible sources: thermal residual stress, differential Poisson effect and the fiber surface asperities.

8.3 Statistical Model for Fiber Strength Distribution

The two-parameter Weibull probability theory is used to extrapolate the fiber strength from the test gage length to the desired unit length used in the simulation. According to this theory the probability that a fiber of length 'L' breaks at a stress lower than σ is given by:

$$P(\sigma) = 1 - \exp\left(-\frac{L}{L_o} \left[\frac{\sigma}{\sigma_o}\right]^q\right) \quad (8.9)$$

where 'q' is the Weibull modulus (shape factor), L_o is a reference length which can be arbitrarily chosen, and σ_o is the scale parameter for unit length ratio ($\frac{L}{L_o} = 1$).

The variation of fiber strength along the length of the fiber due to the distribution of flaws is taken into account by introducing the Weibull Model in the frame work of Monte Carlo simulation. The intial length of the fiber is divided in to a number of small links. Random values of link strengths are derived by inverting equation 8.9. L_o is taken as unity. Thus

$$\sigma(i) = \sigma_o L^{-1/q} \left[\ln\left(\frac{1}{1 - R(i)}\right) \right]^{1/q} \quad (8.10)$$

where $R(i)$ is a random number between zero and unity which represents the probability of failure of i th link and 'i' is the number of the fiber link.

8.4 Implementation of the model

The numerical procedure is outlined in the flow-chart in Figure 8.6. The fiber is divided into a number of small links (2500 links for all the cases run here and was found to be adequate). The average strength of one link is evaluated by extrapolating from the value at the test gage length using equation ???. The statistical distribution of strength values along the length of the fiber is given by equation 8.10. The geometric, material and statistical parameters of the fiber and matrix are input into the program. These include the Young's moduli, Weibull scale parameter and Weibull modulus (shape factor), Poisson ratio and radii of the fiber and matrix; and the initial length of the fiber.

A strain is initially applied to the un-broken fiber and the resulting stress in each link is compared with its respective strength. If the stress induced exceeds the link strength, a break occurs in this link, resulting in the formation of two fragments. At this point, a check is made to see if any debonding takes place in the entire fiber. If there is any debonding, the debond length is calculated through the iterative solution of equation 8.8. Then, the axial stresses are calculated for the bonded and debonded regions of the fragment. The strain is now incremented and the procedure is repeated. This iterative procedure is repeated until no further breaks occur with increase in strain. A state of 'saturation' is reached at this strain level.

8.5 Results and Discussion

The numerical simulation of the fiber fragmentation test is conducted for a carbon-epoxy system. The material properties of the fiber and matrix and the Weibull parameters of the fiber [14] are given in Table 1. A specimen of gage length 10 mm is used in all the cases. To study the effect of interfacial conditions on the fragmentation test results, two extreme conditions are considered: a perfectly bonded interface ($\tau_{deb} = \infty$) and a weak interface with a low τ_{deb} and τ_{fr} . Perfect bonding though a hypothetical situation, is considered here mainly to bring out the effect of debonding on fragmentation process by comparing the two cases.

8.5.1 Stress Distributions

Figure 8.6 shows the axial stress profile in the fiber as a function of increasing applied strain for the case of strongly bonded interface. It can be seen that the number of breaks continue to increase with increase in applied strain till the fragment lengths are smaller than the load transfer length required for the axial strain (or stress) to reach the far field value (Figure 8.6 b); further breaks are then considerably reduced. When the bonding at the interface is not perfect, debonding occurs in the regions of maximum shear stress which are at the end of the fragments. A bond strength of 60 MPa is used. The debonded length is calculated using the equations in section 8.2. Figure 8.6 shows the axial stress profiles from the simulation for the weakly bonded case. Debonding reduces the effective length available for load transfer, leading to a drop in the fiber stresses. Debonding progresses with increasing applied strain; this reduces the probability of further breaks resulting in saturation at a lower applied strain when compared with the perfectly bonded case. It can be seen from Figure 8.6(b) that a significant portion of the specimen length has debonded at this stage.

8.5.2 Mean Fragment Length and Saturation

Numerical simulation shows that the variation of cumulative number of breaks (or fiber fragments) with increasing applied strain is significantly different for weak and strong interfaces. For the case of perfect bonding, the rate of increase of fiber breaks with increasing applied strain is almost uniform as can be seen from Figure 8.6. It can also be seen that saturation of breaks is not seen even at 10% strain. Figure 8.6 shows the value of mean fragment length l_m ($=$ total length/ cum. number of breaks) as a function of applied strain for both strong and weak interfaces. In the absence of debonding, the l_m value decreases with increasing strain (Figure 8.6(a)) due to continuing process of fragmentation. For the sake of clarity the variation only after 4.5% strain is shown in the Figure; more than 25 breaks have occurred at this stage as can be seen from Figure 8.6, causing a drop in l_m from 10,000 μm to 400 μm . The slope of the curve in Figure 8.6(a) is very steep in the initial regions where the applied strain is less than 10%. The slope of the curve drops after this point as the fragment

lengths become smaller than the load transfer length. Saturation is not reached at even 40 %. (Strains above 5% are unrealistic from an experimental point of view, but the plot was taken up to 50% to show the trend in the curve). By contrast, saturation is seen at only 4% when τ_{deb} was taken at 60 MPa (Figure 8.6(b) and 8.6). As can be seen from Figures 8.6 and 8.6 the number of fiber breaks at any strain is much lower for the weakly bonded case. This is due to the extensive debonding which limits the number of breaks and also results in much lower strain for saturation.

The evolution total debonding of the fiber as a function of applied strain is shown in Figure 8.6. A comparison of saturation strain in Figure 8.6 with the corresponding % debonded length in Figure 8.6 indicates that more than 80% of the fiber length has debonded at saturation. Also, comparing the debonding with the fiber breaks (Figure 8.6), it is seen that the debonding occurs most when breaks are occurring, and reduces once the breaks stop. This is because the frictional forces in the debonded region will become significant after extensive debonding and resist further debonding in the broken fragments. Any new break will have minimum resistance from friction and hence can debond more than an already debonded fragment; but, as noted earlier, debonding considerably reduces the probability of further breaks in the broken fragments.

8.5.3 Effect of variation in interfacial properties

Bond Strength

A parametric study is conducted to examine the effect of bond strength on the mean fragment length at saturation. Figure 8.6 shows the variation of l_m with bond strength. It can be seen that higher bond strengths lead to a drop in the mean fragment length (increase in the number of breaks) for a given applied strain, as the initiation of debonding is postponed. This is also evident from the increase in the peak value in the histogram showing the number of breaks versus fragment size (Figure 8.6). It can be seen that with increase in bond strength the spread in the distribution of fragment size significantly decreases with the peak value moving to the left (smaller fragment size). The histogram is plotted from simulations performed with more than 40 different seeds to generate a reasonable volume of sampling data. It was found that the effect of sampling size is much more significant on the fragment length distribution than on the mean fragment length.

Frictional Stress

Increased frictional forces cause a reduction in the debonded length. This results in an increase in the number of breaks which is clear from the reduction in l_m in Figure 8.6. A comparison of the slopes in Figures 8.6 and 8.6 reveals that the sensitivity of l_m to change in the frictional properties is much higher when compared to a corresponding drop in the bond strength, especially at lower values of τ_{fr} ; but as the value of τ_{fr} approaches τ_{deb} , further

decrease in l_m is negligible.

8.5.4 Comparison with Experimental Data

Lacroix et al. [12] performed single fiber fragmentation tests on carbon-epoxy composites and measured the number of breaks as a function of applied strain. Carbon fibers with different surface treatments were used in the study. They found that fiber surface treatments modify the interfacial conditions and affect the experimental results. Figure 8.6 shows a comparison of the results of fiber fragmentation simulation with experimental data. Comparisons are made for a fiber treatment of 10% standard surface treatment (SST). The figure shows the scatter in the experimental data for five tests. The numerical simulation in Figure 8.6 is the average of a number of runs with different seeds for random number generation. The material constants used in the simulation are shown in Table 2. A good correlation between the simulation and experiment is obtained for the mean fragment length values with $\tau_{deb} = 170.0 MPa$ and $\tau_{fr} = 50.0 MPa$. It can be seen that in the experiment fiber breaks occur at a lower value of applied strain compared to the simulation (curve A). Fiber statistics dominate the occurrence of the first few breaks and hence a difference in the Weibull parameters possibly due to the deterioration of the fiber strength in the composite may be the cause of this shift. To confirm this the simulation is repeated after modifying the Weibull scale parameter (curve B). As expected, a lower value of the scale parameter (7300 instead of 8110) shifted the curve to the left, closer to the experimental results.

8.6 Summary and Conclusions

A numerical simulation of the single fiber fragmentation test is performed, taking into account, the random variation of the flaw strength of the fiber. The effect of debonding and frictional stress on the mean fragment length l_m at saturation is studied. Numerical simulation shows that the variation of cumulative number of breaks and debond progression with increasing applied strain is significantly affected by the interfacial properties. It is found that in the case of weak interfaces saturation of fiber fragments occurs at much lower applied strain values and is usually associated with extensive debonding (more than 80% of the specimen length in some cases). It is seen that an increase in either τ_{deb} and τ_{fr} decreased the l_m value. The results from the numerical simulation are correlated with the experiments on carbon-epoxy composite systems and a reasonably good match is observed.

Bibliography

- [1] Kelly A. and Tyson W.R. Tensile properties of fiber-reinforced metals: Copper/tungsten copper/molybdenum. *Journal of Mechanics and Physics of Solids*, 13:329–350, 1965.
- [2] Curtin W. A. Exact theory of fibre fragmentation in a single-filament composite. *Journal of Materials Science*, 26(6):5239–5253, 1991.
- [3] Curtin W. A. Determining Fiber Strength vs. Gage Length. *Polymer Composites*, 15(6):474–478, 1994.
- [4] Favre J.F. and Jacques D. Stress Transfer by shear in carbon fibre model composites: Part 1: Results of single-fibre fragmentation tests with thermosetting resins . *Journal of Materials Science*, 25:1373–11380, 1990.
- [5] Piggot M.R. Failure processes in the fibre-polymer interphase . *Composites Science and Technology*, 42:57–76, 1991.
- [6] Ho A., Netravali A.N., and Phoenix S.L. Interfacial shear strength studies of Nicalon fibers in epoxy matrix using single fiber composite test. *Polymer Composites*, 16(6):542–548, 1995.
- [7] Zhou L. M., Kim J. K., Baillie C., and Mai Y.W. Fracture Mechanics analysis of the fibre fragmentation test. *Journal of Composite Materials*, 29:881–902, 1995.
- [8] Baxevanakis C., Jeulin D., and Valentin D. Fracture statistics of single fiber composite specimens. *Composites Science and Technology*, 48:47–56, 1993.
- [9] Ling S. and Wagner H.D. Relationship between fiber flaw spectra and the fragmentation process: A computer simulation investigation. *Journal of Materials Science*, 28:6233–6245, 1993.
- [10] Shioya M. and Takaku A. Estimation of fibre and interfacial shear strength using a single fibre compsite . *Composites Science and Technology*, 55:33–39, 1995.
- [11] Feillard P., Desarmot G., and Favre J.F. Theoretical aspects of the fragmentation test . *Composites Science and Technology*, 50:265–279, 1994.
- [12] LaCroix T., Keunnings R., Desager M., and Verpoest I. A new data reduction scheme for the fragmentation testing of polymer composites. *Composites Science and Technology*, 43:379–387, 1992.

- [13] Cox H.L. The elasticity and strength of paper and other fibrous materials. *British Journal of Applied Physics*, 3:72-79, 1952.
- [14] Favre J.F., Sigety P., and Jacques D. Stress Transfer by shear in carbon fibre model composites:Part 2: Computer Simulation of the fragmentation test . *Journal of Materials Science*, 26:189-195, 1991.
- [15] LaCroix T., Tilmans B., Keanings R., Desager M., and Verpoest I. Modelling of critical fibre length and interfacial debonding in the fragmentation testing of polymer composites. *Composites Science and Technology*, 43:379-387, 1992.

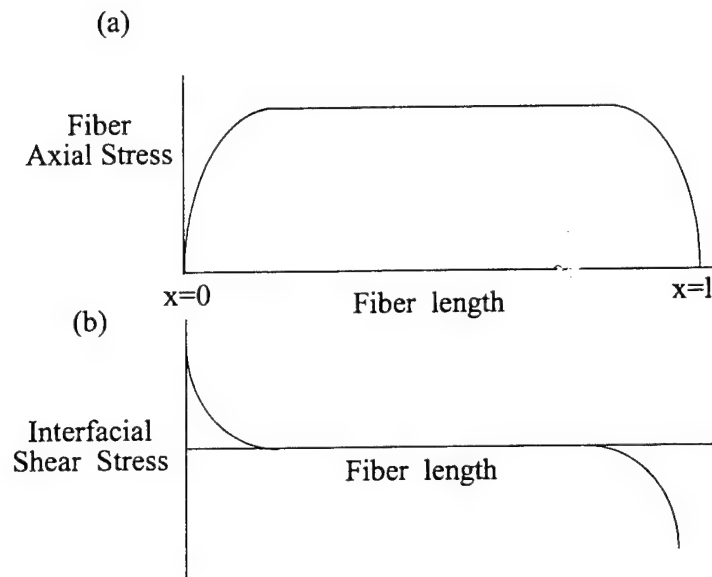


Figure 8.1: Stress distribution with no debonding. (a) axial stress in the fiber; (b) interfacial shear stress

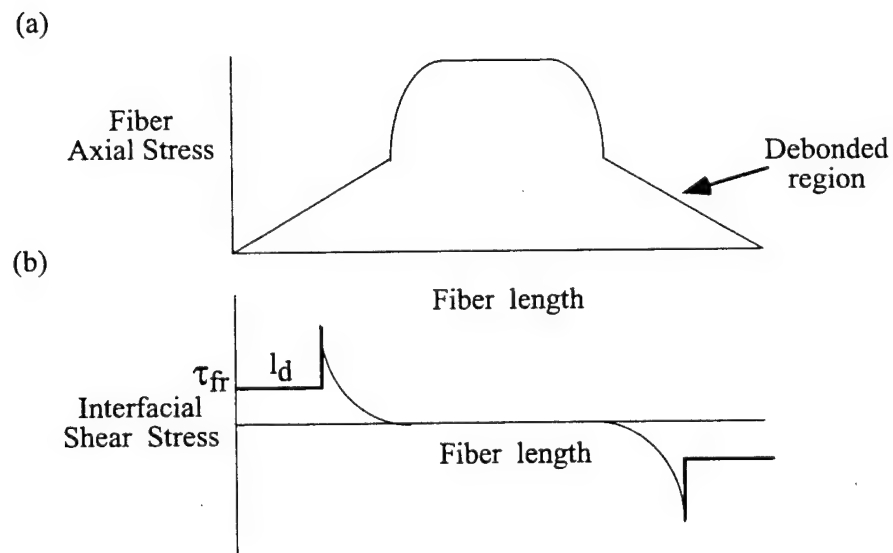


Figure 8.2: Stress distribution with partial debonding. (a) axial stress in the fiber; (b) interfacial shear stress

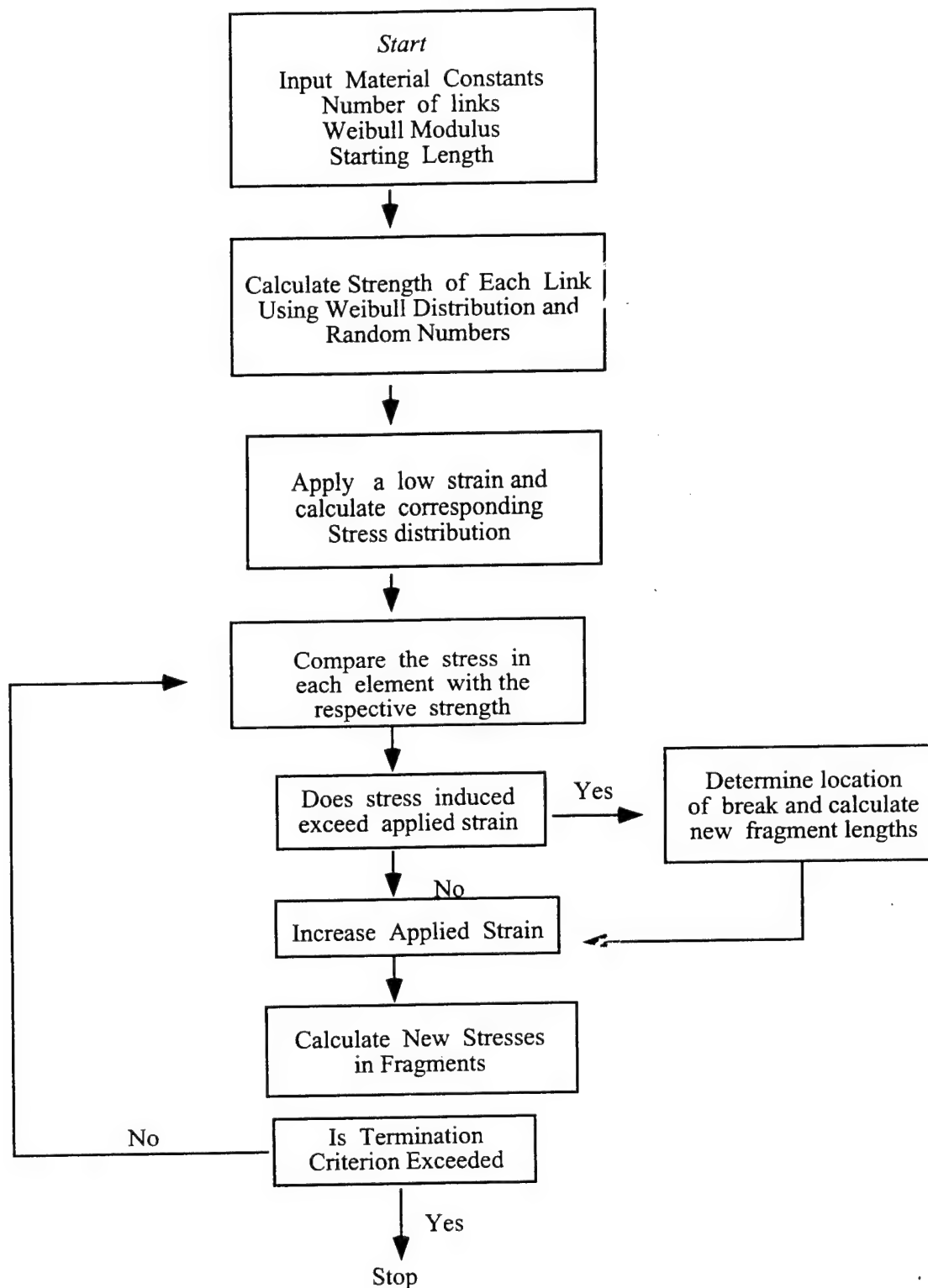


Figure 8.3: Flow chart for the simulation of the fiber fragmentation test

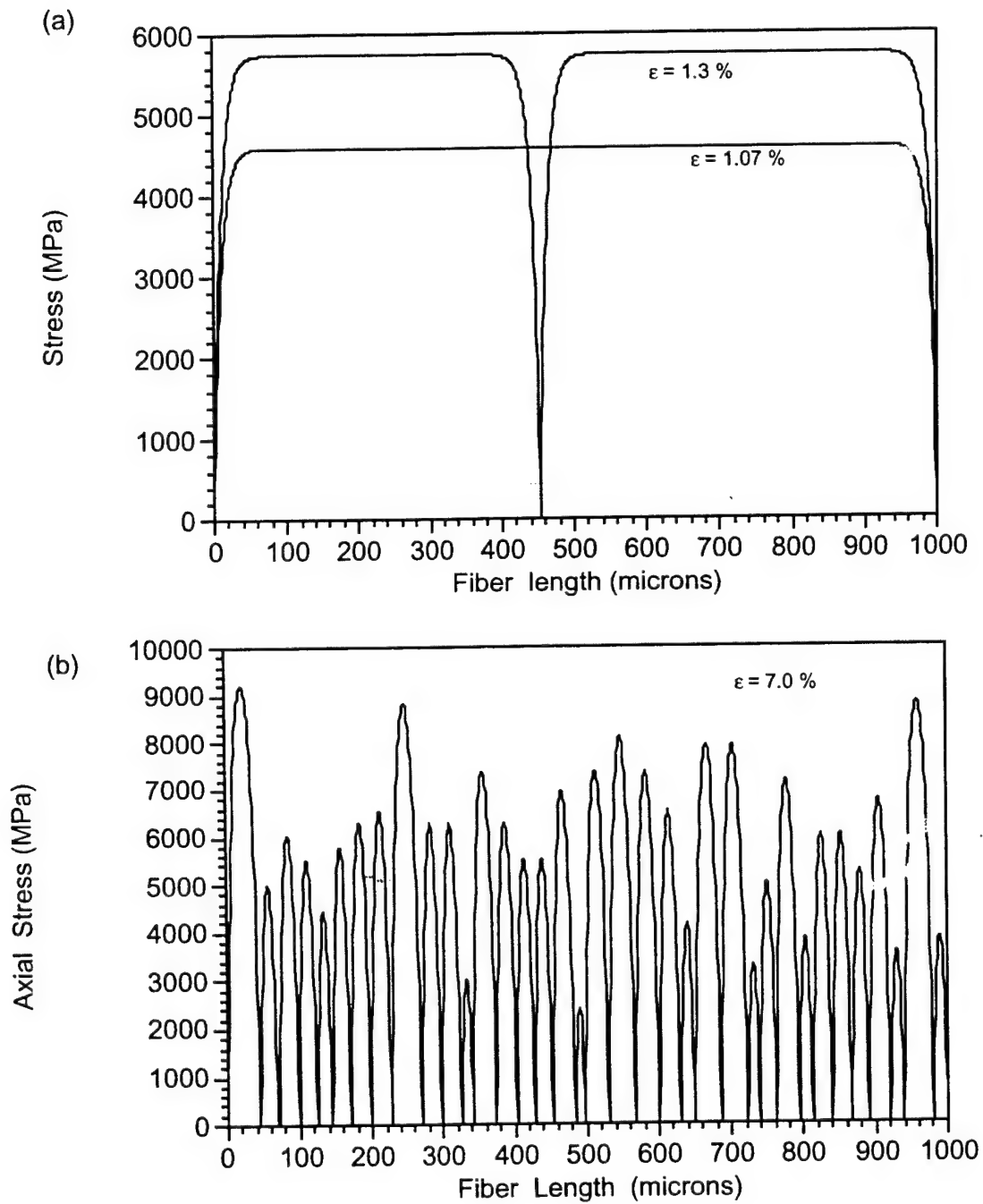


Figure 8.4: Axial stress in fiber with strong bond (a) at intermediate applied strain, (b) high strain

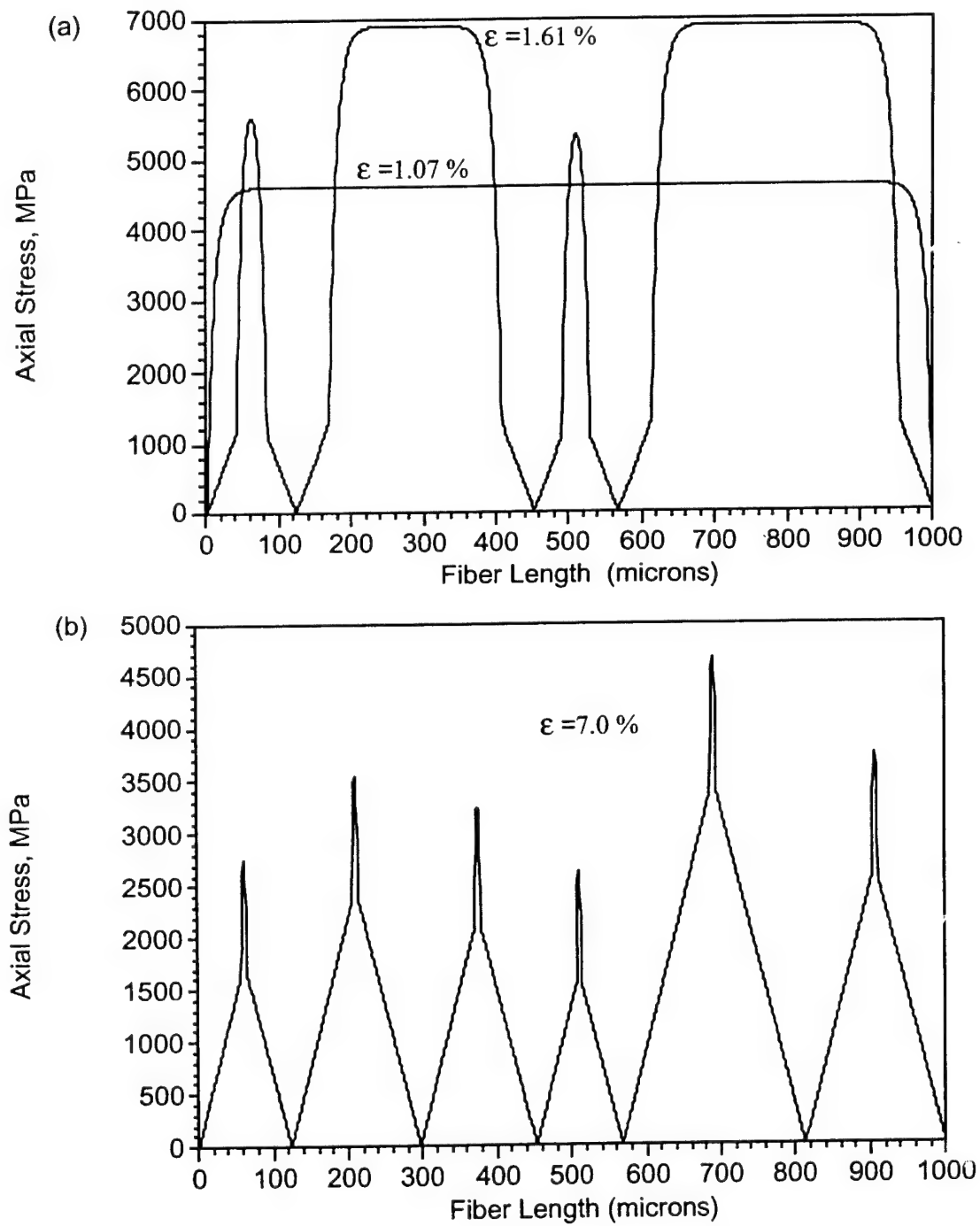


Figure 8.5: Axial stress profile with debonding (a) at initial loading and intermediate stages, (b) at saturation

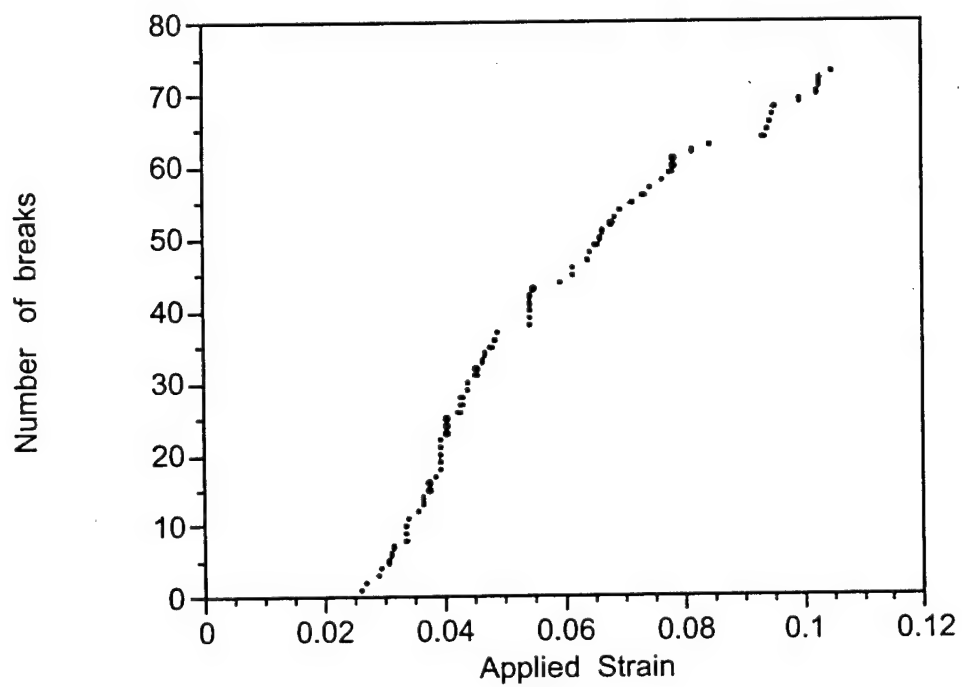


Figure 8.6: Number of breaks vs. applied strain (perfect bonding)

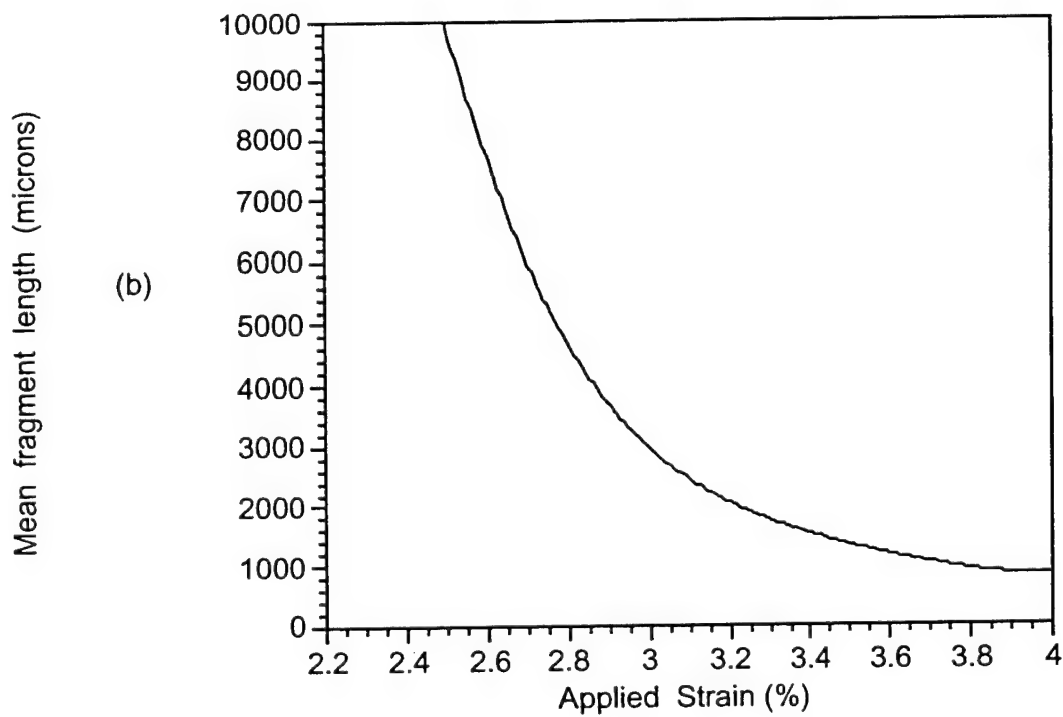
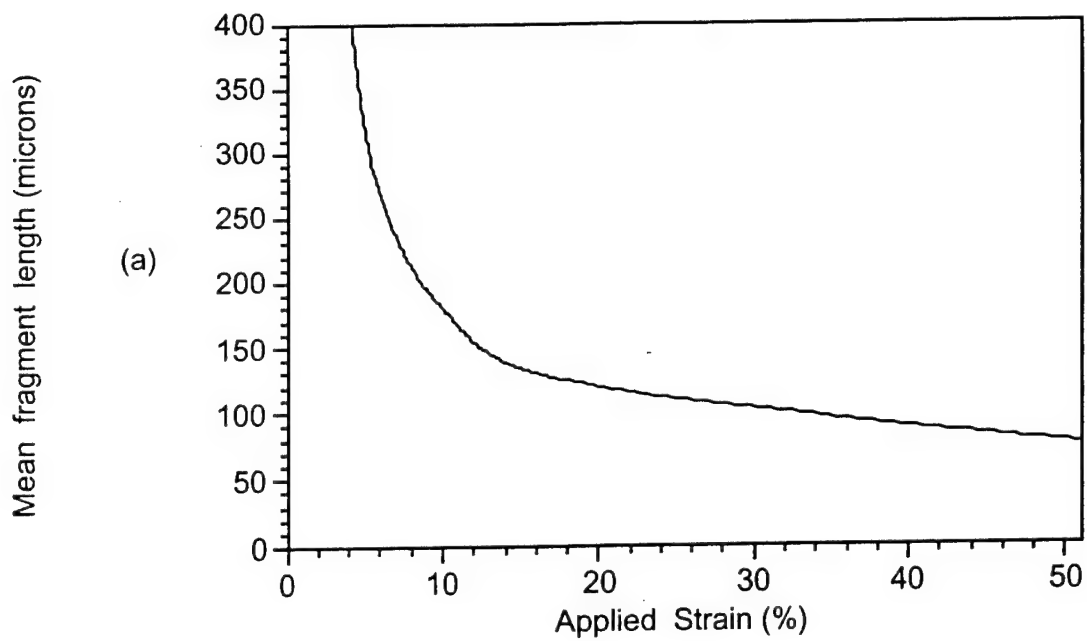


Figure 8.7: (a):Variation of average fragment length with applied strain for a strong bond.
(b):Variation of average fragment length with applied strain for a weak bond.

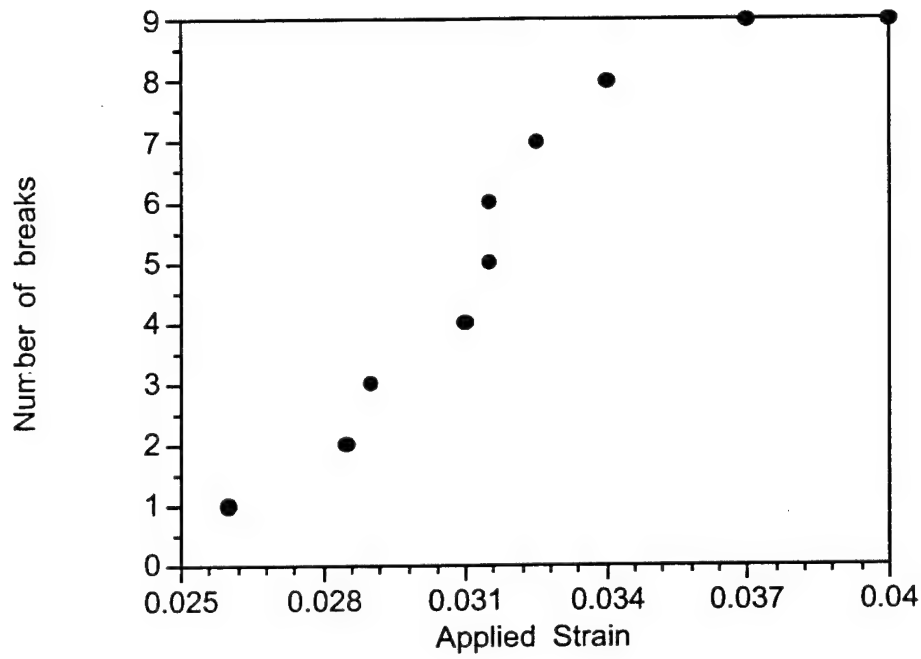


Figure 8.8: Number of breaks vs. applied strain (bond strength = 60 MPa, frictional stress = 20 MPa).

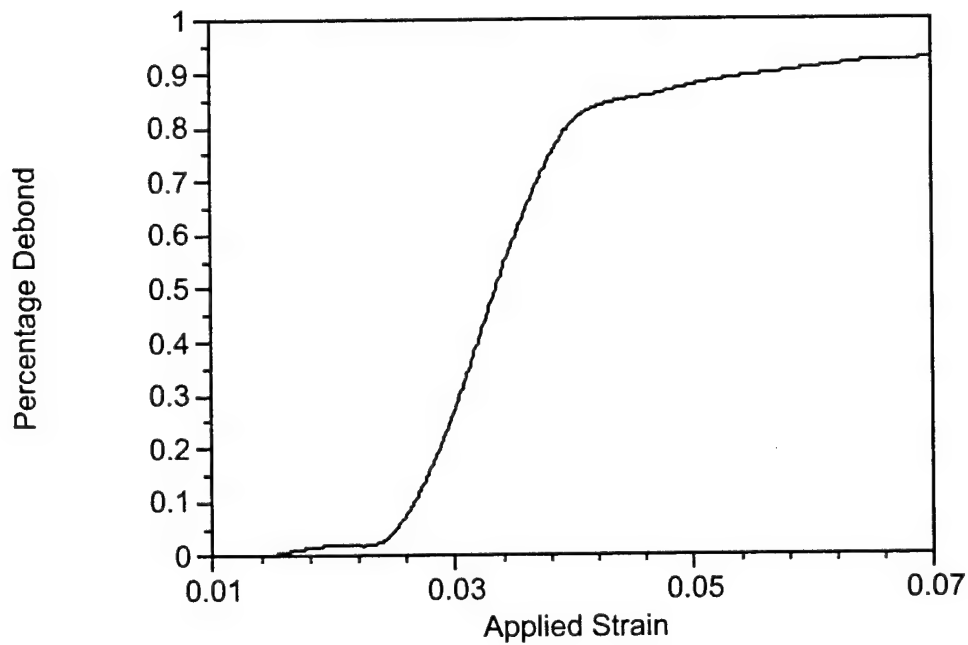


Figure 8.9: Variation of debonding with applied strain

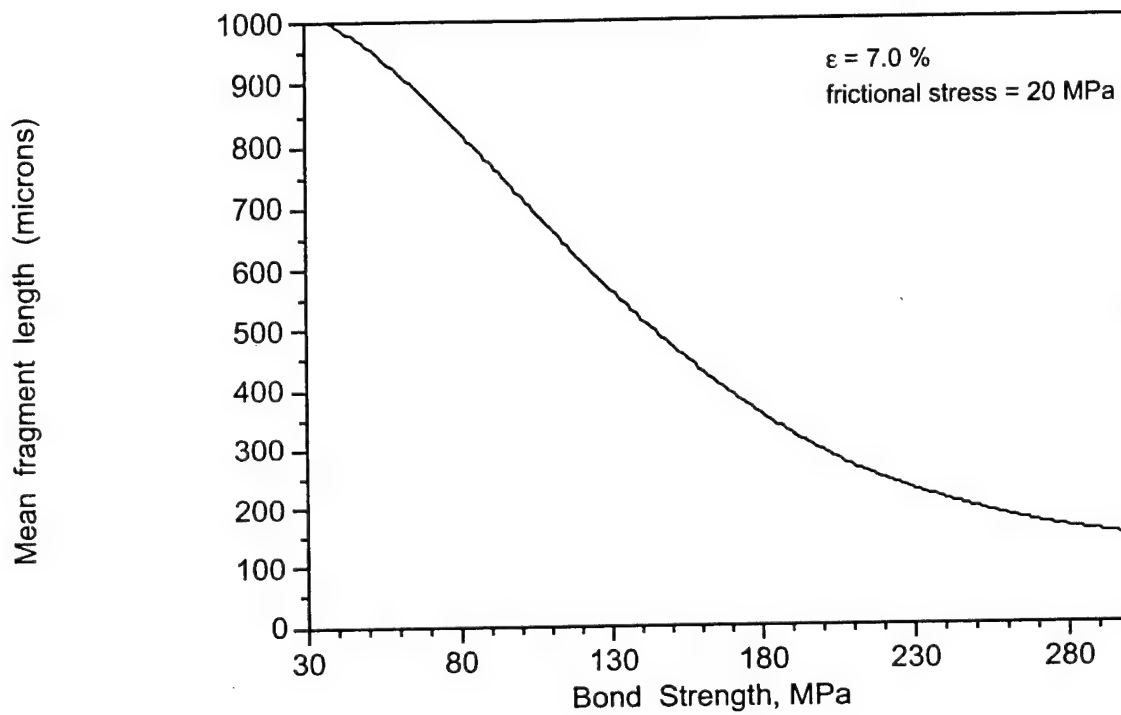


Figure 8.10: Variation of mean fragment length with bond strength.

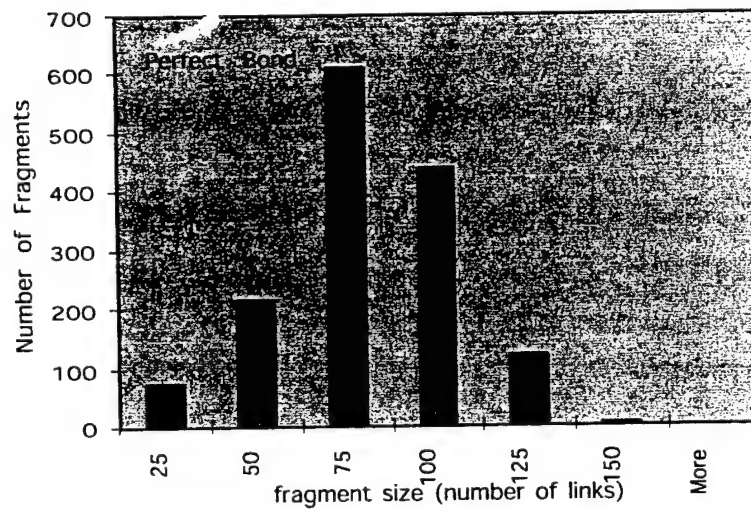
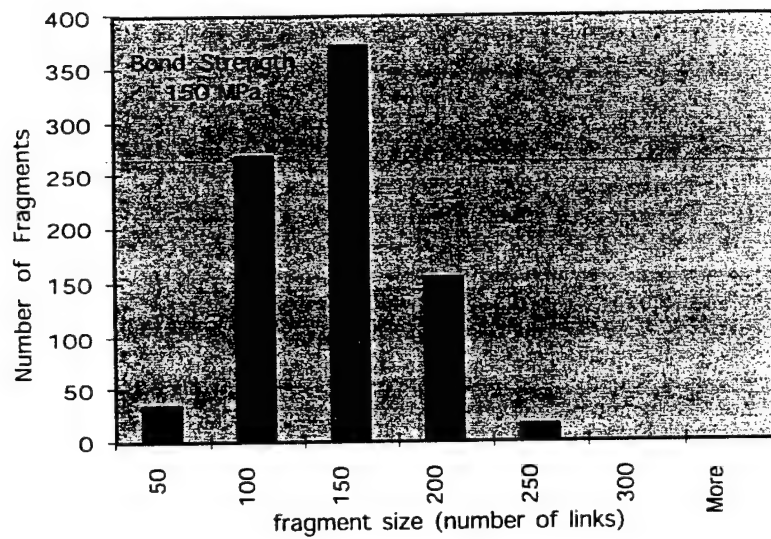
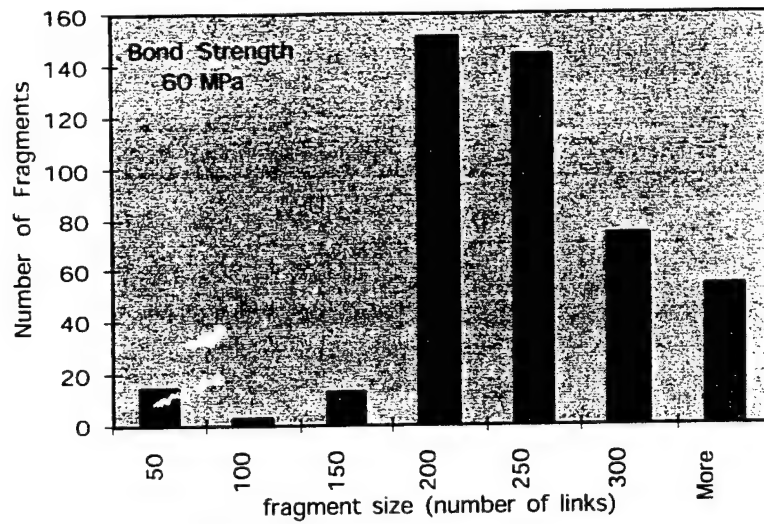


Figure 8.11: Fragment length distribution with increasing bond strength (1 link = 4 microns)

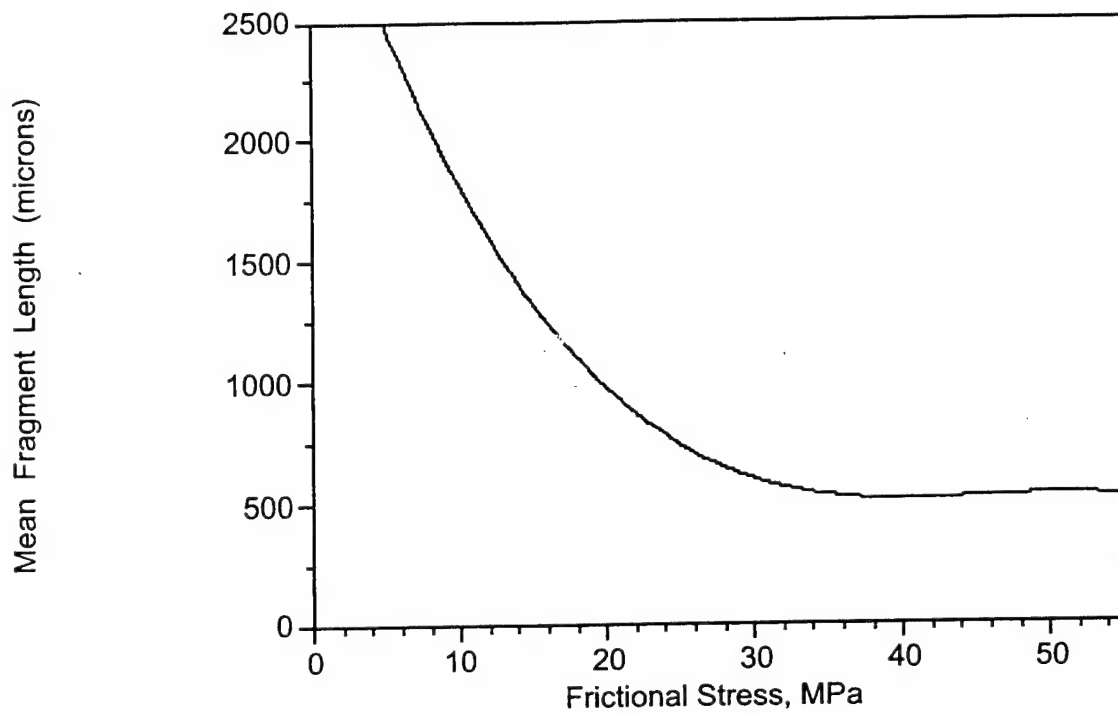


Figure 8.12: Variation of mean fragment length with frictional stress

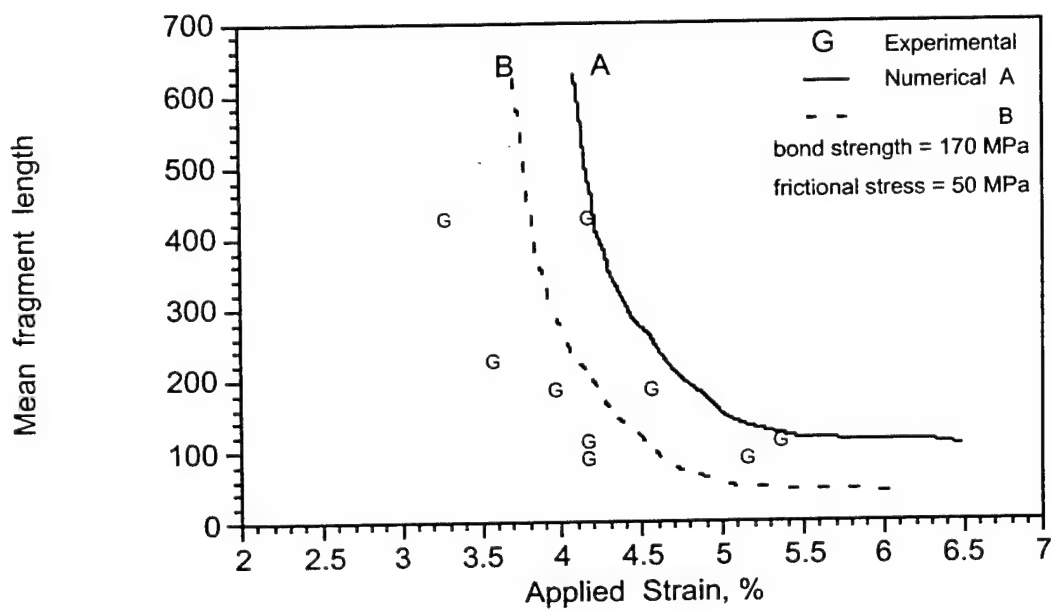


Figure 8.13: Comparison of the numerical values with experimental results

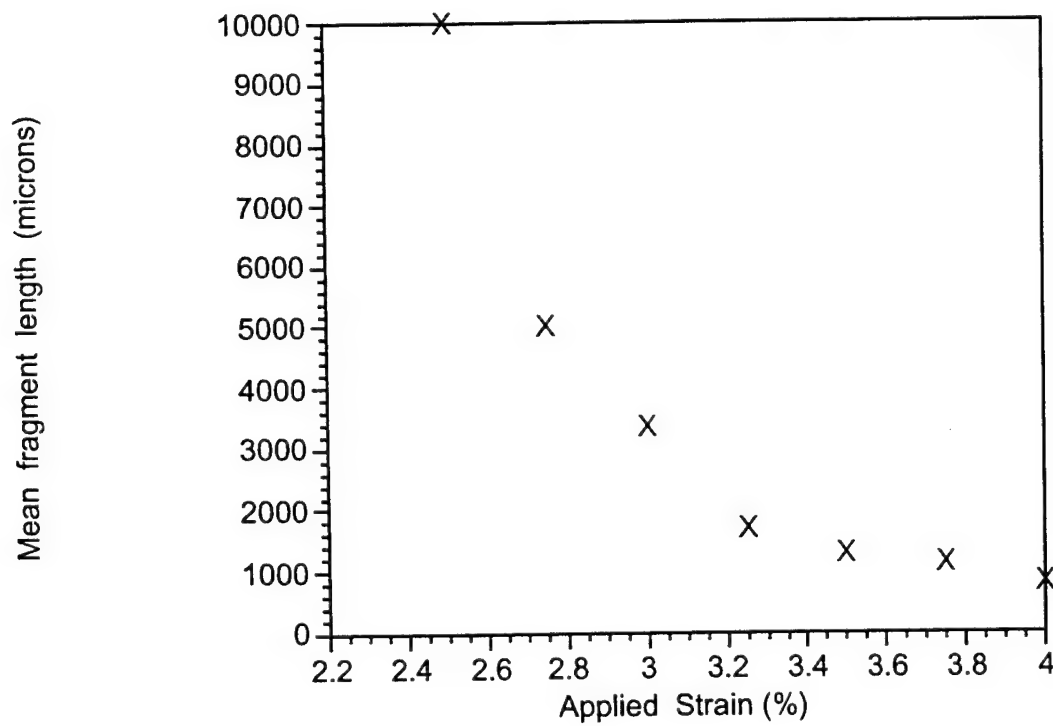
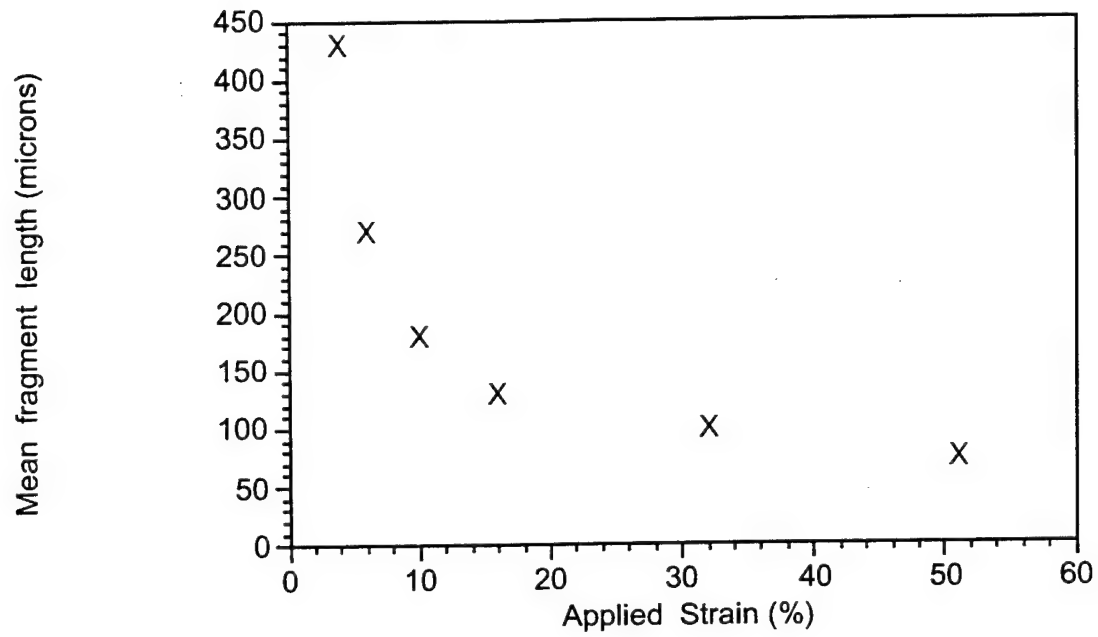


Figure 8.14: debond-length friction

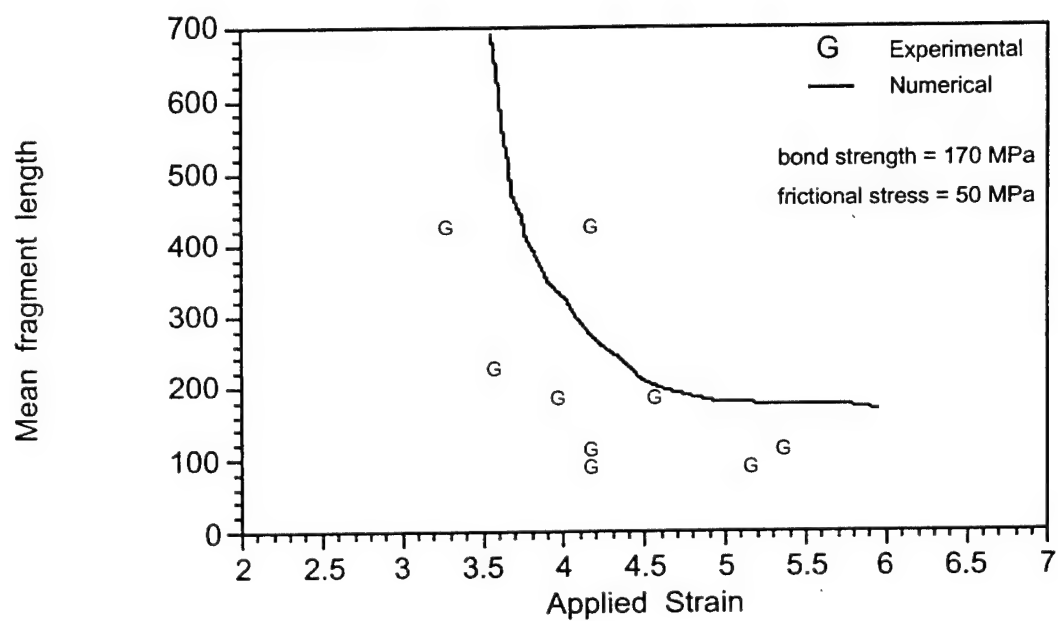


Figure 8.15: exp comp lm

Chapter 9

Summary and Conclusion

9.1 Introduction

The elevated temperature specific stiffness and strength properties of Metal Matrix Composites (MMCs) have made them candidate materials to meet the stringent requirements of the future U.S. Air Force aircrafts. The successful application of such composites not only relies on the use of right fiber and matrix materials, but strongly depends on the interface between the fiber and matrix. The processing conditions prevailing during the consolidation of these composites play a critical role in the evolution of the fiber-matrix interface.

A fundamental understanding of the relationship between the processing conditions, chemistry of the reaction zone at the interface, and the mechanical properties of the interface is important to the successful use of MMCs.

9.2 Overall goal of the research work

The primary objectives of the research work are

- To establish a link between the interface chemistry and its mechanical properties of Titanium Matrix Composites.
- To study the effect of interfacial properties and inelastic behavior of the matrix on the evolution of damage in Metal Matrix Composites.

The research effort involves composite consolidation, controlled exposure studies, chemical, metallurgical and mechanical characterization and numerical modeling of selected Titanium Metal Matrix Composites.

9.3 Basic Research Issues

The role of fiber-matrix interface is crucial to the performance of the composites. Interfacial debonding is one of the common damage mechanism in most fiber-reinforced MMCs. The fatigue, fracture, transverse (90° to the fiber direction) stress-strain behavior, are found to be strongly influenced by the interfacial bonding conditions [1]. The bond strength of an interface is the net effect of the contributions from chemical and mechanical components [2]. The former is due to the reaction at the interface during the composite processing and depends on the fiber and matrix materials and the processing conditions. The mechanical component is due to the sliding resistance at the interface and depends on the presence of residual stresses and interfacial surface irregularities. It is necessary to understand the role of this mechanical component while characterizing the interfacial strength and toughness.

The interfacial chemistry evolves with time exposure to elevated temperature and/or environment, and influences both the size and phases within the reaction zone of the interface. Titanium alloys and intermetallics which are the matrix materials in this work are very highly reactive at elevated temperatures and produce nonstoichiometric carbides and silicides within the interphases. Chemical compositional and phase evolution through an understanding of the diffusional process or otherwise is necessary.

Residual stresses develop when the MMCs and IMCs are cooled after processing from a reference temperature at which they are stress free, to room temperature. This is due mainly to the difference in the coefficients of thermal expansion (CTE) of fiber and matrix material. These stresses reach considerable levels because, in typical MMCs and IMCs considered in this study, the mismatch in the CTE is quite significant ($\alpha_{matrix} \geq 2\alpha_{fiber}$) and the temperature differential involved in the cooling process is high (about 800°C to 900°C). Residual stresses are affected by the evolution of interfacial chemistry, and by the inelastic response of matrix material.

The mechanical response of the interfaces is usually measured using a thin slice push out test, and transverse tensile testing. However, extracting quantitative interfacial properties from the push-out test is not trivial. A comprehensive process model (including composite consolidation and specimen preparation) to understand the interfacial failure process during push-out tests is needed for better interpretation of the test results. In the numerical simulation, either a stress based failure criterion or an energy based criterion can be used to model the failure process.

In summary, basic research issues in this effort focus on the *understanding the chemical evolution (diffusional) process at the interface, accurately computing the residual stresses in the interface zone (accounting for matrix inelasticity, and load shedding during crack propagation), developing a mechanistic model of an interface based on stress or energy failure criterion, and studying the effect of interface properties on the performance of the composites.*

9.4 Technical Approach

The technical approach involves both experimental and computational components. For our purpose, two model composite systems were selected, Ti-6Al-4V/SSC-6 and Timetal 21S/SCS-6. While the former was consolidated within our laboratory, the latter was obtained from other sources. The effect of elevated temperature was studied by heat treating specimens at selected temperatures (450° C, 700° C and 927° C) in vacuum for varying periods of time. The time periods used are 25, 70 and 120 hours. Scanning Electron Microscope (SEM) is used to measure the thickness of the interface. Interfacial chemistry and elemental composition are monitored using Energy Dispersive X-ray Spectroscopy (EDX).

Push-out tests to measure interfacial mechanical properties are conducted at NASA Lewis Research Center (thanks to Dr. J. Eldridge), on the heat treated specimens and the results are compared with those of as-processed ones. Modeling push-out test involves three major stages. Step 1 involves modeling the composite consolidation at high temperatures and then cooling down to room temperature which induces residual stresses in the composite. Step 2 is the specimen preparation stage consisting of slicing a thin push-out specimen from the bulk composite which results in stress redistribution at the two ends of a fiber. Step 3 is modeling the loading stage where compressive load is applied to the fiber until it is pushed out of the specimen. A detailed description of the above sequence of steps is provided elsewhere [3]. The interface is modeled as a contact surface and the bonding at the interface is simulated using high stiffness springs. The interface failure process is modeled using a strain energy based failure criteria given by:

$$G_i \geq G_{ic}$$

where G_i is the strain energy release rate for the interface crack and G_{ic} is the critical value of the strain energy release rate. The interface crack propagates further when its strain energy release rate exceeds the critical value. A numerical method based on the equivalent domain integral technique (EDI) [8, 9, 4] has been developed by the authors [5, 7] to evaluate the strain energy release rate of propagating interface cracks. The EDI method was implemented in the commercial finite element analysis software MARC [6] through user subroutines. It is then used in the modeling of interface failure during thin-slice fiber push-out test. Figure 2 shows the application of numerical simulation to evaluate fracture toughness from the experimental data.

9.5 Significant Results

The evolution of interface in Titanium Matrix Composites (e.g. SCS-6/Timetal 21s) composite system is studied by means of heat treatment experiments, with the objective of establishing a link between the evolution of chemistry and geometry of the reaction zone and the interfacial properties.

- Microstructural studies reveal that reaction growth is due to transformation of both coating and the matrix. The growth of the reaction zone into the matrix is much more than the growth towards the fiber, as carbon is able to diffuse much farther into the matrix than the diffusion of Titanium into the fiber.
- Reaction zone sizes increase rapidly with time at 927° C. At lower temperatures such as 700° C and 450° C no significant increase in reaction zone size is observed for this system.
- Push-out tests conducted on heat treated specimens reveal that the effect of thermal exposure on interfacial properties is predominantly due to exposure temperature. Time of exposure is found to have only a secondary effect.
- Load displacement curves for as-processed SCS-6/Timetal 21s specimens and specimens heat treated at 700° C and 450° C have sharp load drops at the point of complete debonding marked by distinct acoustic emission signals. The results for specimens heat treated at 927° C show that debonding occurs as a slow process with no observable sharp load drops and acoustic emission signals.
- Fracture toughness values remain more or less constant for normal use temperatures in the range of 450° to 700° C. The values however, increase when the exposure temperature is raised to 927° C.
- Fracture surfaces of the specimens exposed at 927° C show that debonding took place in the reaction zone whereas in as-processed specimens and those heat treated at the lower temperature ranges debonding initiated in the coating. This is because the weak region in the coating is replaced by the stronger interfacial region.

9.6 Relevance to Air Force and Future Direction

From the above study, it is clear that interfaces play a crucial role not only in MMCs but in high temperature heterogeneous systems, e.g., thermal barrier coatings. Clearly a deeper understanding of the interfacial fracture processes is needed using an innovative experimental measurements and advanced computational schemes at micron levels.

Bibliography

- [1] B. S. Majumdar and G. M. Newaz. Inelastic Deformation of Metal Matrix Composites: Plasticity and Damage Mechanisms. *Philosophical Magazine A*, 66(2):187–212, 1992.
- [2] A. G. Evans, M. Ruhle, B. J. Dalgleish, and P. G. Charalambides. The Fracture Energy of Bimaterial Interfaces. *Materials Science and Engineering*, A126:53–64, 1990.
- [3] C. R. Ananth and N. Chandra. Numerical Modeling of Fiber Push-out Test in Metallic and Intermetallic Matrix Composites - Mechanics of the Failure Process. *Journal of Composite Materials*, 29(11):1488–1514, 1995.
- [4] I. S. Raju and K. N. Shivakumar. An Equivalent Domain Integral Method in the Two-Dimensional Analysis of Mixed Mode Crack Problems. *Engineering Fracture Mechanics*, 37(4):707–725, 1990.
- [5] S. Mukherjee, C. R. Ananth, and N. Chandra. Computational Analysis of Interfacial Fracture Process in Fiber Push-out Tests. *Composites Science and Technology*, (submitted) March 1996.
- [6] MARC Analysis Corporation. *MARC Version: K5, User Manuals*, 1992.
- [7] S. Mukherjee, C. R. Ananth, and N. Chandra. Evaluation of Fracture Toughness of MMC Interfaces Using Thin-slice Push-out Tests. *Scripta Materialia*, 36(11), 1997.
- [8] G. P. Nikishkov and S. N. Atluri. An Equivalent Domain Integral Method for Computing Crack Tip Integral Parameters in Non-Elastic, Thermomechanical Fracture. *Engineering Fracture Mechanics*, 26:851–867, 1987.
- [9] G. P. Nikishkov and S. N. Atluri. Calculation of Fracture Mechanics Parameters for an Arbitrary Three-Dimensional Crack, by the Equivalent Domain Integral Method. *International Journal for Numerical Methods in Engineering*, 24:1801–1821, 1987.